Inelastic Losses in X-ray Absorption Theory

Luke Campbell

A dissertation submitted in partial fulfillment
of the requirements for the degree of

Doctor of Philosophy

University of Washington

2002

Program Authorized to Offer Degree: Physics

University of Washington

Graduate School

This is to certify that I have examined this copy of a doctoral dissertation by

Luke Campbell

and have found that it is complete and satisfactory in all respects,
and that any and all revisions required by the final
examining committee have been made.

Chair of Supervisory Committee:

_____

John J. Rehr

Reading Committee:

_____

John J. Rehr

_____

Larry Sorensen

_____

Stephen R. Sharpe

Date: _____

In presenting this dissertation in partial fulfillment of the requirements for the Doctoral degree at the University of Washington, I agree that the Library shall make its copies freely available for inspection. I further agree that extensive copying of this dissertation is allowable only for scholarly purposes, consistent with "fair use" as prescribed in the U.S. Copyright Law. Requests for copying or reproduction of this dissertation may be referred to Bell and Howell Information and Learning, 300 North Zeeb Road, Ann Arbor, MI 48106-1346, to whom the author has granted "the right to reproduce and sell (a) copies of the manuscript in microform and/or (b) printed copies of the manuscript made from microform."

Signature_____

Date_____

University of Washington

Abstract

Inelastic Losses in X-ray Absorption Theory

by Luke Campbell

Chair of Supervisory Committee:

Professor John J. Rehr
Physics

There is a surprising lack of many body effects observed in XAS (X-ray Absorption Spectroscopy) experiments. While collective excitations and other satellite effects account for between 20% and 40% of the spectral weight of the core hole and photoelectron excitation spectrum, the only commonly observed many body effect is a relatively structureless amplitude reduction to the fine structure, typically no more than a 10% effect. As a result, many particle effects are typically neglected in the XAS codes used to predict and interpret modern experiments. To compensate, the amplitude reduction factor is simply fitted to experimental data.

In this work, a quasi-boson model is developed to treat the case of XAS, when the system has both a photoelectron and a core hole. We find that there is a strong interference between the extrinsic and intrinsic losses. The interference reduces the excitation amplitudes at low energies where the core hole and photo electron induced excitations tend to cancel. At high energies, the interference vanishes, and the theory reduces to the sudden approximation. The x-ray absorption spectrum including many-body excitations is represented by a convolution of the one-electron absorption spectrum with an energy dependent spectral function. The latter has an asymmetric

quasiparticle peak and broad satellite structure. The net result is a phasor sum, which yields the many body amplitude reduction and phase shift of the fine structure oscillations (EXAFS), and possibly additional satellite structure. Calculations for several cases of interest are found to be in reasonable agreement with experiment. Edge singularity effects and deviations from the final state rule arising from this theory are also discussed.

The *ab initio* XAS code FEFF has been extended for calculations of the many body amplitude reduction and phase shift in x-ray spectroscopies. A new broadened plasmon pole self energy is added. The dipole matrix elements are modified to include a projection operator to calculate deviations from the final state rule and edge singularities.

TABLE OF CONTENTS

LIST OF FIGURES

Chapter 1

INTRODUCTION

Since their discovery, it has been known that x-rays were absorbed more strongly by some materials than others. However, it was not until the pioneering work of Sayers, Stern, and Lytle in the 1970's that the x-ray absorption spectra of materials began to be used to quantitatively investigate their structure on the atomic level [46, 47]. Since the absorption of x-rays depends only on the immediate environment of the absorbing atom (typically within several atomic diameters) and the spectra is a unique signature of a given material, x-ray absorption becomes a useful tool for investigating the structure of liquids and disordered solids, where traditional diffraction methods do not work. Today, intense beams of modern syncrotrons allow us to probe not only the atomic structure, but also the chemistry and electronic structure of solids and liquids by virtue of the structure present in their x-ray absorption spectra.

The theory has evolved along with the experiment, and has proved a useful tool for interpreting the x-ray spectroscopic experiments. Modern *ab initio* computer codes using multiple scattering theory, developed since the 1980's and continuously improved since then, allow investigators to correlate structural elements in their models with features observed in the experiments [50, 34, 13, 38, 12, 51]. By fitting elements of the theoretical models with measured spectra, interatomic distances can be pinned down to within a few hundredths of an Angstrom, and bond angles, distortions, and several coordination shells can also be measured [35]. Further, the calculations of the electronic properties necessary to give good theoretical results can often give insight

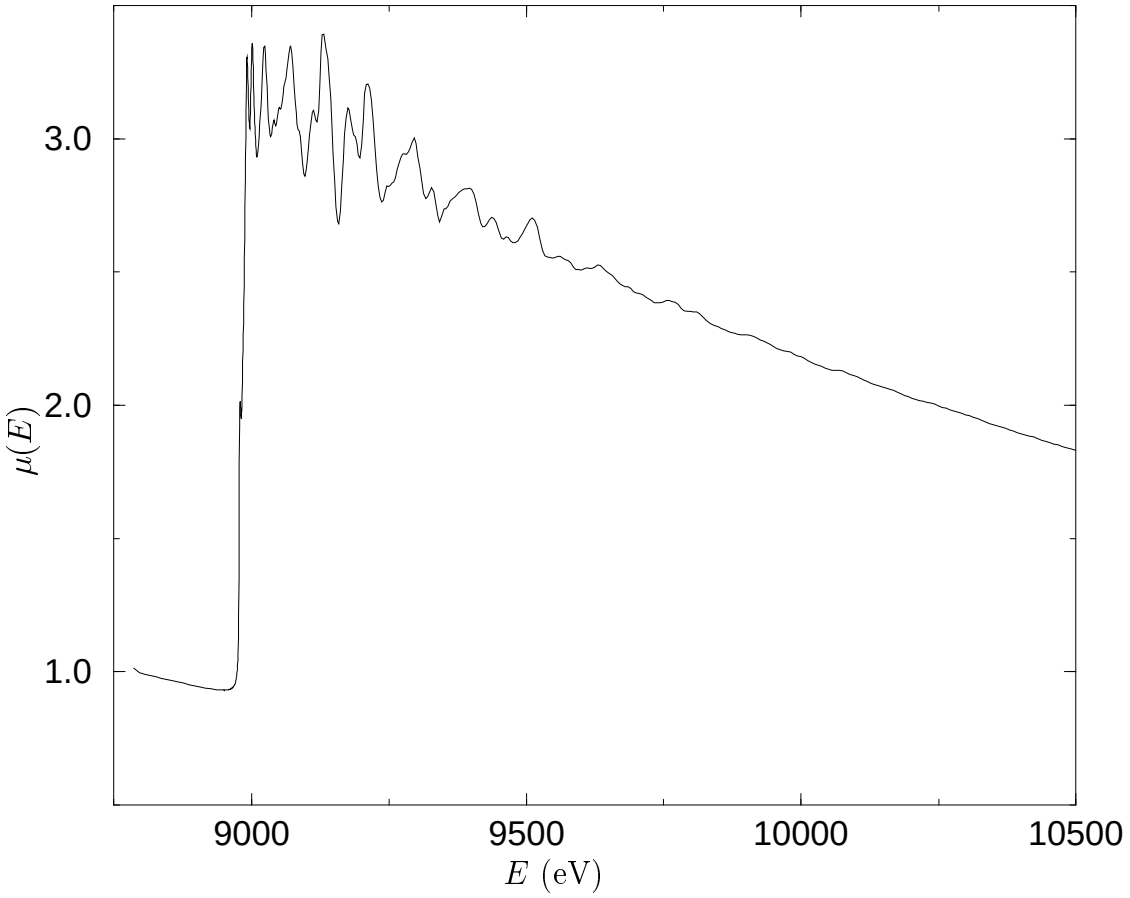

Figure 1.1: The XAS spectrum of the K shell of copper at 10 Kelvin. The edge jump near 9000 eV indicates the transition from the lowest lying (1 S) atomic orbital to a conduction state. The features immediately above the edge comprise the fine structure, which arises from solid state effects.

into what is occurring in the solid, solution, or liquid in question. However, these calculations consistently overestimate the amplitude of the fine structure observed in experiments. This can be corrected at the expense of introducing an adjustable parameter, an overall many body amplitude reduction on the order of 0.9 which corrects for the single electron models employed in the computer codes.

In this dissertation, we develop a general theory of many body effects on x-ray absorption spectra which can account for this amplitude reduction. There is already a considerable body of work on many body effects in spectroscopies of condensed matter systems, particularly as regards the electron quasiparticle. The GW method [26, 32] and the Bethe-Salpeter equation [11] have been quite successful at finding electron energies and lifetimes in materials. However, the theory that is used is largely an effective one electron theory which ignores the loss spectrum of the material. Further, it is not clear how to handle the presence of the core hole in x-ray absorption spectroscopies. That this single particle theory is so effective in x-ray absorption is surprising, since for typical electron densities of solids the collective and multiple particle excitations of both the photoelectron and the core hole can account for 20% to 40% of the spectral density. However, effects of this magnitude are not typically observed in experiments. While there is a history of associating features in the absorption spectra with multi-electron excitations that correspond to energies near the observed features (see, for example, reference [37]), these effects are typically small, and may be confused with other sources, such as the atomic background. Indeed, the only many body effect beyond the quasiparticle approximation which has been unambiguously observed in x-ray absorption spectroscopies is the aforementioned more or less uniform reduction in amplitude to the fine structure signal, on the order of 10% of the signal strength. This amplitude reduction occurs from inelastic effects beyond the quasiparticle approximation. Perhaps as a consequence, there have been no good methods of calculating it.

Also of interest to this dissertation are many particle effects which have been

predicted but which are not yet incorporated in the usual x-ray absorption computer codes. These include the edge singularities, which come about because the "passive" electrons not involved in the transition are projected from states where all the deep atomic levels are occupied to states affected by the potential of the core hole [3, 33, 36, 20]. In real systems, the "singular" behavior is be smeared out due to broadening, and this behavior is often masked by fluctuations in the density of states at the edge, which have their own dips and rises.

1.1 Goals

This work is an attempt at understanding many body inelastic losses in x-ray absorption theory. The primary goals of this dissertation are as follows:

- Explain the observed weakness of many body effects in x-ray absorption spectroscopies.
- Develop a method of calculating the many body amplitude reduction from first principles.
- Predict other many body features that can be observed in x-ray absorption spectroscopy.

In pursuit of these goals, the following tasks and investigations were undertaken:

- Developed a broadened plasmon pole self energy model for the photoelectron.
- Tested the quasi-boson model of interference between core hole and photoelectron losses, and used this to find the loss or excitation spectrum.
- Developed methods for the convolution of the loss spectra with the single electron x-ray absorption spectra to obtain a many body spectrum.

- Modified the dipole matrix element to include edge singularity corrections and deviations from the final state rule.

1.2 Dissertation overview

We begin with a review of the single electron theories of x-ray absorption in Chapter 2. The concepts introduced here will be necessary for much of the following work. Chapter 3 reviews previous work that has been done on inelastic losses in x-ray absorption, and introduces edge singularities and the intrinsic loss spectrum. From there we continue to the extrinsic losses caused by the propagation of the photoelectron in Chapter 4. Chapter 4 includes a discussion of the electron self energy, quasiparticle properties, and the behavior of the extrinsic satellite losses, and introduces a broadened plasmon pole model for the self energy. Chapter 5 then introduces a general theory of losses in x-ray absorption in which both the core hole and the photoelectron are present, and describes the interference between them. In this chapter, the main result of this dissertation is presented, in which the many body x-ray absorption spectrum can be expressed as a convolution of the single electron calculation for the absorption spectrum with a many body spectral function. The methods used to calculate the edge singularity are described in Chapter 6, and results are presented showing the effect of this singularity in copper and titanium. Explicit forms of the intrinsic and interference terms are derived for the plasmon pole electron gas in Chapter 7. The results of calculations based on the quasi-boson model in the plasmon pole electron gas are presented in Chapter 8 for EXAFS (extended x-ray absorption fine structure) spectroscopy and Chapter 9 for the XANES (x-ray absorption near edge spectrum). In the EXAFS region, this model is shown to reproduce the experimental amplitude to acceptable accuracy. Possible many body effects are described that may be observed in the XANES region and one example of this is shown for copper metal. A description of the code developed to perform these calculations is given in Chap-

ter 10. Finally, Chapter 11 wraps up the dissertation with conclusions and future prospects.

1.3 Terminology and basic concepts

The absorption coefficient $\mu(\omega)$ is the basic quantity measured in an x-ray absorption experiment. This is defined as the inverse mean path length for absorption of the x-ray, such that a in incident beam of intensity I_0 and frequency ω decreases in intensity as $I = I_0 e^{-x\mu(\omega)}$. This measured quantity naturally follows from the absorption cross section as $\mu(\omega) = \sum_a \sigma_a(\omega) n_a$ for each atom type a and atomic concentration n_a. Much of the absorption spectrum is dominated by sharp absorption edges, where the incoming photons acquire enough energy to excite deeper core electrons. This atomic picture, without significant solid state effects, is given by a background absorption coefficient $\mu_0(\omega)$. While the location and intensity of these edges can be useful for fingerprinting samples to test for their atomic species, far more information can be garnered from the *fine structure*, a series of fine ripples in the spectrum present from just above an absorption edge and extending to many hundreds of eV beyond the edge. The fine structure spectrum $\chi(\omega)$ is defined as the absorption coefficient with the atomic edge jumps subtracted off, and normalized to the atomic background $\chi(\omega) = (\mu(\omega) - \mu_0(\omega))/\mu_0(\omega)$. There are several commonly used acronyms to describe different types of measurements of these basic quantities:

- XAS - X-ray Absorption Spectrum or X-ray Absorption Spectroscopy, a general term for all x-ray absorption spectroscopies.

- XAFS - X-ray Absorption Fine Structure.

- EXAFS - Extended X-ray Absorption Fine Structure, the fine structure present beyond about 40 eV from the edge.

- XANES - X-ray Absorption Near Edge Structure, the absorption coefficient in the vicinity of an edge, up to approximately 40 eV above the edge.

When an x-ray is absorbed, it excites a *photoelectron* from a core level of the absorbing atom, leaving behind a relatively long lived *core hole*. Most of the excess energy of the x-ray photon beyond that necessary to promote the core electron to a conduction state goes into the kinetic energy of the photoelectron, but some of the x-ray energy can be sapped away by excitations of the system. In atoms, when this excitation is a re-arrangement of the bound state occupation of the absorbing atom, it is called a *shake-up* transition, when the excitation involves a bound valence or shallower core electron escaping to the continuum, it is called a *shake off* transition. In condensed systems (solids, solutions, and liquids), excitations can take the form of a whole zoo of collective modes. The dominant excitation, however, is the *plasmon* state. A plasmon is a quantized charge density wave that can propagate through the system. There is a minimum energy necessary to excite a plasmon corresponding to a minimum frequency known as the *plasma frequency*, which is given the symbol ω_p. Below this energy, the dominant excitation is the separation of electron-hole pairs. Those excitations which are inherent in the creation of the core hole are said to be *intrinsic*. The excitations which occur after the core hole creation as a result of the propagation of the photoelectron in the system are *extrinsic*. These two processes are not independent when they occur together such that you cannot simply add their amplitudes, the modification of the excitations that occurs when both a core hole and a photoelectron are present is known as *interference*. The excitations of a system, including the promotion of the photoelectron from the core level, can be described by a *spectral function*, or excitation spectrum, which is given the symbol $A(k, \omega)$. This is the probability density of finding the system in any given momentum state k of the photoelectron, and overall energy ω of the entire system.

In this thesis, we will everywhere use *atomic units*, where $|e| = \hbar = m_e = 1$. This simplifies the notation. When necessary, the correct symbols can be put back in the equations by dimensional analysis. In the system of atomic units, the unit of energy is the *Hartree*, such that 1 Hartree = 27.2 eV; and the unit of distance is the *Bohr*, with 1 Bohr = 0.529 Å.

Chapter 2

SINGLE ELECTRON THEORY OF X-RAY ABSORPTION

Before delving into the complexities of the effects of many particle excitations on x-ray absorption, it is useful to review the single electron theory of this subject. This not only serves as an introduction to the field, but the current work builds on the single electron theory, so that an understanding of this theory, or at least its main results, are necessary to proceed. Because this section is merely a review of those results which are important to the main thrust of the thesis, many details which are important to the theory of x-ray absorption but irrelevant to this work will be left out. The interested reader is encouraged to review the literature already published elsewhere; references [44] and [7] make a good starting point.

As a beam of electromagnetic radiation of initial intensity I_0 and frequency ω passes through a homogeneous material, its intensity decreases exponentially with the distance x

$$I = I_0 e^{-x\mu(\omega)}. \tag{2.1}$$

Here, $\mu(\omega)$ is called the *absorption coefficient*. This coefficient is related to the cross section for absorption in a simple way

$$\mu(\omega) = \sigma(\omega)n \tag{2.2}$$

where n is the concentration of the absorbing atoms.

The absorption cross section is traditionally represented via a golden rule formalism in the dipole approximation, which is derived, e.g., in Sakuri sections 5.6-5.7 ([45])

$$\sigma(\omega) = \frac{4\pi^2\omega}{c} \sum_f |\langle f|\hat{\varepsilon}\cdot\mathbf{r}|i\rangle|^2 \delta(E_f - E_i - \omega). \tag{2.3}$$

In the above expression, $\hat{\varepsilon}$ is the direction of photon polarization, $\mathbf{r}$ is the position operator, while i and f stand for the occupied initial and unoccupied final electron states, respectively, with energies E_i and E_f. For convenience, we define the *dipole operator* $\Delta_\varepsilon = \hat{\varepsilon} \cdot \mathbf{r}$, and note that by simply replacing this operator by its relativistic form $\Delta_\varepsilon = ce^{i(\mathbf{k}\cdot\mathbf{r})}\hat{\varepsilon} \cdot \vec{\alpha}$ we obtain the relativistic form of the absorption cross section.

We note in passing that the states $|i\rangle$ and $|f\rangle$, along with their respective energies, can be calculated in crystalline solids using conventional band structure approaches. However, that is not the method we choose to use. To proceed further, we introduce the one electron Green's function

$$G(E) = (E - H + i\delta)^{-1} = \sum_f \frac{|f\rangle\langle f|}{E - E_f + i\delta} \tag{2.4}$$

where δ is a positive infinitesimal and H is the full one electron Hamiltonian. In particular we note that

$$\mathrm{Im}\, G(E) = -\pi \sum_f |f\rangle\langle f|\delta(E - E_f). \tag{2.5}$$

This has the interpretation that for a state with quantum number denoted by $\mathbf{k}$

$$\mathrm{Im}\, \langle \mathbf{k}|G(E)|\mathbf{k}\rangle = -\pi \sum_f |\langle \mathbf{k}|f\rangle|^2 \delta(E - E_f) = -\pi A(\mathbf{k}, E). \tag{2.6}$$

That is, the imaginary part of the Green's function gives the probability density A for a particle in state $\mathbf{k}$ to be found in an infinitesimal interval of energy around the energy E. A simple substitution of Eq. 2.5 into Eq. 2.3, and recognizing that only final states with $E_f > \mu_F$ are allowed, then shows

$$\sigma(\omega) = -\frac{4\pi\omega}{c}\mathrm{Im}\, |\langle i|\Delta_\varepsilon^\dagger G(\omega + E_i)\Delta_\varepsilon|i\rangle|\theta(\omega + E_i - \mu_F) \tag{2.7}$$

where the chemical potential is given the symbol μ_F. We can generalize this to include lifetime effects by replacing $i\delta$ in Eq. 2.4 with a finite positive $i\Gamma(E)$ corresponding to the lifetime of the core hole final state. This merely gives Lorentzian broadening to the absorption spectrum.

2.1 The EXAFS path expansion

At this point, we separate the electron Hamiltonian into two parts, $H = H_0 + V_{\rm sc}$. H_0 is taken as the free electron Hamiltonian plus a constant potential $H_0 = -\frac{1}{2}\nabla^2 + E_0$, while $V_{\rm sc}$ is a sum of atomic potentials $V_{\rm sc} = \sum_i v_i$, where the index i labels each individual atom. For our purposes, we can assume that the atomic potentials are spherically symmetric. While a full potential approach is possible in principle, it has proven to be difficult to implement, and only gives significant corrections within a few eV of the threshold for absorption. The Green's function can now be expanded using the Dyson equation into a perturbation series

$$G = G_0 + \sum_i G_0 v_i G_0 + \sum_{i,j} G_0 v_i G_0 v_j G_0 + \cdots. \tag{2.8}$$

To avoid calculating the multiple scattering expansion within each cell i, we define the t matrix as $t_i = v_i + v_i G_0 t_i$. This allows us to sum the terms in the perturbation series to all orders at each site. For spherical potentials, the t matrix is easily expressed in terms of the partial wave phase shifts, such that in the basis of angular momentum and atomic positions and with spherically symmetric potentials we get $\langle L|t_j|L'\rangle = e^{i\delta_{l,j}} \sin(\delta_{l,j})\delta_{LL'}$. The perturbation expansion can then be re-summed into a multiple scattering series

$$G = G_0 + \sum_i G_0 t_i G_0 + \sum_{i\neq j} G_0 t_i G_0 t_j G_0 + \cdots. \tag{2.9}$$

We now solve the central atom Green's function exactly

$$G_c = G_0 + G_0 t_c G_0 \tag{2.10}$$

where the subscript c denotes the central, or absorbing, atom. Given this, we express the full Green's function as

$$G = G_c + G_{\rm sc} \tag{2.11}$$

where the scattering Green's function is

$$G_{\rm sc} = G_c \left[\sum_{i\neq c} t_i + \sum_{i\neq j\neq c} t_i G_0 t_j + \cdots \right] G_c. \tag{2.12}$$

For spherical potentials, the angular momentum basis is convenient, so can express our Green's functions in this basis.

$$G_{\rm sc}(\mathbf{r},\mathbf{r}',\omega) = -2p\sum_{L,L'} R_L(\mathbf{r})G^{\rm sc}_{L,L'}(\omega)R_{L'}(\mathbf{r}') \quad (2.13)$$

$$G_c(\mathbf{r},\mathbf{r}',\omega) = -2p\sum_{L} R_L(r_<)\left[N_l(r_>)+iR_l(r_>)\right]Y_L(\hat{r})Y^*_L(\hat{r}') \quad (2.14)$$

Here, $p=\sqrt{2(E-E_0)}$, R_l and N_l are the regular and irregular solutions to the radial Shrödinger equation for the potential v_c, and $R_L(\mathbf{r}) = i^l e^{i\delta_l}R_l(r)Y_L(\hat{r})$. These radial wave functions are scattering state normalized to $R_l = \cos(\delta_l)j_l(kr)+\sin(\delta_l)n_l(kr)$, $N_l = -\sin(\delta_l)j_l(kr)+\cos(\delta_l)n_l(kr)$. The relativistic form of this equation can be recovered by replacing the solutions to the Schrödinger equation with those from the Dirac equation, and summing over the spinor indices [6].

Now, by representing the angular momentum resolved free particle Green's function between different atomic sites with, for example, the Rehr-Albers separable representation

$$G_{Li,L'j} = \frac{e^{ip|\mathbf{R_i}-\mathbf{R_j}|}}{p|\mathbf{R_i}-\mathbf{R_j}|}\sum_{\lambda} Y_{L\lambda}(\frac{\mathbf{R_i}-\mathbf{R_j}}{|\mathbf{R_i}-\mathbf{R_j}|})\tilde{Y}_{L\lambda}(\frac{\mathbf{R_i}-\mathbf{R_j}}{|\mathbf{R_i}-\mathbf{R_j}|}) \quad (2.15)$$

the scattering Green's function can be fully calculated. The details of calculating the quantities $Y_{L\lambda}(\hat{r})$ are left to the paper by Rehr and Albers [43], but it will be pointed out here that the $Y_{L\lambda}(\hat{r})$ decrease in importance with increasing λ; and usually calculating up to $\lambda = 6$ is sufficient. Merely retaining the first term in the λ expansion is equivalent to taking the plane wave approximation.

Inserting our representation for the Green's function, Eq. 2.11, into the formula for the absorption cross section 2.7, we find

$$\sigma(E) = -\frac{4\pi\omega}{c}\mathrm{Im}\,|\langle i|\Delta^\dagger_\varepsilon|R_L\rangle(-i\delta_{L,L'}+e^{i(\delta_l+\delta_{l'})}G_{\rm sc}(\omega+E_i)\langle R_{L'}|\Delta_\varepsilon|i\rangle| \quad (2.16)$$
$$\times\theta(\omega+E_i-\mu_F).$$

Physically, this multiple scattering expansion represents an electron ejected from the absorbing atom and scattering off of its neighbors before scattering back to the absorbing atom once again. The first term containing only G_c is the background absorption

from the central atom alone. Subsequent terms, from the expansion of the scattering Green's function G_{sc}, represent the electron scattering off one, two, or more neighboring atoms before returning, with the prohibition that the electron cannot scatter off of the same atom twice in a row (although it may return to a given atom after visiting yet another atom). The change to the central atom absorption is caused by the interference of all the electron waves returning to their origin after being reflected from other atoms in the material.

At this point, it is easy to see that the absorption consists of an atomic contribution from the central atom alone (μ_0) and a contribution from scattering off neighboring atoms ($\mu_0\chi$), such that the total absorption is expressed as

$$\mu(E) = \mu_0(E)[1 + \chi(E)]. \tag{2.17}$$

The bare atom absorption μ_0 is not the absorption from an isolated atom, as its electron configuration has been altered by the potentials of its neighbors. While this shows some solid state effects, it is primarily the fine structure signal χ that is used to determine the structural properties of the solid. Because χ comes about from scattering of nearby atoms, it contains information about the distances, bond angles, and coordination numbers of the neighboring atoms, and as such is a useful probe of condensed systems.

In the single electron approximation, it can be shown [46] that the EXAFS signal can be expressed as a sum over sinusoidal signals from each distinct multiple scattering path

$$\chi(k) = \sum_i S_0^2 N_i \frac{|f(k)|}{kR_i} \sin(2kR_i + 2\delta_c + \phi(k)) e^{-2\sigma_i^2/k^2 - 2R_i/\lambda(k)}, \tag{2.18}$$

where the sum is over all possible scattering paths i, R_i is half the total path length, N_i is the number of crystalographically indistinguishable paths, $f(k) = |f(k)|e^{i\phi(k)}$ is the curved wave backscattering amplitude, δ_c is the central atom partial-wave phase shift, $\lambda(k)$ is the mean free path of the electron in the solid, σ_i is the root mean square fluctuation in the total path length called the *Debye-Waller factor*, and $k =$

$\sqrt{2(\omega - E_F)}$ is the EXAFS wavenumber for photon energy ω and Fermi energy E_F (note that in EXAFS terminology, k is not the photoelectron momentum). Of most importance to this thesis, however, is the factor S_0^2. This factor was put in as a way of dealing with many body effects in a single particle theory. S_0^2 is assumed to be structureless, a simple constant that gives an overall reduction in amplitude to the EXAFS oscillations. While the inclusion of the mean free path λ is a many body effect, it is one that can be handled by this single particle theory by introducing a finite imaginary part $i\Gamma_{\mathbf{k}}$ to the denominator of the Green's function in Eq. 2.4, where $\lambda(k) \approx p/\Gamma_{\mathbf{k}}$ for photoelectron momentum p. Another many body effect already present in the standard single particle theory is an energy dependent shift in the energy in the denominator of the Green's function. These two corrections are, in fact, the real and imaginary parts of the complex on-shell self energy $\Sigma(\mathbf{k}, k^2/2) = \Delta E_{\mathbf{k}} - i\Gamma_{\mathbf{k}}$, such such that $G(\mathbf{k}, E) = (E - k^2/2 - \Delta E_{\mathbf{k}} + i\Gamma_{\mathbf{k}})^{-1}$. Because of their importance to the current work, explicit instructions for calculating these two terms will be given in later sections.

Although the sum in Eq. 2.18 is formally over all possible scattering paths, only a few yield any significant contribution. Away from the Fermi level, the finite mean free path cuts off any long paths, while many other paths are eliminated simply because their effective curved wave backscattering amplitude is small. Although there are a very large number of paths with small amplitudes, they add to the signal with essentially random phases, and so largely cancel and contribute mostly small amplitude noise. In practice, in the EXAFS region starting about 20 to 30 eV above the edge and continuing up to several hundred eV, on the order of ten to twenty paths are sufficient to get to within a few percent of the fully converged result, a precision which is within the experimental noise [51]. From a theoretical perspective, currently all of the parameters in the EXAFS equation 2.18 except for S_0^2 can be computed *ab initio* once the basic structure is known, although σ_i^2 is, in many cases, not at all trivial to compute. Full *ab initio* calculations of σ_i^2 often involve quantum chemistry

calculations to find force constants between the atoms for input either into a molecular dynamics simulation [16] or an equation of motion or recursion method model [39], [40]. However, in crystalline solids, the correlated Debye model will usually give sufficiently accurate results [48], provided a reliable value of the Debye temperature is available. For the other parameters, computer programs such as the *ab initio* code FEFF, which uses the methods described in this chapter, are available that will calculate the EXAFS spectrum once a particular geometry of the atoms in the solid is given [5].

If some of the parameters in the EXAFS equation 2.18 are not known, they can be fitted, up to the information content in the EXAFS signal given by $\Delta N = \Delta k \Delta R/\hbar$. This is a common procedure, and codes such as FEFFIT are available to make this procedure relatively painless [35]. This allows structural parameters such as bond lengths and bond angles to be extracted from experimental data. EXAFS is particularly suitable for such a fitting, for when the Fourier transform is taken of the EXAFS equation 2.18, the result is a number of more or less sharp peaks corresponding to each scattering path, and whose coordinate R conjugate to the variable k in the transform closely approximates the actual half path length of the scattering path in question. Simple methods such as phase correcting for the partial wave phase shifts and dividing by the backscattering amplitude $|f(k)|$ will both sharpen up the peaks and put these peaks at a coordinate R equal to the half path length for one given path. Because it is usually only the first few paths which are necessary to extract all the relevant information, filtering the Fourier transform to include only the first few paths will reduce the parameters needed to be fit down to a mere handful. In fact, one can often simply use the first scattering path off of the nearest neighbors to extract the structural quantities of interest. Unfortunately, since until now there has been no way to estimate S_0^2 beforehand, one is left with two correlated parameters that affect the overall amplitude of a path - the amplitude reduction factor S_0^2 and the coordination number N. If the coordination number of a path is known from

the crystal structure or other information about the geometry, there is of course no problem. However, since S_0^2 is typically a number between 0.8 and 1, one will be left with a 10% uncertainty when trying to fit an unknown coordination number of any given path. Because EXAFS does not depend on long range order, it is a useful tool for studying disordered materials and liquids, but it is in just such systems where the coordination number will not necessarily be known.

2.2 Full multiple scattering and the XANES region

Near the Fermi level, the extrinsic mean free path becomes much longer, and in fact becomes infinite at the Fermi level, although the total lifetime of a state is still limited by the core hole lifetime, leading to a proliferation of long paths. Further, the path expansion of XAFS diverges in the so called X-ray Absorption Near Edge Structure (XANES) region even for finite mean free paths, and another method must be used. One method that has proved successful is a formal inversion of Eq. 2.9, i.e., [5]

$$G = G_0(1 - tG_0)^{-1} = (1 - tG_0)^{-1}G_0. \tag{2.19}$$

The Green's function G_0 and the t operator can be represented as complex, non sparse matrices in a vector space spanned by the basis of local scattering state angular momenta and atomic coordinates $|L, R_i\rangle$. Only a few angular momentum states are needed for each atom; the finite size of the atom means that at low values of the photoelectron momentum only small values of l are important. However, because of the long mean free path, large numbers of sites may be needed to converge to the result from a macroscopic system. As a consequence large matrices need to be inverted. Modern computers can handle matrices as large as about $10^4 \times 10^4$, so that sufficiently large clusters can at least be held in memory, but the time to invert a matrix typically scales as the dimension of the matrix to the third power. As a result, full multiple scattering calculations can be time consuming. Nevertheless, they often give superior results to the path expansion in the near edge region of the XAFS spectrum. It

is in this near edge region that accurate atomic potentials are the most important, so that self consistent potentials must be implemented, and currently methods of generating self consistent non-spherical potentials are a field of much interest. It is, indeed, fortunate that thermal effects are least important at these low energies, since no method has been found for full multiple scattering procedures to correctly take the Debye-Waller factors fully into account, and performing a configurational average over a thermal ensemble of the system is prohibitively time consuming. As computers speed up, however, full multiple scattering calculations become faster and faster; especially since they are easily parallelizable for implementation on networked clusters [14]. Furthermore, new matrix inversion routines optimized for this problem have also decreased the time required [4].

The *final state rule* is the prescription for calculating the quasiparticle contribution to the XAS using a fully relaxed core hole as the final state. While this makes physical sense, it neglects multi-electron excitations that are the main subject of this dissertation. In some cases the *initial state rule* of calculating the XAS without a core hole in the final state more accurately reproduces experiment. While this choice of the final state has little effect on the EXAFS, there can be significant differences in the near edge region, especially for the L and M edges.

The region near threshold often has a rather complicated edge structure. Because of the divergence of the EXAFS equation, features in the XANES region are often no longer explained by multiple scattering paths. Rather, we harken back to Fermi's golden rule, and look to the angular momentum projected density of states to explain the XAS spectra after suitable modification by the dipole matrix elements. Where an orbital or band into which the photoelectron can be ejected piles up a lot of density (after considering the dipole selection rules limiting angular momentum changes), the absorption will be high. When this sort of feature occurs at the edge, it is called a *white line*. Because the d shell electrons form bands highly localized in energy, they will have a high density of states over their energy range. In the transition metals,

the d shell is only partially filled, so that the Fermi level occurs inside the d band and strong white lines are common at the L_2 edges, with a lesser white line at the L_3 edge. Where there is a lack of a suitable orbital or band with an allowed angular momentum quantum number l, the absorption stays small even though there is sufficient energy to promote a core electron to above the Fermi level. This feature is often called a *dark line*. Further, it is not uncommon to find a very sharp feature just before the main edge, referred to as a *pre-edge feature*, which is commonly attributed to a very high density of states from a localized band or molecular orbital located just below the Fermi level.

2.3 FEFF

The one electron XAS calculations performed in this thesis used the computer program FEFF [5]. This program is fully *ab initio*, using full potential methods to calculate self consistent potentials for the scattering centers, and from these, determine the scattering phase shifts. From there, FEFF calculates the XAS using the real space multiple scattering and full multiple scattering routines described previously in this chapter. Because it works in real space, it can be used on amorphous or disordered materials as well as crystals.

In addition to EXAFS and XANES, FEFF calculates x-ray magnetic circular dichroism (XMCD) and non-resonant x-ray emission spectra (XES), and performs electronic structure calculations including the angular momentum resolved density of states (LDOS) which are useful for interpreting XANES spectra. Although not the main output of this program, FEFF finds the dipole matrix elements as part of its computational process. These FEFF derived matrix elements are used in this dissertation for the calculation of edge singularities.

2.4 Ending comments

Although the quasiparticle approximation employed in developing the theories presented in this chapter has been useful for XAS theory codes such as FEFF, the theory nevertheless remains incomplete, as evidenced by adjustable parameters such as the many body amplitude reduction S_0^2. In the next chapter, we present an overview of the many body effects intrinsic in the promotion of the core electron into a photoelectron and a core hole.

Chapter 3

INTRINSIC LOSSES IN X-RAY ABSORPTION

In this chapter, we reveiw previous work that has been done on inelastic losses in x-ray absorption. In the process, we introduce the many body spectral function and show how the intrinsic losses can modify the single particle XAS through a convolution with the many body spectral function. Further, we show how many body effects lead to edge singularities.

In a real solid, the many body final states after the absorption of a photon are excitations of a system with on the order of 10^{23} nuclei and electrons. The energy of the photon will then be distributed over all the modes of this system allowed by conservation laws. Many of these excitations display particle-like behavior, and when one of these so called *quasiparticles* dominates, the physical response approaches the single particle theory described in the previous section. In condensed systems, the quasiparticle excitations in the system can be conceptually thought of as that of a single electron "dressed" by its interaction with the solid. This alters its energy and gives it a finite lifetime, represented in the single particle formalism with the addition of a complex self energy. However, one must keep in mind that in general there will be additional collective excitations.

In a many body system, the single particle expression for Fermi's golden rule (equation 2.3) is should be replaced by a sum over all allowed final states of the many body system

$$\sigma(\omega) = \frac{4\pi^2\omega}{c} \sum_n |\langle \Psi_n'^N | \Delta_\varepsilon^N | \Psi_i^N \rangle|^2 \delta(E_n - E_i - \omega). \tag{3.1}$$

Here, $|\Psi_n'^N\rangle$ is a final many body state of N electrons in the presence of the core

hole and in an excitation state n, and $|\Psi_i^N\rangle$ is the initial many body state, usually assumed to be the ground state of the many body system $|\Psi_0^N\rangle$. The many body dipole operator Δ_ε^N can be expressed as

$$\Delta_\varepsilon^N = \sum_{i,f} \Delta^{i,f}(\varepsilon) a_f^\dagger a_i \tag{3.2}$$

where the destruction operator a_i removes an electron from state i, the creation operator $a_f^\dagger$ makes an electron in state f, and $\Delta^{i,f}(\varepsilon)$ is the dipole matrix element between two single particle states.

A traditional approach for calculating the many body effects on the x-ray absorption spectrum is to use a separable representation of the many body wave function

$$H_N = H_{N-1} + h \tag{3.3}$$

for the many body Hamiltonian for the N electron system H_N and the single electron Hamiltonian h. This is referred to as the *sudden approximation*, which comes ultimately from the assumption that the photoelectron leaves quickly in some sense, such that the system does not have time to respond to its potential as it exits. With this approximation, the many body wave function can be factorized into a term containing the interacting many body wave function of $N-1$ electrons and a photoelectron state with quantum number k.

$$|\Psi^N\rangle = |\Psi^{N-1}\rangle|k\rangle. \tag{3.4}$$

The many body matrix element $M_n = \langle \Psi_n'^N | \Delta_\varepsilon^N | \Psi_0^N \rangle$ then becomes

$$M_n = \langle f | \Delta_\varepsilon^{i,f} | i \rangle \langle \Psi_n'^{N-1} | \Psi_0^{N-1} \rangle. \tag{3.5}$$

Now, we follow Rehr *et al* (1978) [42] and define the many body overlap integral

$$S_n = \langle \Psi_n'^{N-1} | \Psi_0^{N-1} \rangle. \tag{3.6}$$

Then our many body absorption cross section becomes

$$\sigma(\omega) = \frac{4\pi^2\omega}{c} \sum_n S_n^2 M_n^2 \delta(E_n - E_i - \omega) \tag{3.7}$$

and thus the many body absorption spectrum is

$$\mu(\omega) = \sum_n S_n^2 \mu^0(\omega - E_n) \tag{3.8}$$

$$= \int d\omega' A_{intr}(\omega') \mu^0(\omega - \omega'). \tag{3.9}$$

Here, $A_{intr}(\omega')$ is the *intrinsic spectral function*, the probability density of finding the system in some particular excitation energy ω'. This process is called intrinsic because it is inherent in the excitation of the absorbing atom into a core level hole state and photoelectron. This is opposed to extrinsic excitations, which occur after the production process and typically result from excitations of the system by the fast moving photoelectron.

The intrinsic spectral function of an atomic system consists of several discrete delta function peaks corresponding to the first several excitation overlap probabilities S_n which, past a certain energy, give way to a continuum of excitations. The delta function peaks are called shake-up processes and result from transitions between the bound states in the atom, while the continuum is called shake-off, and refers to the ejection of an electron from an atomic bound state into an unbound state.

From Eq. 2.17, we see that the EXAFS signal can be expressed as $\chi(\omega) = [\mu(\omega) - \mu_0(\omega)]/\mu_0(\omega)$. Because the embedded atom background μ_0 is smoothly varying away from the edge, and because $\sum_n S_0^2 = 1$, we can approximate $\mu_0 \approx \mu_0^0(\omega) \sum_n S_n^2 = \mu_0^0(\omega)$, where μ_0^0 is the single electron background. Given this approximation, the EXAFS signal is given by a phasor sum

$$\chi(\omega) = \sum_n S_n^2 \chi^0(\omega - E_n). \tag{3.10}$$

Of all the overlap factors, the ground state overlap S_0^2 usually dominates in atoms and molecules. Because the EXAFS signal for a given scattering path is sinusoidal (equation 2.18), all the other overlaps contribute with rapidly varying phases which tend to cancel. This leads to a signal reduced in amplitude by the ground state

overlap

$$\chi(\omega) = S_0^2 \chi^0(\omega). \tag{3.11}$$

This is the justification for the constant amplitude reduction factor in equation 2.18. Starting from this historical definition, any amplitude reduction from the single body result has come to be known as S_0^2, and it is this latter definition that will be used throughout this thesis.

In condensed systems, there will be additional collective excitations of the medium that can be observed. In particular, the sudden polarization of the medium from the appearance of the positively charged core hole can excite plasmons and particle hole pairs. The plasmon oscillations are characterized by a minimum frequency at zero wavenumber known as the plasma frequency ω_p, which depends on the density of electrons n in the system

$$\omega_p = \sqrt{4\pi n}. \tag{3.12}$$

When the absorbed photon carries enough energy to excite a plasmon, the plasmons will dominate the extended many body response. When there is insufficient energy to excite plasmons, the dominant non-quasiparticle contribution to the spectrum arises from the creation of particle-hole pairs, analogous to the shake-up and shake-off rearrangements of atomic systems. In condensed systems, intrinsic spectral function no longer contains delta functions of atomic overlaps because of broadening with the quasiparticle lifetime. In this case, the largest contribution to the phasor sum in Eq. 3.10 is the quasiparticle peak centered at zero excitation energy.

Now, while the final many body state $|\Psi_n'^{N-1}\rangle$ may not be affected by the dynamics of the quasiparticle, it is influenced by the presence of the positively charged core hole left behind. It was shown by Anderson [3] that as $N \to \infty$, the many body ground state in the presence of a core hole (or any other scattering impurity) is orthogonal to the many body ground state without the core hole, so

$$\langle \Psi_0'^{N-1} | \Psi_0^{N-1} \rangle = S_0^2 = 0. \tag{3.13}$$

This is also true for any excited state overlap S_n, and is referred to as the "orthogonality catastrophe". The resolution of this catastrophe is that in a bulk system, the atomic bound states are spread out into bands and the delta function peaks of the atomic intrinsic spectral function become a continuum of excitations over the bands. Thus, while the contribution from any individual excited state overlap vanishes, we must sum over all excited states so that in any small region of energy above $\omega' = 0$ there is a finite contribution.

Nevertheless, the orthogonality catastrophe theory predicts there is a singular rise or loss of absorption intensity at threshold. This was suggested by Mahan [33], while Friedel [20] extended the analysis to include "replacement" and "shake-off" terms to first order in the scattering potential of the core hole. It has been shown by Nozières and De Dominicis [36] that an exact solution of the absorption problem for free conduction electrons in the presence of a non-degenerate structureless core hole gives rise to a power law singular structure in the x-ray absorption spectrum varying as

$$\mu \propto (\omega - \mu_F)^{-\alpha_l} \tag{3.14}$$

near the threshold at the chemical potential μ_F, where

$$\alpha_l = 2\frac{\delta_l}{\pi} - 2\sum_l (2l+1)\left(\frac{\delta_l}{\pi}\right)^2 . \tag{3.15}$$

The notation l is used to indicate the angular momentum state of the photoelectron, and δ_l the phase shift of the core hole potential for state l. It predicts that the absorption at threshold is either infinite (for $\alpha_l > 0$) or zero (for $\alpha_l < 0$). In any real system, lifetime broadening will smear out any such singularity, in which case these effects manifest as edge enhancements or reductions in the spectrum. Because the density of states at an absorption edge often undergoes pronounced fluctuations for a given angular momentum, it is difficult to pick out edge singularity effects from the peaks or valleys of the single particle density of states.

Friedel [20] has identified three types of transitions which give rise to these edge singularity effects:

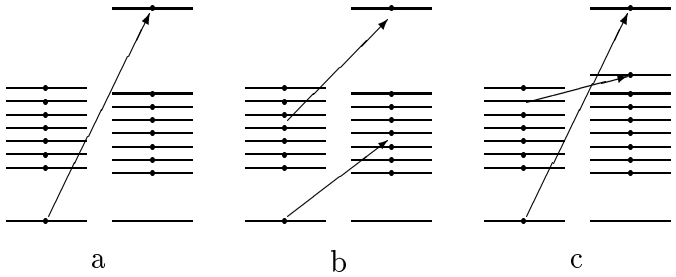

In the figure above, diagram **a** illustrates the direct transition, and diagram **b** a replacement transition. Diagram **c** shows the shake-up and shake-off transitions. Equations 3.15 and 3.14 take all three of these transitions into account, for absorption near an edge. However, while the shake-up and shake-off transitions of diagram **c** can be described away from the edge by equation 3.9, there is no such description for the projection of the direct and replacement initial and final states. One of the goals of this dissertation is to derive expressions for all of these many body effects at all energies, and these will be described in subsequent chapters.

This concludes the introduction to intrinsic many body effects in XAS. In the next chapter we will investigate another source of inelastic losses in x-ray absorption - the extrinsic losses caused by the propagation of the photoelectron.

Chapter 4

EXTRINSIC LOSSES IN X-RAY ABSORPTION

In this chapter, we derive the photoelectron self energy using a broadened plasmon pole model, which reduces to the Hedin-Lundqvist self energy [31] in the limit of zero broadening. The photoelectron quasiparticle properties are found from this self energy, the extrinsic spectral function is calculated, and a method of finding the extrinsic satellite spectral function is discussed.

After the photoelectron has been ejected from the absorbing atom, it interacts with the surrounding medium to create additional collective excitations of the system. As described in chapter 3, the interactions lead to a change in the properties by which the electron propagates, turning what was a bare, freely propagating electron into a quasiparticle with an effective mass and finite lifetime. Both the quasiparticle and the collective excitations can be described by a complex momentum and energy dependent *self energy* $\Sigma(\mathbf{k},\omega)$. With the inclusion of the self energy, we can write the one electron Green's function for a quantum number $\mathbf{k}$ as

$$G(\mathbf{k},\omega) = (\omega - \epsilon_{\mathbf{k}} - \Sigma(\mathbf{k},\omega) + i\delta_{\mathbf{k}})^{-1} \tag{4.1}$$

where $\delta_{\mathbf{k}}$ is a positive infinitesimal for $|\mathbf{k}| > k_F$ and a negative infinitesimal for $|\mathbf{k}| < k_F$. Reminding ourselves of equation 2.6 and its interpretation, we find that $|\mathrm{Im}\, G(\mathbf{k},\omega)|/\pi = A(\mathbf{k},\omega)$ gives the probability for the entire interacting system including the photoelectron to be in a particular energy ω at any given value of the quantum number $\mathbf{k}$. If we assume that the self energy varies slowly near the point where $\omega = \epsilon_{\mathbf{k}} + \Sigma(\mathbf{k},\omega)$, it is easy to see that we get a Lorentzian-like peak in our spectral density function A in the vicinity of $\epsilon_{\mathbf{k}} + \Sigma(\mathbf{k},\epsilon_{\mathbf{k}})$. This is the quasiparticle

resonance, indicating that the system has a large probability to be in a narrow range of energies for a given $\mathbf{k}$. Due to the variation in Σ in the region of the quasiparticle, the lineshape will not be a true Lorentzian, but will rather have some more or less pronounced Fano-like asymmetry. Depending on the nature of the self energy function, in addition to the quasiparticle we may also get definite peaks far from the quasiparticle. These peaks are called satellites, and indicate a significant probability that the system contains other excitations in addition to the photoelectron. We will go into more details about the nature of the spectral function and the quasiparticle later, but first we must investigate the self energy.

4.1 The GW self energy in the plasmon pole electron gas approximation.

As shown by Hedin [22], the self energy for a system of interacting electrons and nuclei can be written as

$$\Sigma(\mathbf{k},\omega) = i\int \frac{d^3q\, d\omega'}{(2\pi)^4} G(\mathbf{k}-\mathbf{q},\omega-\omega')W(\mathbf{q},\omega')\Gamma(\mathbf{k},\mathbf{q},\omega,\omega'). \tag{4.2}$$

The interaction W is a coulomb potential dynamically screened by the medium. We can represent this as

$$W(\mathbf{q},\omega') = v(q)/\epsilon(\mathbf{q},\omega') = v(q)/(1-v(q)P(\mathbf{q},\omega')) \tag{4.3}$$

where $v(q) = 4\pi/q^2$ is the Coulomb potential, ϵ is the dielectric function and P is the polarization operator

$$P(\mathbf{q},\omega') = -i\int \frac{d^3k\, d\omega}{(2\pi)^4} G(\mathbf{k},\omega)\Gamma(\mathbf{k},\mathbf{q},\omega,\omega')G(\mathbf{k}-\mathbf{q},\omega-\omega'). \tag{4.4}$$

The quantity Γ is the *vertex correction*. The GW approximation of Hedin [22] is so called because to a good approximation $\Gamma(\mathbf{k},\mathbf{q},\omega,\omega') = 1$, and thus we only use the Green's function G and the screened interaction W in the computation of the self energy.

The density correlation function $S(\mathbf{q},\omega')$ is a charge density fluctuation propagator that can be expressed as

$$S(\mathbf{q},\omega') = [1/\epsilon(\mathbf{q},\omega') - 1]/v(q). \tag{4.5}$$

Using this form, we can separate the self energy into an exchange term and a term arising from density fluctuations

$$\Sigma_{ex}(\mathbf{k},\omega) = i\int \frac{d^3q\, d\omega'}{(2\pi)^4} G(\mathbf{k}-\mathbf{q},\omega-\omega')v(q) \tag{4.6}$$

$$\Sigma_{d}(\mathbf{k},\omega) = i\int \frac{d^3q\, d\omega'}{(2\pi)^4} G(\mathbf{k}-\mathbf{q},\omega-\omega')S(\mathbf{q},\omega')v(q)^2. \tag{4.7}$$

The exchange part of the self energy is simply the static Hartree-Fock exchange potential, which in the free electron gas is

$$\Sigma_{ex}(k) = -\frac{2}{\pi}\left[\frac{k_F}{2} + \frac{k_F^2-k^2}{4k}\ln\left|\frac{k+k_F}{k-k_F}\right|\right] \tag{4.8}$$

as derived in chapter 17 of reference [9]. It is interesting to note that the GW approximation to lowest order is simply the Hartree-Fock expression with the bare Coulomb potential replaced by a static screened potential.

The density correlation function can be expressed as a spectral representation

$$S(\mathbf{q},\omega) = -\frac{2}{\pi v(q)}\int_0^\infty d\omega' \frac{\omega'}{\omega^2-(\omega'-i\delta)^2}\mathrm{Im}\,(1/\epsilon(\mathbf{q},\omega'). \tag{4.9}$$

A simple model for this is to use a single oscillator for the dielectric function [31]

$$\epsilon(\mathbf{q},\omega) = 1 + \frac{\omega_p^2}{\omega_q^2-\omega_p^2-\omega^2-i\omega\delta}. \tag{4.10}$$

As $q\to 0$, the plasmon energy ω_q approaches the plasma frequency $\omega_p = \sqrt{4\pi n}$ for electron density n, and at high values of q, $\omega_q \to q^2$. In this derivation, we take

$$\omega_q^2 = \omega_p^2 + Aq^2 + q^4/4 \tag{4.11}$$

for the dispersion relation. To be general, we will not further specify the nature of the dispersion constant A. However, in all results presented we have followed B.I.

Lundqvist [31] and used $A = k_F^2/3$ except where explicitly stated otherwise. From equation 4.10, we have

$$\mathrm{Im}\,(\epsilon^{-1}(\mathbf{q},\omega)) = -\frac{\pi\omega_p^2}{2\omega_q}\delta(\omega-\omega_q). \tag{4.12}$$

We can add a finite broadening to our model by taking $\delta \to \gamma$ in our dielectric function. This will give us a density fluctuation propagator of

$$S(\mathbf{q},\omega) = -\frac{2}{\pi v(q)}\frac{\omega_q - i\gamma}{\omega^2-(\omega_q-i\gamma)^2}. \tag{4.13}$$

We wish to compute $\Sigma_d(\mathbf{k},\omega)$ self consistently with respect to $G(\mathbf{k},\omega) = [\omega - k^2/2 - \Sigma(\mathbf{k},\omega)]^{-1}$. Full self consistency is difficult, however. What we can easily do is replace $\Sigma(\mathbf{k},\omega)$ by a constant Σ_F. We then choose to enforce self consistency at the Fermi level, and set

$$\Sigma_F = \Sigma(k_F,\mu) \tag{4.14}$$

where $\mu = k_F^2/2 + \Sigma_F$ is the chemical potential. This is a convenient choice because quasiparticle excitations at the Fermi level turn out to be lossless, and Σ_F has no imaginary component. Then, taking

$$G(\mathbf{k},\omega) = G^{(0)}(k,\omega-\Sigma_F) = 1/[\omega - k^2/2 - \Sigma_F + i\delta_{\mathbf{k}}] \tag{4.15}$$

where $G^{(0)}$ is the bare electron propagator and $\delta_{\mathbf{k}}$ is a positive infinitesimal when $k > k_F$ and a negative infinitesimal otherwise, we find

$$\begin{aligned}\Sigma_d(\mathbf{k},\omega) &= \frac{i}{(2\pi)^4}\int d^3q d\omega' \frac{4\pi}{q^2\omega_q}\frac{\omega_p^2(\omega_q-i\gamma)}{(\omega'-\omega_q+i\gamma)(\omega'+\omega_q-i\gamma)}\times \\ &\quad\times\frac{1}{\omega-\omega'-(\mathbf{k}-\mathbf{q})^2/2-\Sigma_F+i\delta_{\mathbf{k}-\mathbf{q}}}.\end{aligned} \tag{4.16}$$

Since Σ_F is not given *a priori*, we define Σ_0 as the self energy obtained by setting $\Sigma_F = 0$. Then,

$$\Sigma(\mathbf{k},\omega) = \Sigma_0(\mathbf{k},\omega-\Sigma_F) \tag{4.17}$$

and we note that

$$\Sigma_F = \Sigma_0(k_F, k_F^2/2). \tag{4.18}$$

We also note in passing that our self energy is now in the form of a system of electrons coupled to a boson field

$$\Sigma(\mathbf{k},\omega) = i\int \frac{d^3q\, d\omega'}{(2\pi)^4}|V_0^q|^2 D(\mathbf{q},\omega')G(\mathbf{k}-\mathbf{q},\omega-\omega') \tag{4.19}$$

with a Bose propagator

$$D(\mathbf{q},\omega) = \frac{2\omega_q}{\omega^2-(\omega_q-i\delta)^2} \tag{4.20}$$

and the coupling of the electron to the boson given by

$$V_0^{\mathbf{q}} = \left(\frac{2\pi\omega_p^2}{q^2\omega_q}\right)^{1/2}. \tag{4.21}$$

This establishes the coupling to the density fluctuation potential that will be used in later sections.

After integrating equation 4.16 over a contour of ω' (closed in either half plane as convenient), we obtain

$$\begin{aligned}
\Sigma_d(k,\omega) &= \frac{\omega_p^2}{4\pi^2}\int \frac{dqd\phi d\xi}{\omega_q}\left[\frac{\theta(|\mathbf{k}-\mathbf{q}|-k_F)}{\omega-\omega_q-(\mathbf{k}-\mathbf{q})^2/2-\Sigma_F+i\gamma}\right. \\
&\quad \left. + \frac{\theta(k_F-|\mathbf{k}-\mathbf{q}|)}{\omega+\omega_q-(\mathbf{k}-\mathbf{q})^2/2-\Sigma_F-i\gamma}\right] \\
&= \frac{\omega_p^2}{4\pi^3}\int d\omega' \frac{\gamma}{(\omega-\omega')^2+\gamma^2} \\
&\quad \times \int \frac{dqd\phi d\xi}{\omega_q}\left[\frac{\theta(|\mathbf{k}-\mathbf{q}|-k_F)}{\omega'-\omega_q-(\mathbf{k}-\mathbf{q})^2/2-\Sigma_F+i\delta}\right. \\
&\quad \left. + \frac{\theta(k_F-|\mathbf{k}-\mathbf{q}|)}{\omega'+\omega_q-(\mathbf{k}-\mathbf{q})^2/2-\Sigma_F-i\delta}\right]
\end{aligned} \tag{4.22}$$

where $\xi = \cos\theta$. The last step simply introduces a Lorentzian broadening. Since this can be done after completing all the other integrations, we henceforth only consider infinitesimal broadening in the integral, with the understanding that it can be easily added later if desired.

For convenience, we split this into two terms

$$\Sigma_d(k,\omega) = \Sigma_d^+(k,\omega) + \Sigma_d^-(k,\omega) \tag{4.23}$$

$$\Sigma_d^+(k,\omega) = \frac{\omega_p^2}{2\pi}\int \frac{dqd\xi}{\omega_q}\frac{\theta(|\mathbf{k}-\mathbf{q}|-k_F)}{\omega-\omega_q-(\mathbf{k}-\mathbf{q})^2/2-\Sigma_F+i\delta} \tag{4.24}$$

$$\Sigma_d^-(k,\omega) = \frac{\omega_p^2}{2\pi}\int \frac{dqd\xi}{\omega_q}\frac{\theta(k_F-|\mathbf{k}-\mathbf{q}|)}{\omega+\omega_q-(\mathbf{k}-\mathbf{q})^2/2-\Sigma_F-i\delta} \tag{4.25}$$

for terms arising from contributions above and below the Fermi level, respectively.

4.1.1 Imaginary part

The imaginary part of the self energy is easily found to be

$$\begin{aligned}
\mathrm{Im}\,\Sigma_d^+(k,\omega) &= -\frac{\omega_p^2}{2}\int_0^\infty \frac{dq}{\omega_q}\int_{-1}^1 d\xi\theta(|\mathbf{k}-\mathbf{q}|-k_F)\times \\
&\quad \times\delta(\omega-\omega_q-k^2/2-q^2/2+kq\xi-\Sigma_F) \\
&= -\frac{\omega_p^2}{2k}\int_{q_1}^{q_2}\frac{dq}{\omega_q q} \\
&= -\frac{\omega_p}{4k}\ln\left[\frac{\omega_{q_1}+Aq_1^2/(2\omega_p)+\omega_p}{\omega_{q_2}+Aq_2^2/(2\omega_p)+\omega_p}\frac{q_2^2}{q_1^2}\right] \qquad (4.26) \\
\mathrm{Im}\,\Sigma_d^-(k,\omega) &= \frac{\omega_p^2}{2}\int_0^\infty \frac{dq}{\omega_q}\int_{-1}^1 d\xi\theta(k_F-|\mathbf{k}-\mathbf{q}|)\times \\
&\quad \times\,\delta(\omega+\omega_q-k^2/2-q^2/2+kq\xi-\Sigma_F) \\
&= \frac{\omega_p}{4k}\ln\left[\frac{\omega_{q_3}+Aq_3^2/(2\omega_p)+\omega_p}{\omega_{q_4}+Aq_4^2/(2\omega_p)+\omega_p}\frac{q_4^2}{q_3^2}\right] \qquad (4.27)
\end{aligned}$$

Here, q_1 and q_2 are the lower and upper limits, respectively, of the range of q values for which a ξ exists of magnitude less than unity satisfying the constraints of both the theta and delta function in the top line of the above equation. Similarly, q_3 is the lower and q_4 the upper bound of the range of q which allow the argument of the delta function to equal zero for ξ within the bounds of its integration, and the theta function is non-zero.

In order to evaluate this result, we need to find expressions for the fluctuation momenta q. The range of q allowed by the delta function in Eq. 4.26 is equivalent to finding values of q which satisfy the following inequalities:

$$\omega_q-\omega+\Sigma_F+(q-k)^2/2\le 0 \tag{4.28}$$

and

$$\omega_q - \omega + \Sigma_F + (q+k)^2/2 \geq 0$$

as can easily be checked by setting the argument of the delta function equal to zero and solving for ξ. The limiting q values will occur at solutions of

$$\omega_q - \omega + \Sigma_F = -(q-k)^2/2 \tag{4.29}$$

$$\omega_q - \omega + \Sigma_F = -(q+k)^2/2$$

Note that the right side of these equations are symmetric about $q = 0$, while the left sides are parabolas, one of which is the reflection of the other about $q = 0$. Thus, the solutions of one equation will be the negative of the solutions of the other. The two limiting q values are, in fact, the absolute values of the two solutions to either of the above equations.

A similar argument for the delta function constraint in Eq. 4.27 shows the limiting values of q occur at solutions of

$$\omega - \Sigma_F + \omega_q = (q-k)^2/2 \tag{4.30}$$

$$\omega - \Sigma_F + \omega_q = (q+k)^2/2$$

where similar symmetry properties ensure we need only solve one of the above equations and take the absolute value. To solve for these limiting values of q numerically, we evaluate

$$\omega_q = \omega - \Sigma_F - (q-k)^2/2, \tag{4.31}$$

square both sides, substitute equation 4.11 for ω_q, and collect terms in powers of q, resulting in a cubic polynomial for q.

$$\begin{aligned} kq^3 + (\omega - \Sigma_F + A - 3k^2/2)q^2 + (k^3 - 2(\omega - \Sigma_F)k)q & \qquad (4.32) \\ +(\omega - \Sigma_F)_p^2 - (\omega - \Sigma_F)^2 + (\omega - \Sigma_F)k^2 - k^4/4 &= 0. \end{aligned}$$

This introduces a spurious solution, corresponding to the solution of the equation

$$\omega_q = (q-k)^2/2 - \omega + \Sigma_F. \tag{4.33}$$

This is just the solution needed for equation 4.30. The three roots of the polynomial in q can be checked numerically by finding which root give the largest value of $|\omega_q - \omega + \Sigma_F + (q-k)^2/2|$. This corresponds to the lower q limit for Σ_d^-, since, as it will be shown, the Fermi cutoff only supplies an upper limit to this integral. Thus, this solution is equal to q_3. The two remaining roots give the q limits for Σ_d^+ before Fermi corrections, call them $\tilde{q}_1$ and $\tilde{q}_2$ such that $\tilde{q}_1 < \tilde{q}_2$. The solution q_3 always exists, $\tilde{q}_1$ and $\tilde{q}_2$ may or may not be real.

Now let us consider the Fermi occupation factor $\theta(|\mathbf{k}-\mathbf{q}| - k_F)$, which is non-zero when $k^2/2 + q^2/2 - kq\xi > \varepsilon_f$. Since the delta function in equation 4.26 requires $\omega - \omega_q - k^2/2 - q^2/2 - kq\xi - \Sigma_F = 0$, we can write

$$\omega_q < \omega - \Sigma_F - \varepsilon_f \tag{4.34}$$

Let q_0 be defined such that $\omega_{q_0} = \omega - \Sigma_F - \varepsilon_f$, and then

$$q_1 = \min(\tilde{q}_1, q_0) \tag{4.35}$$

$$q_2 = \min(\tilde{q}_2, q_0)$$

Similarly, the Fermi limit on Σ_d^-, $\theta(k_F - |\mathbf{k}-\mathbf{q}|)$, gives us the inequality

$$\omega_q < \varepsilon_f - \omega + \Sigma_F \tag{4.36}$$

This provides the upper limit to q, so q_4 is defined by $\omega_{q_4} = \varepsilon_f - \omega + \Sigma_F$.

4.1.2 Energy of the onset of plasmon losses

It is useful to find the value of ω which is at the onset of plasmon losses. Below this value of ω, $\mathrm{Im}\,\Sigma_d(k, E_k)$ is zero, above this value, $\mathrm{Im}\,\Sigma_d(k, E_k)$ rises rapidly before leveling off. At the plasmon turn-on, we must have either $\tilde{q}_1 = \tilde{q}_2 < q_0$ or $\tilde{q}_1 = q_0 < \tilde{q}_2$

when all threshold q values are evaluated on shell ($\omega = k^2/2 + \Sigma(k,\omega)$). The condition for $\tilde{q}_1 = \tilde{q}_2$ occurs when the discriminant of the cubic polynomial from equation 4.32 is zero. In order to solve this analytically, we approximate $\omega = k^2/2 + \Sigma_F$. This is reasonable since $\Sigma(k,\omega)$ at the plasmon turn on is close to Σ_F, and the errors should not be too great. With this approximation, we solve

$$k^6 - 3Ak^4 + (3A^2 - 27\omega_p^2/4)k^2 - A^3 = 0. \tag{4.37}$$

For $\tilde{q}_1 = q_0$, substituting eqn (for q_0) into eqn (for $\tilde{q}_1$ and $\tilde{q}_2 < q_0$) we find $k = |q_0 \pm k_F|$. With $q_0 = \sqrt{-2A + 2\sqrt{A^2 + E_k^2 - \omega_p^2}}$, we can solve for k. It turns out that k is given by the solution of the cubic equation

$$k^3 \pm (3k_F/2 + A/k_F)k^2 + (k_F^2 + 2A)k \pm (k_F^3/4 + Ak_F + \omega_p/k_F) = 0 \tag{4.38}$$

4.1.3 Real part

We now proceed to find the real part of the self energy. Starting from equation 4.24 we obtain

$$\Sigma_d^+(k,\omega) = \frac{\omega_p^2}{2\pi}\int \frac{dq}{\omega_q}\int_{-1}^{\xi^+} \frac{1}{\omega - \omega_q - k^2 - q^2 + kq\xi - \Sigma_F + i\delta} \tag{4.39}$$

where

$$\xi^+ = \max(\min(\frac{k^2 + q^2 - 2\varepsilon_F}{2kq}, 1), -1) \tag{4.40}$$

Note that $\xi^+ = 1$ when $q > k + k_F$ or $q < k - k_F$, and $\xi^+ = -1$ when $q < k_F - k$. We then have that

$$\begin{aligned}
\mathrm{Re}\,\Sigma_d^+(k,\omega) &= \frac{\omega_p^2}{2\pi}\int_0^\infty \frac{dq}{\omega_q kq}\ln\left|\frac{\omega - \omega_q - k^2/2 - q^2/2 + kq\xi^+ - \Sigma_F}{\omega - \omega_q - k^2/2 - q^2/2 - kq - \Sigma_F}\right| \qquad (4.41)\\
&= \frac{\omega_p^2}{2\pi k}\int_{k+k_F}^\infty \frac{dq}{\omega_q q}\ln\left|\frac{\omega - \omega_q - (k-q)^2/2 - \Sigma_F}{\omega - \omega_q - (k+q)^2/2 - \Sigma_F}\right|\\
&\quad + \frac{\omega_p^2}{2\pi k}\int_{k-k_F}^{k+k_F} \frac{dq}{\omega_q q}\ln\left|\frac{\omega - \omega_q - \varepsilon_F - \Sigma_F}{\omega - \omega_q - (k+q)^2/2 - \Sigma_F}\right|\\
&\quad + \theta(k - k_F)\frac{\omega_p^2}{2\pi k}\int_0^{k-k_F} \frac{dq}{\omega_q q}\ln\left|\frac{\omega - \omega_q - (k-q)^2/2 - \Sigma_F}{\omega - \omega_q - (k+q)^2/2 - \Sigma_F}\right|
\end{aligned}$$

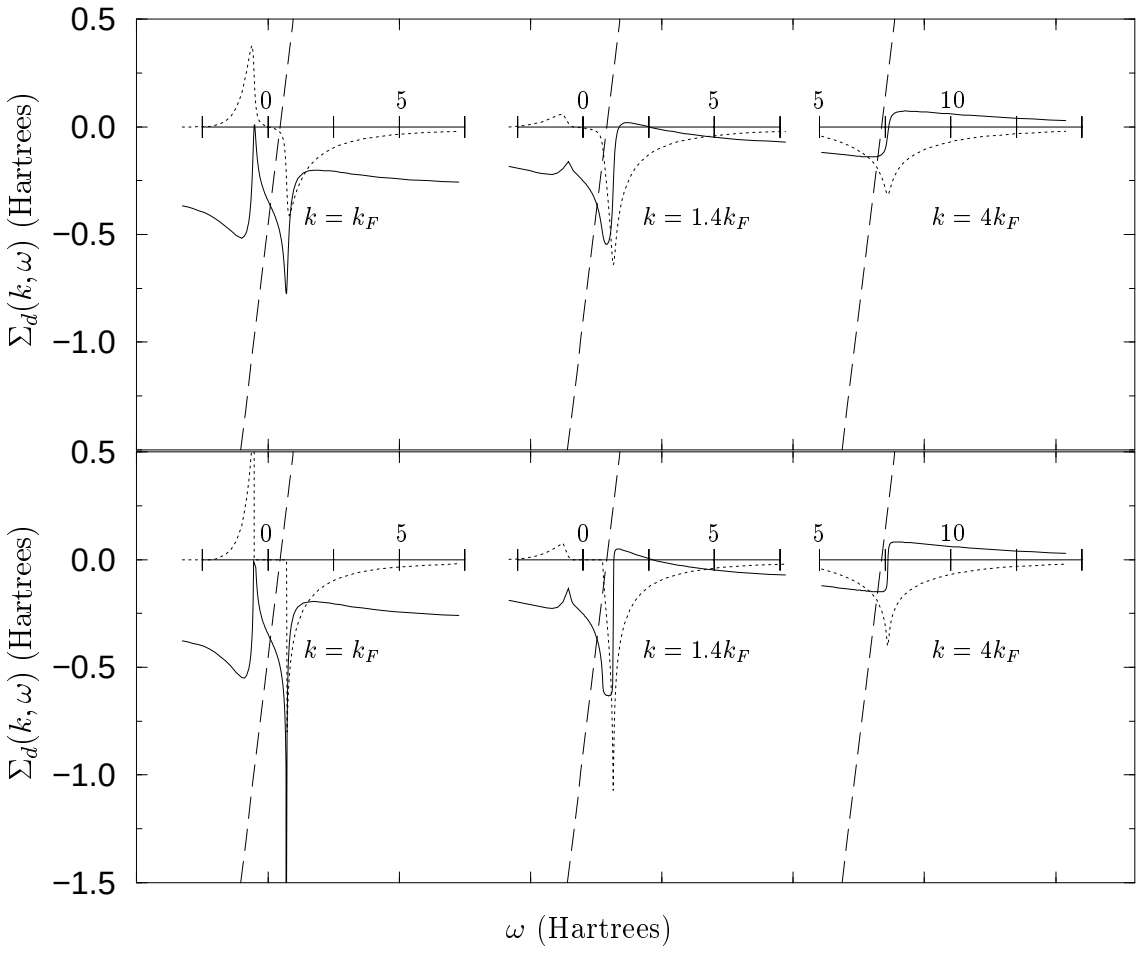

Figure 4.1: The real (solid) and imaginary (dots) parts of the self energy at selected values of momentum. The line $\omega = \omega - E_k$ is also shown (dashes). A quasiparticle occurs near where the $\omega = \omega - E_k$ line crosses the real part of the self energy. The upper figures have a plasmon broadening of $0.1\ \omega_p$, the lower figures are unbroadened. Both sets of figures are for $r_s = 2$.

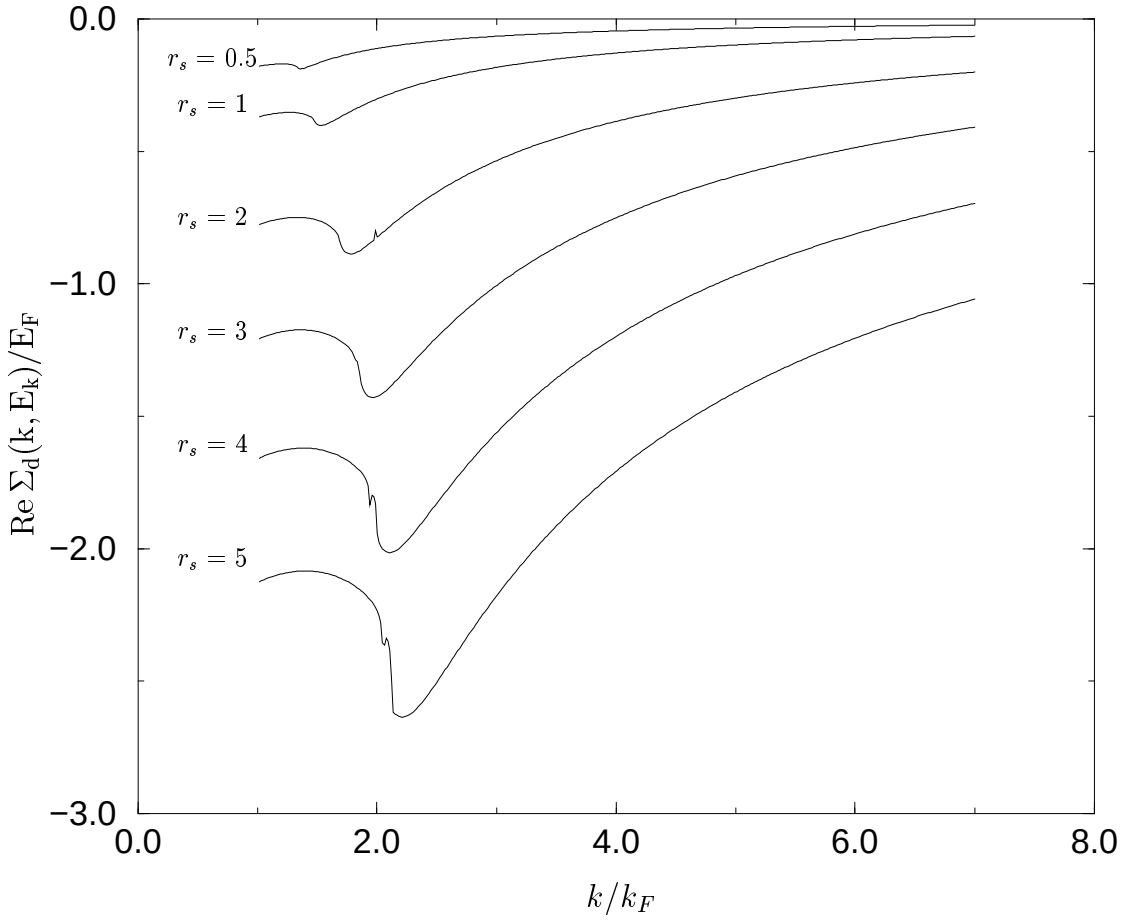

Figure 4.2: The real part of the quasiparticle self energy evaluated at several values of the electron gas density with zero plasmon broadening.

An analogous argument for Σ_d^- gives us

$$\begin{aligned} \mathrm{Re}\,\Sigma_d^-(k,\omega) &= \frac{\omega_p^2}{2\pi k}\int_{k-k_F}^{k+k_F}\frac{dq}{\omega_q q}\ln\left|\frac{\omega+\omega_q-(k-q)^2/2-\Sigma_F}{\omega+\omega_q-\varepsilon_F-\Sigma_F}\right| \\ &\quad+\theta(k_F-k)\frac{\omega_p^2}{2\pi k}\int_0^{k_F-k}\frac{dq}{\omega_q q}\ln\left|\frac{\omega+\omega_q-(k-q)^2/2-\Sigma_F}{\omega+\omega_q-(k+q)^2/2-\Sigma_F}\right| \end{aligned} \tag{4.42}$$

The full self energy in this plasmon pole model is thus given by

$$\Sigma(k,\omega) = \mathrm{Re}\,\Sigma_d^+(k,\omega) + \mathrm{Re}\,\Sigma_d^-(k,\omega) + i\,\mathrm{Im}\,\Sigma_d^+(k,\omega) + i\,\mathrm{Im}\,\Sigma_d^-(k,\omega) + \Sigma_{ex}(k)$$

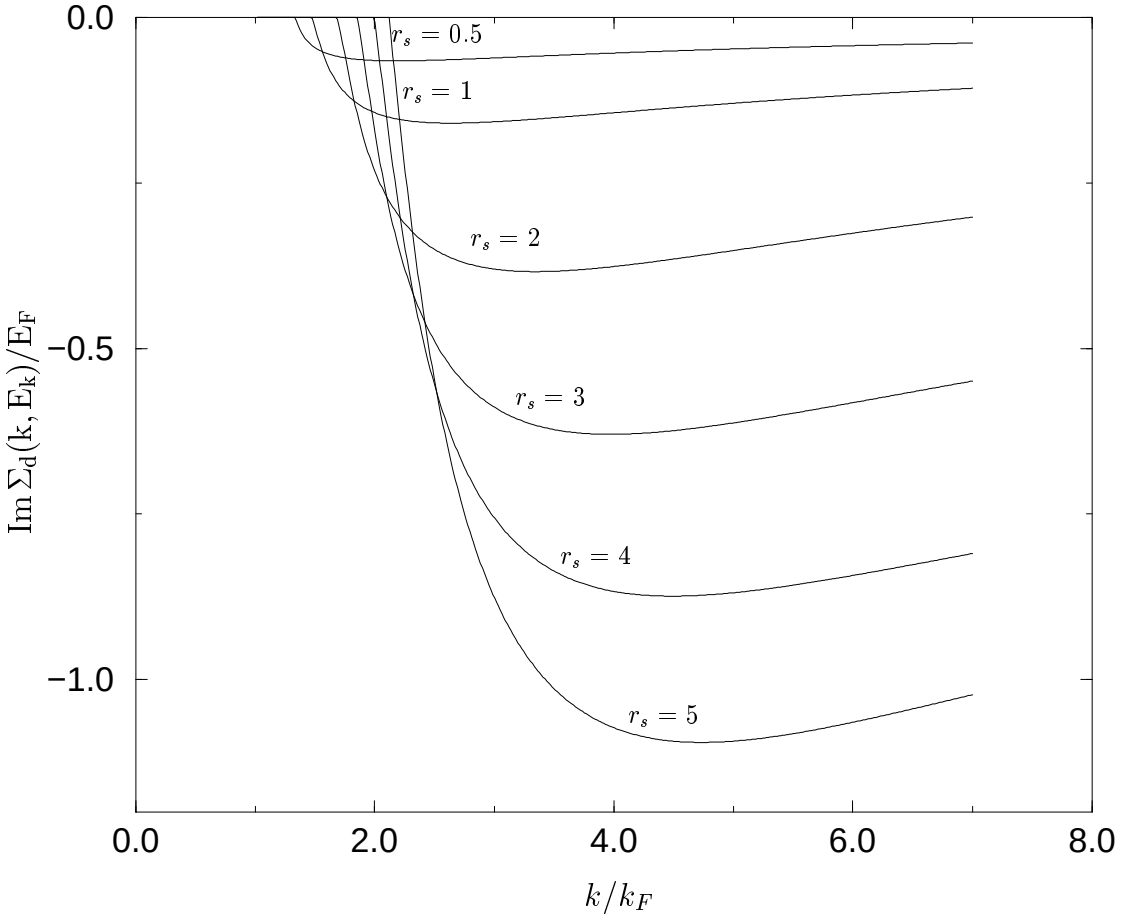

Figure 4.3: The imaginary part of the quasiparticle self energy evaluated at several values of the electron gas density with zero plasmon broadening.

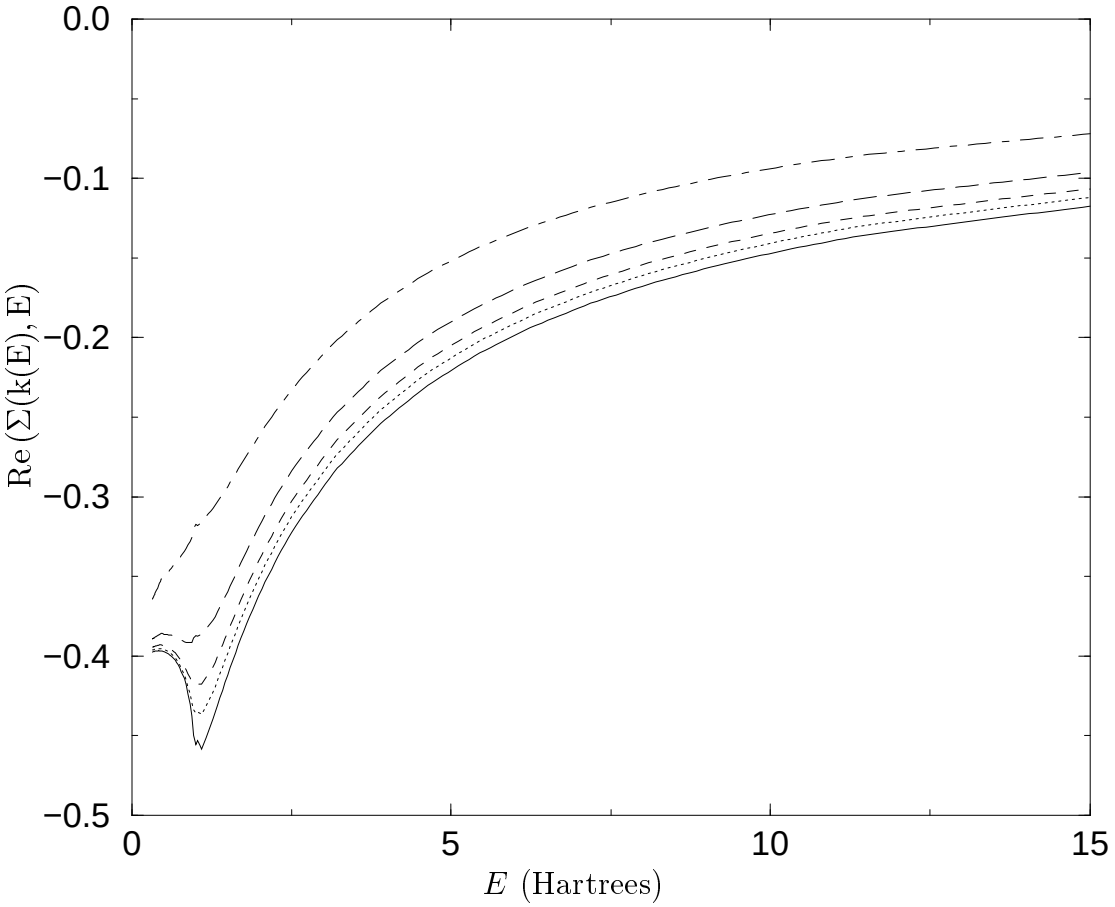

Figure 4.4: The real part of the quasiparticle self energy evaluated at the interstitial electron gas density of copper ($r_s = 1.8$) with a plasmon broadening of $0\omega_p$ (solid), $0.05\omega_p$ (dots), $0.1\omega_p$ (short dashes), $0.2\omega_p$ (long dashes), and $0.5\omega_p$ (dot-dashes).

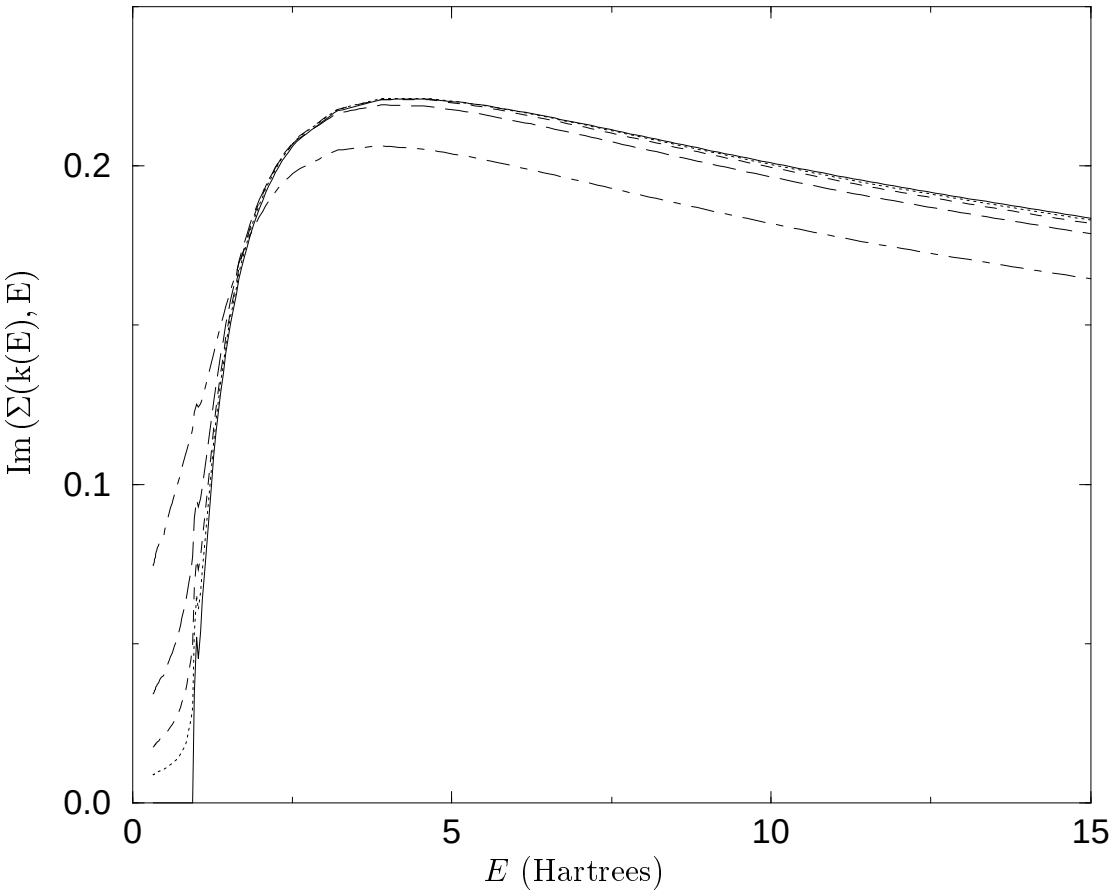

Figure 4.5: The imaginary part of the quasiparticle self energy evaluated at the interstitial electron gas density of copper ($r_s = 1.8$) with a plasmon broadening of $0\omega_p$ (solid), $0.05\omega_p$ (dots), $0.1\omega_p$ (short dashes), $0.2\omega_p$ (long dashes), and $0.5\omega_p$ (dot-dashes).

Although the details of the derivation differ, the final results are mathematically equivalent to those presented in Lundqvist [31] for zero plasmon broadening. This is expected since the starting point and all approximations are the same. Figure 4.10, for example, reproduces figure 6 from Lundqvist's paper.

4.2 The GW renormalization constant in the plasmon pole, free electron gas approximation

For a system described by a propagator $G(\mathbf{k},\omega) = [\omega - k^2/2 - \Sigma(\mathbf{k},\omega) - i\delta]^{-1}$ a quasiparticle will occur when

$$\omega = E_p = k^2/2 + \Sigma(\mathbf{k}, E_p) \tag{4.43}$$

where E_p is, in general, complex. The prescription we have used so far of approximating $\Sigma(\mathbf{k}, E_p)$ by the constant Σ_F is unsatisfactory in this case. Instead, we expand the self energy in a Taylor series. Then

$$\begin{aligned}
\omega - k^2/2 - \Sigma(\mathbf{k},\omega) &= \omega - k^2/2 - \sum_{n=0}^{\infty}\left[\frac{(\omega - k^2/2 - \Sigma_F)^n}{n!}\times\right. \\
&\quad \left.\times \frac{\partial^n}{\partial\omega^n}\Sigma_0(\mathbf{k}, k^2/2)\right] \\
&= \omega - k^2/2 - \Sigma(\mathbf{k}, E_p)) \\
&\quad + \sum_{n=1}^{\infty}\left[\frac{(E_p - k^2/2 - \Sigma_F)^n - (\omega - k^2/2 - \Sigma_F)^n}{n!}\times\right. \\
&\quad \left.\times \frac{\partial^n}{\partial\omega^n}\Sigma_0(\mathbf{k}, k^2/2)\right] \\
&= (\omega - E_p)\left(1 - \sum_{n=1}^{\infty}\left[\frac{(E_p - k^2/2 - \Sigma_F)^{n-1}}{(n-1)!}\times\right.\right. \\
&\quad \left.\left.\times\frac{\partial^n}{\partial\omega^n}\Sigma_0(\mathbf{k}, k^2/2) + \mathcal{O}(\omega - E_p)\right]\right) \\
&= (\omega - E_p)\left(1 - \frac{\partial}{\partial\omega}\Sigma(\mathbf{k}, E_p)\right) + \mathcal{O}(\omega - E_p)^2.
\end{aligned} \tag{4.44}$$

If we set $\omega = k^2/2 - \Sigma_F$, we immediately find

$$\Sigma_0(\mathbf{k}, k^2/2) - \Sigma_F = (E_p - \Sigma_F - k^2/2)\left(1 - \frac{\partial}{\partial\omega}\Sigma(\mathbf{k}, E_p)\right) \tag{4.45}$$

$$= \quad (\Sigma(\mathbf{k}, E_p) - \Sigma_F)\left(1 - \frac{\partial}{\partial\omega}\Sigma(\mathbf{k}, E_p)\right)$$

from which it follows that

$$E_p = k^2/2 + \Sigma_F + Z_k[\Sigma_0(\mathbf{k}, k^2/2) - \Sigma_F] \tag{4.46}$$

where $Z_\mathbf{k} = 1/(1 - \partial/\partial\omega\Sigma(\mathbf{k}, E_p))$ is the *renormalization constant*. It is easy to show that the renormalization constant is the residue at the quasiparticle pole:

$$\begin{aligned} \text{residue} &= \lim_{\omega\to E_p} \frac{\omega - E_p}{\omega - k^2/2 - \Sigma(\mathbf{k}, \omega)} \\ &= \lim_{\omega\to E_p} \frac{\omega - E_p}{(\omega - E_p)\left(1 - \frac{\partial}{\partial\omega}\Sigma(\mathbf{k}, E_p)\right) + \mathcal{O}(\omega - E_p)^2} \\ &= Z_\mathbf{k} \end{aligned} \tag{4.47}$$

Rather than evaluating these equations self consistently for a complex E_p, we can in practice get very good results for the quasiparticle energy by taking only the first two terms in the Taylor series in equation 4.44, which amounts to approximating $Z_\mathbf{k} \approx Z^0_\mathbf{k} = 1/(1 - \partial/\partial\omega\Sigma_0(\mathbf{k}, k^2/2))$. This method will yield values for the photoelectron energy typically within 1% to 0.1% of the self consistent value $E_\mathbf{k} = k^2/2 + \mathrm{Re}\,\Sigma(\mathbf{k}, E_\mathbf{k})$. Unfortunately, this is only approximately the real part of the quasiparticle pole, and this approximation does not always do a satisfactory job of finding the weight of the quasiparticle pole, and thus yields a somewhat incorrect lineshape of the quasiparticle. This would not be so serious, except that if we wish to find the structure of the extrinsic satellite by removing the quasiparticle lineshape from the complete GW spectral function, an incorrect subtraction will leave considerable residual structure in the vicinity of the quasiparticle. We could approximate $\partial/\partial\omega\Sigma(\mathbf{k}, E_p) = \partial/\partial\omega\Sigma_0(\mathbf{k}, k^2/2) + (E_p - k^2/2 - \Sigma_F)\partial^2/\partial\omega^2\Sigma_0(\mathbf{k}, k^2/2)$. However, finding the second derivative of the self energy is fairly involved. Fortunately, there is an easier way, which yields excellent results (figure 4.6). Define the real energy $E^1_\mathbf{k}$ as

$$E^1_\mathbf{k} \quad = \quad k^2/2 + \mathrm{Re}\,\Sigma(\mathbf{k}, E^1_\mathbf{k}) \tag{4.48}$$

$$\approx \quad k^2/2 + \Sigma_F + \mathrm{Re}\, Z^0_{\mathbf{k}}(\mathrm{Re}\, \Sigma_0(\mathbf{k}, k^2/2) - \Sigma_F)$$

and Taylor expand $\Sigma(\mathbf{k}, \omega)$ about $E^1_{\mathbf{k}}$.

$$\begin{aligned} G(\mathbf{k}, \omega) &= \frac{1}{\omega - k^2/2 - \Sigma(\mathbf{k}, \omega)} \\ &= \frac{1}{\omega - k^2/2 - \Sigma(\mathbf{k}, E^1_{\mathbf{k}}) - (\omega - E^1_{\mathbf{k}})\frac{\partial}{\partial \omega}\Sigma(\mathbf{k}, E^1_{\mathbf{k}})} \\ &= \frac{1}{(\omega - E^1_{\mathbf{k}})(1 - \frac{\partial}{\partial \omega}\Sigma(\mathbf{k}, E^1_{\mathbf{k}})) + i\Gamma^1_{\mathbf{k}}} \end{aligned} \tag{4.49}$$

where we define $\Gamma^1_{\mathbf{k}} = |\mathrm{Im}\, \Sigma(\mathbf{k}, E^1_{\mathbf{k}})|$. If we let $Z^1_{\mathbf{k}} = 1/\left(1 - \frac{\partial}{\partial \omega}\Sigma(\mathbf{k}, E^1_{\mathbf{k}})\right)$, then we have

$$G_{qp}(\mathbf{k}, \omega) = \frac{Z^1_{\mathbf{k}}}{(\omega - E^1_{\mathbf{k}}) + i\Gamma^1_{\mathbf{k}} Z^1_{\mathbf{k}}}. \tag{4.50}$$

From this, it follows that the quasiparticle pole is located at

$$E_p = E^1_{\mathbf{k}} - i\Gamma^1_{\mathbf{k}} Z^1_{\mathbf{k}}. \tag{4.51}$$

4.2.1 Quasiparticle Lineshape

The quasiparticle lineshape is given by

$$\begin{aligned} A_{qp}(\mathbf{k}, \omega) &= -\frac{1}{\pi}\mathrm{Im}\, G_{qp}(\mathbf{k}, \omega) \\ &= \frac{1}{\pi}\frac{\Gamma^1_{\mathbf{k}} Z^R_{\mathbf{k}} - (\omega - E^1_{\mathbf{k}} - \Gamma^1_{\mathbf{k}} Z^I_{\mathbf{k}}) Z^I_{\mathbf{k}}}{(\omega - E^1_{\mathbf{k}} - \Gamma^1_{\mathbf{k}} Z^I_{\mathbf{k}})^2 + (\Gamma^1_{\mathbf{k}} Z^R_{\mathbf{k}})^2} \end{aligned} \tag{4.52}$$

where $Z^R_{\mathbf{k}} = \mathrm{Re}\, Z^1_{\mathbf{k}}$ and $Z^I_{\mathbf{k}} = \mathrm{Im}\, Z^1_{\mathbf{k}}$. This shows that the quasiparticle occurs at an energy $E_{\mathbf{k}} = E^1_{\mathbf{k}} + \Gamma^1_{\mathbf{k}} Z^I_{\mathbf{k}}$, has a width $\Gamma_{\mathbf{k}} = \Gamma^1_{\mathbf{k}} Z^R_{\mathbf{k}}$, and has a total spectral weight of $Z^R_{\mathbf{k}}$. In this approximation, $Z_{\mathbf{k}} = Z^1_{\mathbf{k}}$.

One often finds the quasiparticle represented by a first order approximation:

$$A^{\mathrm{approx}}_{qp}(\mathbf{k}, \omega) = -\frac{1}{\pi}\mathrm{Im}\, \frac{Z^0_{\mathbf{k}}}{\omega - E^1_{\mathbf{k}} + i\Gamma^1_{\mathbf{k}}}. \tag{4.53}$$

We see now that, while this form will approximate the shape of the quasiparticle, it will get the quasiparticle peak at too high of energy and will overestimate the

quasiparticle width when the quasiparticle pole is not located on the real axis. A comparison of this simplified quasiparticle to the higher order approximation given in equation 4.52 and to the full spectral function is given in figure 4.6.

Before the onset of plasmon losses, $\mathrm{Im}\,\Sigma(\mathbf{k}, k^2/2)$ varies only slowly and $Z_{\mathbf{k}}$ is thus almost real (in the plasmon pole approximation, $\mathrm{Im}\,\Sigma(\mathbf{k}, k^2/2) = 0$ in this regime and $\mathrm{Im}\,Z_{\mathbf{k}} = 0$ exactly). In this region, the quasiparticle thus has a narrow Lorentzian lineshape. When significant broadening is present, however, $Z_{\mathbf{k}}$ is complex and the quasiparticle takes on the given Fano lineshape. A large imaginary part of $Z_{\mathbf{k}}$ will, in particular, lead to regions far from the quasiparticle energy that have negative spectral density due to the Fano asymmetry. Since the quasiparticle is not well defined except close to the quasiparticle energy, we find it useful to introduce a Gaussian cutoff to the imaginary part of $Z_{\mathbf{k}}$, i.e.,

$$A_{qp}^{\mathrm{gauss}}(\mathbf{k},\omega) = \frac{1}{\pi}\frac{\Gamma_{\mathbf{k}}\mathrm{Re}\,Z_{\mathbf{k}} - (\omega - E_{\mathbf{k}})\mathrm{Im}\,Z_{\mathbf{k}} e^{-((\omega-E_{\mathbf{k}})/2\omega_p)^2}}{(\omega - E_{\mathbf{k}})^2 + (\Gamma_{\mathbf{k}})^2} \tag{4.54}$$

This preserves the quasiparticle energy, width, and weight while strongly reducing the long range (and, on one side, negative) tails.

4.2.2 Derivatives of the real self energy

Starting from equations 4.41 and 4.42 it is easy to directly find the derivatives of the real part of the self energy with respect to ω.

$$\begin{aligned}
\mathrm{Re}\,\frac{\partial}{\partial\omega}\Sigma^{+}_{d,0}(k,\omega) \;=\; & \frac{\omega_p^2}{2\pi k}\int_{k+k_F}^{\infty}\frac{dq}{\omega_q q}\left[\frac{1}{\omega - \omega_q - (k-q)^2/2}\right. \\
& \left. - \frac{1}{\omega - \omega_q - (k+q)^2/2}\right] \\
& + \frac{\omega_p^2}{2\pi k}\int_{k-k_F}^{k+k_F}\frac{dq}{\omega_q q}\left[\frac{1}{\omega - \omega_q - \varepsilon_F}\right. \\
& \left. - \frac{1}{\omega - \omega_q - (k+q)^2/2}\right] \\
& + \theta(k-k_F)\frac{\omega_p^2}{2\pi k}\int_{0}^{k-k_F}\frac{dq}{\omega_q q}\left[\frac{1}{\omega - \omega_q - (k-q)^2/2}\right.
\end{aligned} \tag{4.55}$$

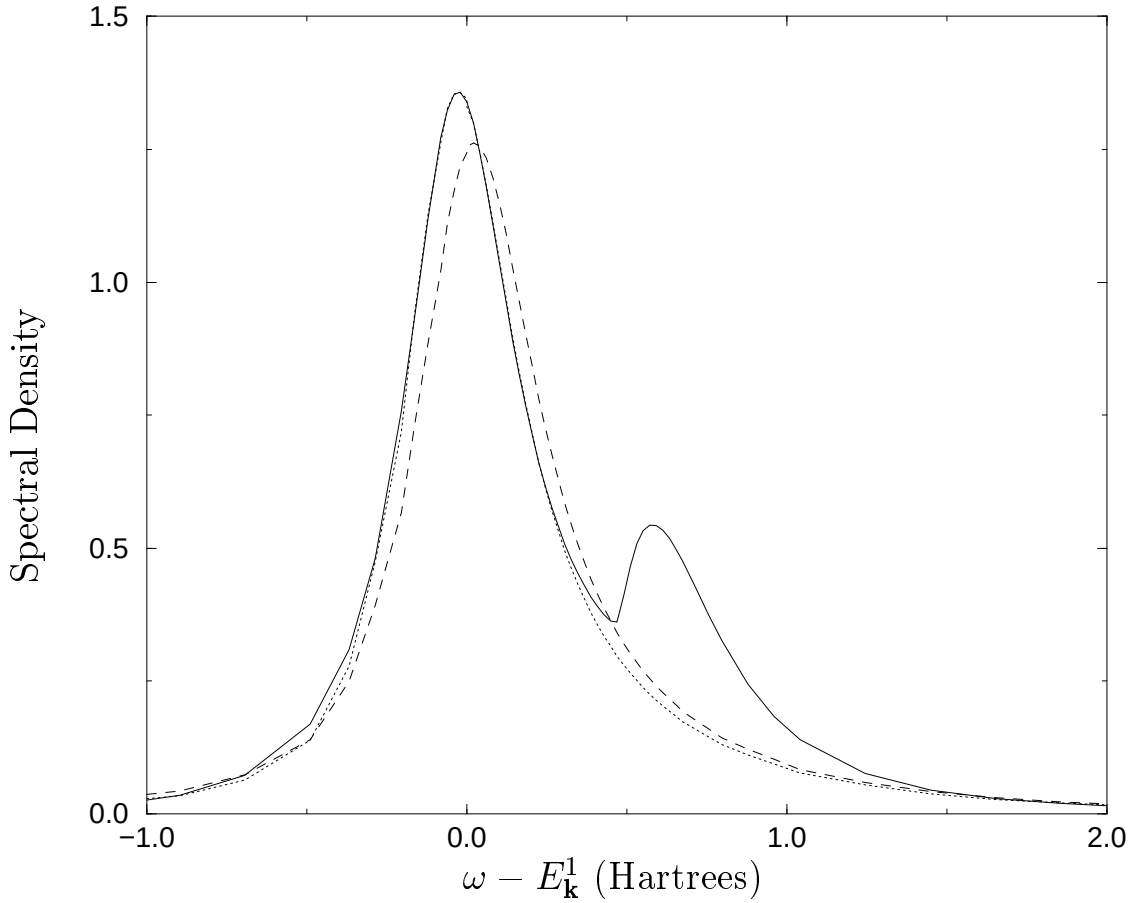

Figure 4.6: The quasiparticle spectral function A_{qp}^{gauss} (dots) compared to the full spectral function (solid line) and the simplified approximation replacing $Z^1_{\mathbf{k}}$ with $Z^0_{\mathbf{k}}$, $E_{\mathbf{k}}$ with $E^1_{\mathbf{k}}$, and $\Gamma_{\mathbf{k}}$ with $\Gamma^1_{\mathbf{k}}$ (dashes). All curves are for $r_s = 2$

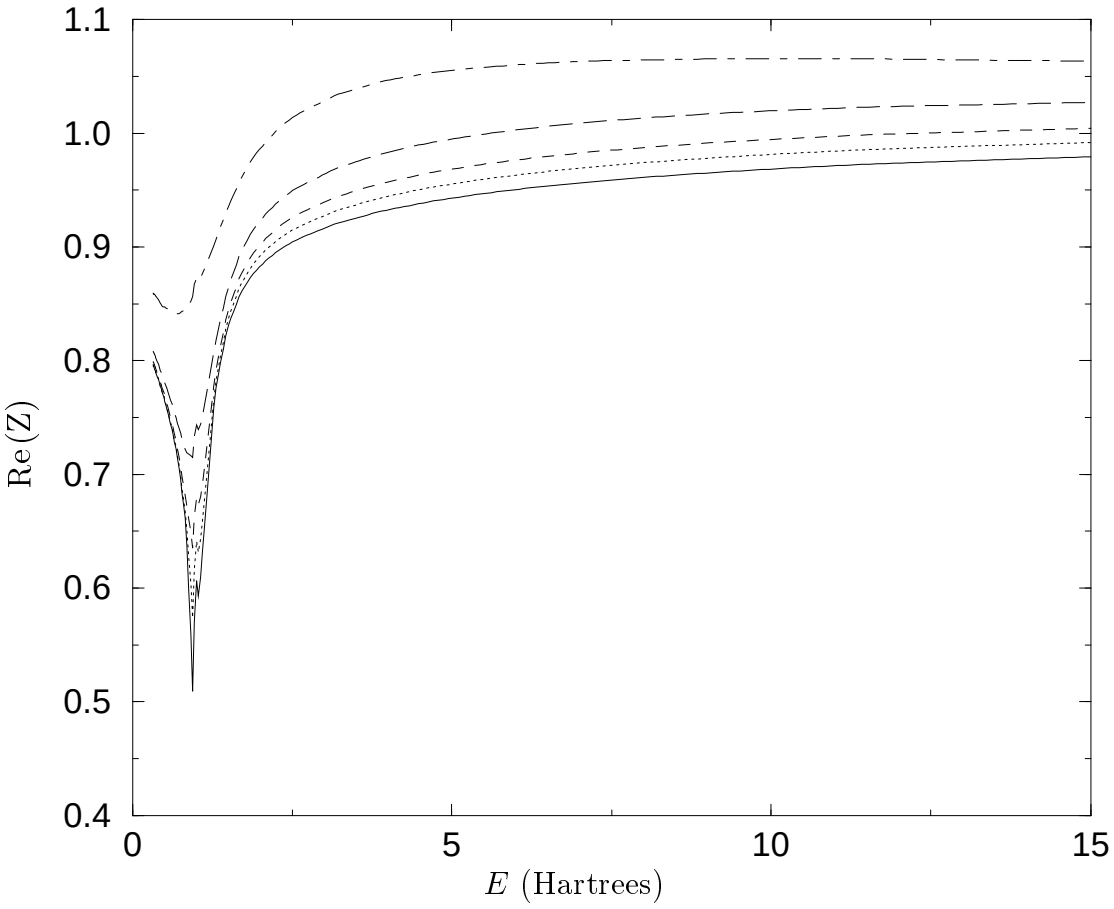

Figure 4.7: The real part of the renormalization constant $Z(k(E))$ for the interstitial electron gas density of copper ($r_s = 1.8$) at plasmon broadenings of $0\omega_p$ (solid), $0.05\omega_p$ (dots), $0.1\omega_p$ (short dashes), $0.2\omega_p$ (long dashes), and $0.5\omega_p$ (dot-dashes). Note that at large amounts of broadening, the real part of the renormalization constant exceeds one. This is a consequence of extending the quasiparticle approximation, normally applicable only in the vicinity of the quasiparticle pole, to all values of the excitation energy. Physically, the spectral weight under the peak in the spectral function due to the quasiparticle pole is less than one.

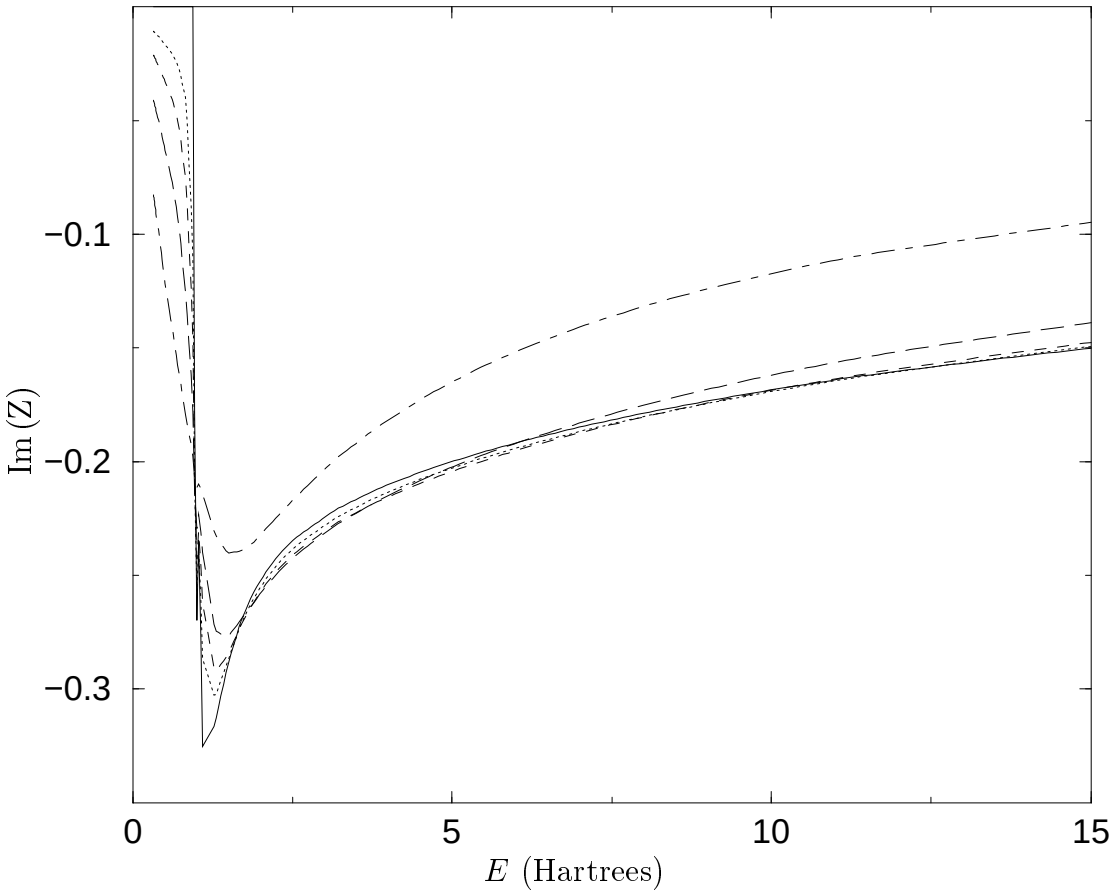

Figure 4.8: The imaginary part of the renormalization constant $Z(k(E))$ for the interstitial electron gas density of copper ($r_s = 1.8$) at plasmon broadenings of $0\omega_p$ (solid), $0.05\omega_p$ (dots), $0.1\omega_p$ (short dashes), $0.2\omega_p$ (long dashes), and $0.5\omega_p$ (dot-dashes).

$$
\begin{aligned}
& - \frac{1}{\omega - \omega_q - (k+q)^2/2} \Bigg] \\
\mathrm{Re}\,\frac{\partial}{\partial\omega}\Sigma^{-}_{d,0}(k,\omega) &= \frac{\omega_p^2}{2\pi k}\int_{k-k_F}^{k+k_F}\frac{dq}{\omega_q q}\left[\frac{1}{\omega+\omega_q-(k+q)^2/2} - \frac{1}{\omega+\omega_q-\varepsilon_F}\right] \\
& + \theta(k-k_F)\frac{\omega_p^2}{2\pi k}\int_{0}^{k-k_F}\frac{dq}{\omega_q q}\left[\frac{1}{\omega+\omega_q-(k-q)^2/2}\right. \\
& \left. - \frac{1}{\omega+\omega_q-(k+q)^2/2}\right]
\end{aligned}
$$

4.2.3 Derivatives of the imaginary self energy

To find the imaginary part of the derivative of the self energy, note that equations 4.26 and 4.27 are sums of terms of the form

$$\frac{\omega_p}{4k}\left[2\ln(q) - \ln(\omega_p + \omega_q + Aq^2/(2\omega_p))\right]. \tag{4.56}$$

The derivative is thus sums of terms of the form

$$\frac{\omega_p}{4k}\frac{\partial q}{\partial\omega}\left[\frac{2}{q} - \frac{1}{\omega_p+\omega_q+Aq^2/(2\omega_p)}\left(Aq\left(\frac{1}{\omega_q}+\frac{1}{\omega_p}\right)+\frac{q^3}{2\omega_q}\right)\right]. \tag{4.57}$$

To evaluate $\partial q/\partial\omega$ we note that $\tilde{q}_1$ and $\tilde{q}_2$ both satisfy $\omega = \omega_q + (q \pm k)^2/2$. From this, we find that for $q = \tilde{q}_1$ or $q = \tilde{q}_2$

$$\frac{\partial q}{\partial\omega} = \frac{\omega_q}{(q\pm k)\omega_q + Aq + q^3/2} \tag{4.58}$$

where we use $(q+k)$ if $\omega = \omega_q + (q+k)^2/2$, and $(q-k)$ if $\omega = \omega_q + (q-k)^2/2$. Similarly, for $q = q_3$,

$$\frac{\partial q}{\partial\omega} = \frac{\omega_q}{(q\pm k)\omega_q - Aq - q^3/2}. \tag{4.59}$$

Finally, from the relations $\omega_{q_0} = \omega - \varepsilon_F$ and $\omega_{q_4} = \varepsilon_F - \omega$, we find that for $q = q_0$ or $q = q_4$

$$\frac{\partial q_0}{\partial\omega} = \begin{cases} (\omega-\varepsilon_F)/\left(q_0\sqrt{A^2+(\omega-\varepsilon_F)^2-\omega_p^2}\right) & \text{for } \omega-\varepsilon_F > \omega_p \\ 0 & \text{otherwise} \end{cases} \tag{4.60}$$

$$\frac{\partial q_4}{\partial\omega} = \begin{cases} (\omega-\varepsilon_F)/\left(q_4\sqrt{A^2+(\omega-\varepsilon_F)^2-\omega_p^2}\right) & \text{for } \varepsilon_F-\omega > \omega_p \\ 0 & \text{otherwise} \end{cases} \tag{4.61}$$

Thus, the full derivative of the imaginary part of the self energy is

$$\begin{aligned}
\mathrm{Im}\,\frac{\partial}{\partial\omega}\Sigma^{+}_{d,0}(k,\omega) &= \frac{\omega_p}{4k}\frac{\partial q_1}{\partial\omega}\left[\frac{2}{q_1} - \frac{1}{\omega_p+\omega_{q_1}+Aq_1^2/(2\omega_p)}\times\right. \\
&\quad \left.\times\left(Aq_1\left(\frac{1}{\omega_{q_1}}+\frac{1}{\omega_p}\right)+\frac{q_1^3}{2\omega_{q_1}}\right)\right] \\
&\quad -\frac{\omega_p}{4k}\frac{\partial q_2}{\partial\omega}\left[\frac{2}{q_2} - \frac{1}{\omega_p+\omega_{q_2}+Aq_2^2/(2\omega_p)}\times\right. \\
&\quad \left.\times\left(Aq_2\left(\frac{1}{\omega_{q_2}}+\frac{1}{\omega_p}\right)+\frac{q_2^3}{2\omega_{q_2}}\right)\right] \qquad (4.62) \\
\mathrm{Im}\,\frac{\partial}{\partial\omega}\Sigma^{-}_{d,0}(k,\omega) &= \frac{\omega_p}{4k}\frac{\partial q_4}{\partial\omega}\left[\frac{2}{q_4} - \frac{1}{\omega_p+\omega_{q_4}+Aq_4^2/(2\omega_p)}\times\right. \\
&\quad \left.\times\left(Aq_4\left(\frac{1}{\omega_{q_4}}+\frac{1}{\omega_p}\right)+\frac{q_4^3}{2\omega_{q_4}}\right)\right] \\
&\quad -\frac{\omega_p}{4k}\frac{\partial q_3}{\partial\omega}\left[\frac{2}{q_3} - \frac{1}{\omega_p+\omega_{q_3}+Aq_3^2/(2\omega_p)}\times\right. \\
&\quad \left.\times\left(Aq_3\left(\frac{1}{\omega_{q_3}}+\frac{1}{\omega_p}\right)+\frac{q_3^3}{2\omega_{q_3}}\right)\right] \qquad (4.63)
\end{aligned}$$

Noting that $(\partial/\partial\omega)V_{ex} = 0$, we can thus find the full derivative of the self energy, and from there compute Z_k and all quasiparticle properties.

4.2.4 The renormalization constant with a broadened plasmon

The analytical expressions for the derivative of the self energy are useful when the self energy is calculated without plasmon broadening, as the self energy then exhibits several singular structures which can inhibit numerical evaluation of the derivative. Since the introduction of plasmon broadening is brought about by a Lorentzian convolution, the unbroadened structure must first be calculated, and when computing that structure, the derivative is necessary for finding the on-shell quasiparticle energies. Once the plasmon broadening is introduced, however, the shape of the self energy is no longer singular, and a numerical evaluation of the derivative will suffice.

However, as shown in figure 4.7, there are subtle numerical problems with the calculation of the quasiparticle. In particular, the real part of the renormalization

constant can become greater than one when significant plasmon broadening is introduced. This may be due in part to calculating the derivatives on the real axis rather than at the quasiparticle pole, however, a comparison of the quasiparticle lineshape to the full spectral function indicates that the quasiparticle approximation does an excellent job of reproducing the spectral function in the immediate vicinity of the quasiparticle, but the long range tails of the quasiparticle add more spectral weight than can physically exist (figure 4.9). This indicates that the high values of the renormalization constant are intrinsic to this model. As a consequence, it is recommended that when performing calculations that depend upon the quasiparticle properties, the plasmon broadening be kept to a minimum. It is found that for typical metalic electron densities with a Wigner-Seitz radius of around $r_s = 2$, a plasmon broadening of $0.1\omega_p$ gives acceptable results for the XAS convolutions performed in this dissertation.

4.3 The structure of the extrinsic satellite

As described in the introductory remarks to this chapter, a system described by a Green's function $G(k,\omega)$ has a spectral function, or excitation spectrum represented as a probability density, equal to

$$\begin{aligned} A(k,\omega) &= \frac{1}{\pi}|\mathrm{Im}\, G(k,\omega)| \\ &= \frac{1}{\pi}\frac{|\mathrm{Im}\, \Sigma(k,\omega)|}{(\omega - k^2/2 - \mathrm{Re}\, \Sigma(k,\omega)^2 + (\mathrm{Im}\, \Sigma(k,\omega))^2}. \end{aligned} \tag{4.64}$$

When we plot $A(k,\omega)$ against ω, we find that in addition to the strong feature in the vicinity of the quasiparticle, as described in the previous section, there are additional *satellite* peaks. We can then define the extrinsic satellite spectral function as the full extrinsic spectral function with the quasiparticle lineshape subtracted off.

$$A_{extr} = \frac{1}{\pi}\frac{|\mathrm{Im}\, \Sigma(k,\omega)|}{(\omega - k^2/2 - \mathrm{Re}\, \Sigma(k,\omega)^2 + (\mathrm{Im}\, \Sigma(k,\omega))^2} - A_{qp} \tag{4.65}$$

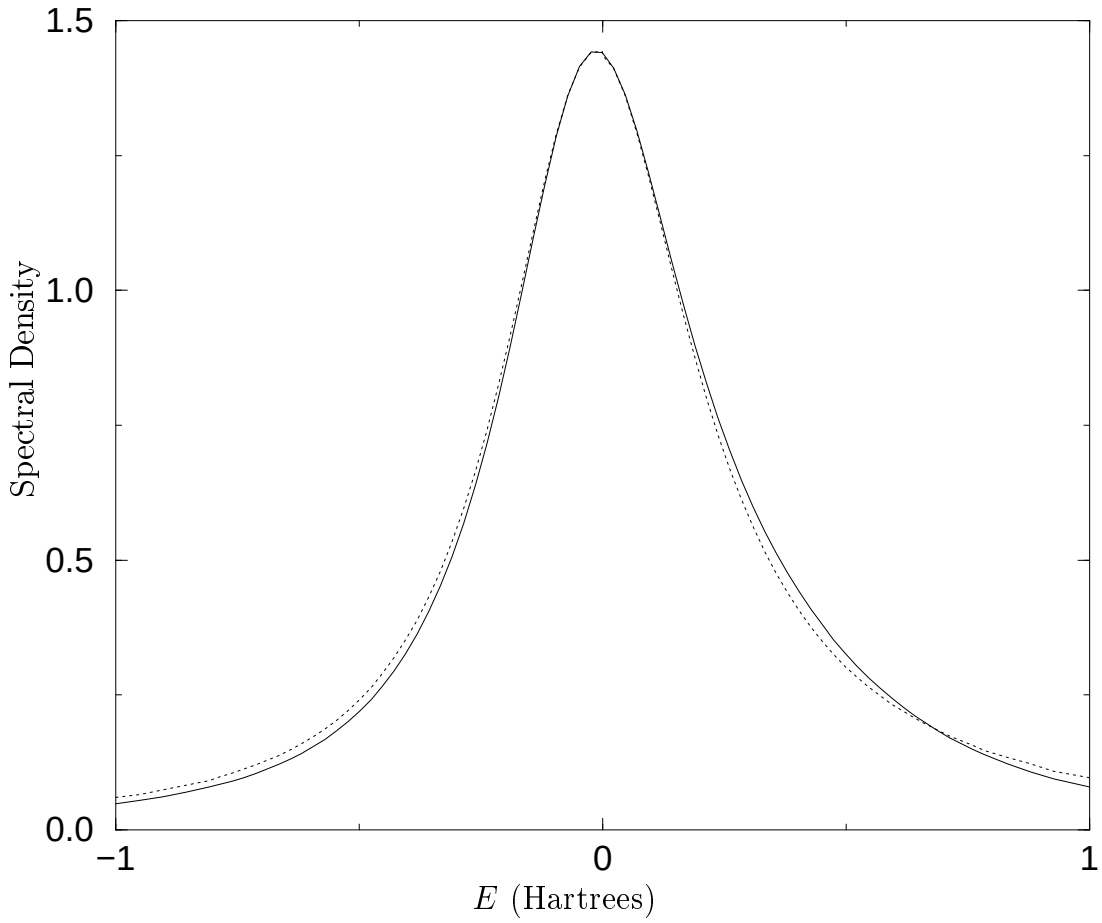

Figure 4.9: The full spectral function (solid) compared to the quasiparticle approximation (dots) for the interstitial electron density of copper ($r_s = 1.8$) and a plasmon broadening of $0.5\omega_p$. While the quasiparticle approximation seems to reproduce the behavior near the quasiparticle pole, the long range tails of the quasiparticle lineshape significantly exceed the spectral density of the full spectral function away from the pole. As a consequence, the quasiparticle has a weight greater than one.

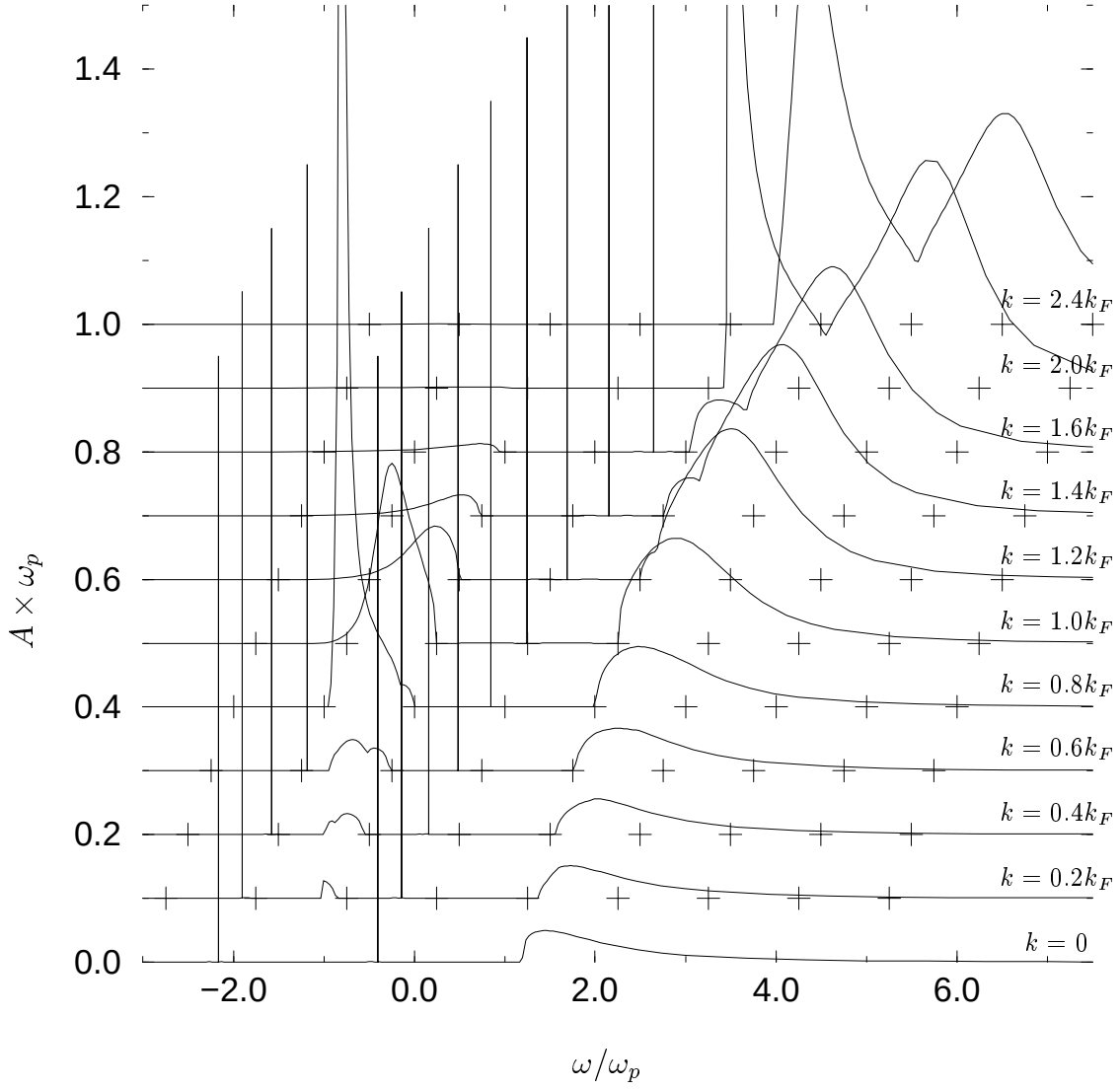

Figure 4.10: The spectral functions for $r_s = 6$ for low values momentum. In our plasmon pole model, the quasiparticle is lossless at low momenta. In addition, there exists a lossless excitation, the plasmaron, at momenta well below the Fermi level [30]. The resulting delta functions for these lossless parts of the spectrum are represented by vertical lines. This figure is essentially identical to figure 6 in Lundqvist 1967 [31]. In the case of x-ray absorption, the core hole lifetime would add additional broadening.

However, we will eventually need a spectral function with the quasiparticle width removed to use in equation 5.43. From this equation, it follows that

$$\mathrm{Im}\left[\frac{G^{ret}_{extr}(\mathbf{k},\omega)}{Z_k} - \int \frac{\hat{A}_{\mathrm{extr}}(\mathbf{k},\omega')d\omega'}{\omega-\omega'-E_{\mathbf{k}}+i\Gamma_{\mathbf{k}}}\right] = 0. \tag{4.66}$$

Where $G^{ret}_{extr}(\mathbf{k},\omega) = \int d\omega' A(\mathbf{k},\omega')/(\omega-\omega'+i\delta)$ is the retarded Green's function. The integral is analytic everywhere above the line $\omega = -i\Gamma_{\mathbf{k}}$. Since the satellite structure is typically broader than the quasiparticle, we assume that $G_{extr}(\mathbf{k},\omega)$ is also analytic in this region so we can shift the origin of ω by $E_{\mathbf{k}}-i\Gamma_{\mathbf{k}}+i\delta(\delta\to 0^+)$ without crossing a line of analyticity. Thus,

$$\mathrm{Im}\left[\frac{G^{ret}_{extr}(\mathbf{k},\omega+E_{\mathbf{k}}-i\Gamma_{\mathbf{k}}+i\delta)}{Z_k} - \int \frac{\hat{A}_{\mathrm{extr}}(\mathbf{k},\omega')d\omega'}{\omega-\omega'+i\delta}\right] = 0 \tag{4.67}$$

and so

$$\hat{A}_{\mathrm{extr}}(\mathbf{k},\omega') = -\frac{1}{\pi}\mathrm{Im}\left[\frac{G^{ret}_{extr}(\mathbf{k},\omega+E_{\mathbf{k}}-i\Gamma_{\mathbf{k}}+i\delta)}{Z_{\mathbf{k}}}\right]. \tag{4.68}$$

Now we express $G^{ret}_{extr}(\mathbf{k},\omega) = (\omega-k^2/2-\Sigma^{ret}(\mathbf{k},\omega))^{-1} - G_{qp}$. Because we are primarily concerned about the behavior of this system at energies well above the Fermi level, we approximate $\Sigma^{ret}(\mathbf{k},\omega)\approx\Sigma(\mathbf{k},\omega)$. To reduce the negative spectral density due to the subtraction of the quasiparticle pole, we use the Gaussian cutoff we introduced before for this purpose in G_{qp}, i.e.,

$$\mathrm{Im}\,G_{qp}(\mathbf{k},\omega+E_{\mathbf{k}}-i\Gamma_{\mathbf{k}}+i\delta) = \frac{-\delta Z^R_{\mathbf{k}}+\omega Z^I_{\mathbf{k}}e^{-\omega/2\omega_p}}{\omega^2+\delta^2}. \tag{4.69}$$

We further replace Z_k by $|Z_k|$ in the above equation, and obtain for $\omega \gg \delta$

$$\begin{aligned}\hat{A}_{\mathrm{extr}}(\mathbf{k},\omega) &= -\frac{1}{\pi|Z_{\mathbf{k}}|}\left[\frac{\Gamma^1_{\mathbf{k}}+\mathrm{Im}\,\Sigma(\mathbf{k},\omega+E^1_{\mathbf{k}})}{(\omega+\Delta E_{\mathbf{k}}-\mathrm{Re}\,\Sigma(\mathbf{k},\omega+E^1_{\mathbf{k}}))^2+(\Gamma^1_{\mathbf{k}}+\mathrm{Im}\,\Sigma(\mathbf{k},\omega+E^1_{\mathbf{k}}))^2}\right. \\ &\quad \left. -\frac{\mathrm{Im}\,Z_{\mathbf{k}}}{\omega}e^{-(\omega/2\omega_p)^2}\right]\end{aligned} \tag{4.70}$$

where $\Delta E_{\mathbf{k}} = \mathrm{Re}\,\Sigma(\mathbf{k},E_{\mathbf{k}})$. We have neglected the $i\Gamma_{\mathbf{k}}$ in the argument for Σ, and as a consequence we must replace $E_{\mathbf{k}}$ by $E^1_{\mathbf{k}}$ and $\Gamma_{\mathbf{k}}$ by $\Gamma^1_{\mathbf{k}}$ everywhere in the above expression. We only consider $\omega\gg\delta$ since G_{extr} is small around $\omega=0$ when the true complex quasiparticle energy is used.

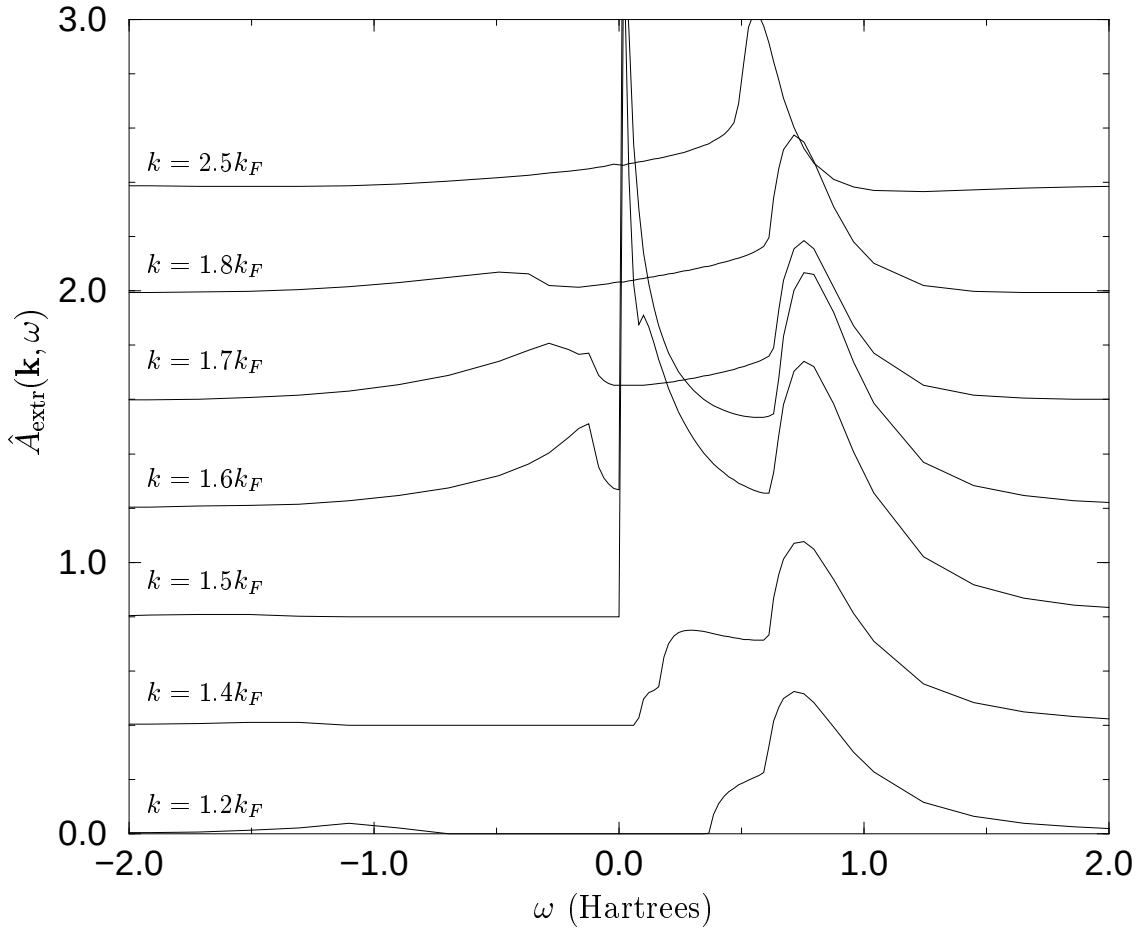

Figure 4.11: The extrinsic satellite spectral functions for $r_s = 2$ at several values of momentum. The curve for $k = 1.4k_F$ illustrates the early stages of the anomalous structure as this structure grows toward the main peak. The curves for $k = 1.5k_F$ and $k = 1.6k_F$ show the anomalous behavior in the vicinity of the quasiparticle. The onset of plasmon losses occurs at $k = 1.67k_F$, above this momentum, the anomalous structure disappears.

The behavior of the extrinsic satellite spectral function is illustrated in figure 4.11. In the plasmon-pole, electron gas model used here, the extrinsic satellite spectral function sometimes exhibits a complicated structure. Close to the Fermi energy, the structure simplifies and consists of a peak at an energy about $\omega_p$above the quasiparticle energy ω and a smooth structure that falls off gradually with increasing energy. For ω near the onset of plasmon losses, there is still a pronounced satellite peak, but there is also an additional "anomalous" structure near the quasiparticle peak. Indeed, it seems ambiguous whether the structure close to the quasiparticle energy should be considered as part of the satellite or the main peak, as the structure accounts for a substantial portion of the extrinsic weight $[1 - Z(\omega)]$ that is not included in the quasiparticle peak. This indicates that the anomalously low and singular behavior of $Z(\omega)$ in this region is partly due to the singular structure of the plasmon-pole approximation and largely an artifact of the *ad hoc* method used to separate the main peak and the "satellite" spectral function. Above the onset of plasmon losses, the anomalous structure disappears, and is replaced by a small tail which extends to the vicinity of the quasiparticle peak. Moreover, as the quasi-particle energy increases, the extrinsic satellite weight becomes progressively smaller.

It is often useful to try to separate the anomalous region of the satellite from the remaining structure, and associate the anomalous peak with the quasiparticle. One method that has proved fairly successful is the following algorithm. Start from the high energy range of the spectral function and scan towards the lower energy direction. Once you have passed the first maximum, check the derivative and the second derivative of the spectral function. If the spectral function is computed before the onset of plasmon losses, stop checking the derivative for negative excitation energies. If the derivative changes sign from negative to positive as you sweep to the left, the anomalous region to be included in the quasiparticle is everything to the left of the place where the derivative changes sign. If the derivative does not change sign, but the second derivative changes sign from negative to positive, the anomalous region

is everything to the left of the location where the second derivative changes sign. This method allows the spectral weight and shape of the anomalous region to vary smoothly with increasing **k**. In the end, the separation of the anomalous region of the extrinsic satellite makes no difference for numerical work where the full excitation spectrum is used, but it can help in gaining a qualitative understanding of what is occurring.

4.4 Ending comments

In this chapter, we have described one of the primary loss mechanisms in XAS, and have derived explicit formulas for the loss spectrum. These extrinsic losses occur in addition to the intrinsic losses described in the previous chapter. The two loss mechanisms are not independant, however. In the next chapter, we will investigate the interference between these two mechanisms and, in the process, develop a general theory of inelastic losses in XAS.

Chapter 5

INTERFERENCE EFFECTS IN X-RAY ABSORPTION

In this chapter, we introduce a general theory of losses in x-ray absorption in which both the core hole and photoelectron are present, including the interference between them. The main result of this dissertation is presented, in which the many body x-ray absorption spectrum can be expressed as a convolution of the single electron calculation for the absorption spectrum with a many body spectral function.

Two types of losses have been discussed so far, the extrinsic losses that occur during the propagation of the photoelectron, and intrinsic losses due to the creation of excitations by the sudden appearance of the core hole. Both types of losses have long been known in x-ray absorption. Both of these loss mechanisms are due to excitations of the same type, namely plasmons and, to a lesser extent, other multi-electron excitations. In x-ray absorption spectra (XAS), the net effect of these excitations is observed to be quite weak, except for the extrinsic effects on the quasiparticle due to a finite lifetime and energy shifts. Naïvely, we would expect from the basic expressions that the effects of the excitations should be much larger. This brings up the question of interference between these two loss channels.

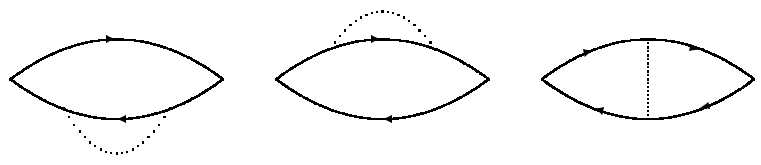

intrinsic extrinsic interference

Figure 5.1: Feynman diagrams of the intrinsic, extrinsic, and interference processes.

Interference is known to be important in photoemission spectroscopy, particularly near threshold [27, 10]. At threshold, the interference between the intrinsic and extrinsic processes is complete, and no collective electronic excitations are possible. In x-ray absorption, Fujikawa has shown that in the vicinity of threshold, a similar cancelation takes place [21]. This corresponds with an intuitive picture of the outgoing photoelectron screening the core hole. When the photoelectron leaves at low energies, it spends much loner in the vicinity of the hole, and their mutual fields tend to cancel, leading to a reduced many body response in the system. At high energies, when the photoelectron leaves quickly, the core hole and the photoelectron behave approximately independently, and we should reduce to a case with negligible interference. However, while the work of Fujikawa explained the weakness of multi-electron excitations at the absorption threshold, the question remains as to what happens at higher energies in XAS.

Much of the work in this chapter has been previously published by Campbell *et al* [15]. We aim to derive a method of dealing with losses in XAS, building on the Hedin and Bardyszewski [23, 10]. We will show that the XAS can be represented as a convolution of the one particle theory with the loss spectrum obtained from an effective one electron Green's function.

5.1 Basic expressions

To consider the effects of interactions between the photoelectron and the core hole state with other electrons in the environment we introduce a set of creation and destruction operators $c_k^\dagger$ and c_k for valence and conduction states $|k\rangle$ with quantum number k, and a creation and destruction operator b for a particular core state $|b\rangle$ involved in the transition. In this representation, our dipole operator becomes

$$\Delta_\varepsilon^N = \sum_k \langle k|d_\varepsilon|b\rangle c_k^\dagger b \tag{5.1}$$

We then construct a "deep-level" Hamiltonian as discussed by Langreth [28]

$$H_0 = H_v + \varepsilon_c b^\dagger b + V b b^\dagger. \tag{5.2}$$

Here H_v is the Hamiltonian of the "outer" (valence and conduction) electrons including the photoelectron, ε_c the energy of the core level, and V is the core hole potential acting on the outer electrons. While this Hamiltonian does not take correlations between the core and valence states into account, it does fully include the correlations of the outer electrons. With this approximation we have

$$V = -\sum_i w(\mathbf{r}_i), \qquad w(\mathbf{r}) = \int v(\mathbf{r}-\mathbf{r}')\rho_b(\mathbf{r}')d\mathbf{r}', \tag{5.3}$$

where $v(\mathbf{r})$ is the Coulomb potential, and $\rho_b(\mathbf{r})$ the charge density of the core electron state $|b\rangle$. It follows that the ground state of H, denoted $|\Psi_0\rangle$, is a product state

$$|\Psi_0\rangle = |\Phi_0\rangle\,|b\rangle\,, \tag{5.4}$$

where $|\Phi_0\rangle$ is the correlated wave function for all the outer electrons:

$$H_v\,|\Phi_0\rangle = E_0^0\,|\Phi_0\rangle\,,\; H\,|\Psi_0\rangle = E_0\,|\Psi_0\rangle\,,\; E_0 = E_0^0 + \varepsilon_c.$$

The core electrons that do not directly participate in absorption process are not considered in this treatment. At this point Eqs. (2.7), (5.1) and (5.4) give

$$\begin{aligned}\mu(\omega) &= -\frac{1}{\pi}\,\mathrm{Im}\sum_{k_1k_2}\langle b|d_\varepsilon^\dagger|k_1\rangle\langle k_2|d_\varepsilon|b\rangle \\ &\times \langle\Phi_0|c_{k_1}\frac{1}{E_0+\omega-H_v'+i\gamma}c_{k_2}^\dagger|\Phi_0\rangle,\end{aligned} \tag{5.5}$$

where

$$H_v' = H_v + V.$$

Our notational scheme will be to use a prime on all quantities affected by the core hole. The x-ray absorption is now reduced to the single electron expression similar to what we had before (equation 2.7)

$$\mu\,(\omega) = -\frac{1}{\pi}\mathrm{Im}\sum_{k_1k_2}\langle b|d_\varepsilon^\dagger|k_1\rangle\langle k_1|G_{\mathrm{eff}}\,(\omega+E_c)\,|k_2\rangle\langle k_2|d_\varepsilon|b\rangle, \tag{5.6}$$

where $G_{\text{eff}}(\omega)$ is the *effective* one electron Green's function

$$\langle k_1|G_{\text{eff}}(\omega)|k_2\rangle = \langle\Phi_0|c_{k_1}\frac{1}{\omega-(H'_v-E'_0)+i\gamma}c^\dagger_{k_2}|\Phi_0\rangle \tag{5.7}$$

in which E'_0 is the ground state energy of H'_v. It is important to note that the wavefunction $|\Phi_0\rangle$ is not an eigenfunction of the operator H'_v appearing in the denominator of the Green's function.

At this point our theory of the many body absorption is general and will in principle, give rise to loss behavior, edge singularities, and deviations from the final state rule. Both the absorption μ and the spectral function $A = |\text{Im}\,G|/\pi$ are everywhere positive. Almbladh and Hedin have developed a transient Green's function approximation to describe the edge shape [2], but we will need to make a different set of approximations to describe losses.

5.1.1 A first look; the Hartee-Fock approximation

To get an idea of the behavior of the Green's function G_{eff}, it is useful first investigate its consequences under the Hartree-Fock approximation. The eigenstates of H_v including $|\Phi_0\rangle$ are Slater determinants built from solutions without the core hole, while the eigenstates that appear in $H'_v = H_v + V$ are those Slater determinants that can be constructed from orbitals which are self consistent solutions with the core hole potential present. Since we can choose any complete set to represent the states k in the dipole operator $\Delta^N_\varepsilon = \sum_k \langle k|d_\varepsilon|b\rangle c^\dagger_k b$, we take the eigenstates of H_v because we wish to have $c^\dagger_k|\Phi_0\rangle = 0$ for $k < K_F$. We then separate H'_v into one term h' with orbitals which describe the photoelectron, and another term to describe the remainder of the system H'_{v0}

$$H'_v = h' + H'_{v0}. \tag{5.8}$$

Both of these terms have interactions with the core hole, V_{pc} and V_{vc} respectively, such that

$$h' = h + V_{pc}, \quad H'_{v0} = H_{v0} + V_{vc} \tag{5.9}$$

where h is the HF photoelectron Hamiltonian without the core hole present, and H_{v0} likewise represents the rest of the system without a core hole. The core hole potentials here are screened by the HF exchange, compared to the bare Coulomb potential of equation 5.3.

Only the one-electron operator h' can couple $c^\dagger_{k_2}$ to c_{k_1} in equation 5.7. Thus we can use a product space, $c^\dagger_k|\Phi_0\rangle = |\Phi_0\rangle|k\rangle$, which then gives for the absorption

$$\mu(\omega) = -\frac{1}{\pi}\mathrm{Im}\,\langle b|d^\dagger_\varepsilon P G_{\mathrm{eff}}(\omega + E_c) P d_\varepsilon|b\rangle, \tag{5.10}$$

where

$$G_{\mathrm{eff}}(\omega) = \left\langle \Phi_0 \left| \frac{1}{\omega - (H'_v - E'_0) + i\gamma} \right| \Phi_0 \right\rangle, \tag{5.11}$$

and P is the projection operator onto unoccupied one-particle states of the initial (no core hole) state is

$$P = \sum_{k>k_F} |k\rangle\langle k|. \tag{5.12}$$

The separation of H'_v into h' and H'_{v0} is certainly an approximation; however, it is an approximation that makes physical sense and which has been used previously in, for example, photoemission problems [24]. The coupling between the photoelectron and the valence electrons is a correlation effect beyond the HF approximation, and is thus neglected in this formulation.

5.1.2 Correlated electron systems

In a correlated electron case, the eigenstates of the Hamiltonian can, in principle, be calculated by configuration interaction theory. Such eigenstates are a superposition of Slater determinants with every possible combination of electron-hole excitations. In the ground state $|\Phi_0\rangle$, those configurations with their virtual excitations near the Fermi level will have the highest amplitude. So long as the photoelectron state k is far from the Fermi level, we can approximate this state as a product space

$$c^\dagger_k|\Phi_0\rangle \approx \begin{cases} |\Phi_0\rangle|k\rangle, & k > k_F \\ 0, & k < k_F. \end{cases} \tag{5.13}$$

We must keep in mind that this can be a poor approximation for k near the Fermi level. As before, we divide the Hamiltonian into a photoelectron term h' and a term describing the valence electrons and their excitations H'_{v0}, with the same core hole potentials from equation 5.9. Unlike the Hartree-Fock case, we have an additional term coupling the photoelectron to the valence electrons.

$$V_{pv} = \sum_{k_1 k_2} \sum_{l_1 l_2}^{val} \langle k_1 l_1 || v || k_2 l_2 \rangle c^\dagger_{k_1} c_{k_2} \left[c^\dagger_{l_1} c_{l_2} - \langle c^\dagger_{l_1} c_{l_2} \rangle \right] \tag{5.14}$$

where $\langle k_1 l_1 \,||v||\, k_2 l_2 \rangle$ is an antisymmetrized matrix element of the Coulomb potential $v(\mathbf{r})$ with the expectation value $\langle c^\dagger_{l_1} c_{l_2} \rangle$ is subtracted off, since it is already included in the definition of h'. While the ground state $|\Phi_0\rangle$ is an eigenfunction of H_{v0} built from one-electron eigenfunctions without the core hole potential, the photoelectron Hamiltonian, h', is built from eigenfunctions $|k'\rangle$ with a core hole present,

$$h' = \sum_{k' > k_F} \varepsilon_k \, |k'\rangle\langle k'|. \tag{5.15}$$

Because the states $|k'\rangle$ are scattering states, there is a one to one correspondence between $|k'\rangle$ and $|k\rangle$, and the energies are unchanged. Since h' is bilinear in the photoelectron operators c_k and there is a linear relation between the states $|k'\rangle$ and $|k\rangle$, the action of h' on any element in the product space $|\Phi_0\rangle|k\rangle$ will not take us outside the product space.

Equations 5.5 and 5.13 one again yield equation 5.10 for the absorption, but now $G_{\text{eff}}(\omega)$ is given by

$$G_{\text{eff}}(\omega) = \left\langle \Phi_0 \left| \frac{1}{\omega - (H'_{v0} - E'_0) - h' - V_{pv} + i\gamma} \right| \Phi_0 \right\rangle. \tag{5.16}$$

The equations 5.8, 5.9, 5.10, and 5.16 are the starting point for this investigation into the many body effects on x-ray absorption.

5.2 Limiting cases

It is informative to begin our investigation of the theoretical model we have developed by looking at two limits. The first of these is the case of no extrinsic effects, where

we set $V_{pv} = 0$. The second is to neglect the effects of the core hole $H'_{v0} = H_{v0}$.

5.2.1 No extrinsic scattering

When $V_{pv} = 0$ we can expand the effective Green's function in eigenstates $|\Phi'_n\rangle$ of H'_{v0} with eigenvalues E'_n and (with γ an infinitesimal) we obtain

$$G_{\text{eff}}(\omega) = \sum_n \frac{|\langle \Phi_0 | \Phi'_n \rangle|^2}{\omega - \omega_n - h' + i\gamma}, \tag{5.17}$$

where $\omega_n = E'_n - E'_0$. When we expand the identity in terms of the eigenstates $|k'\rangle$ of h' on either side of the Green's function in equation 5.6, and taking the imaginary part, we obtain

$$\begin{aligned} \mu(\omega) &= \sum_{k,n} |\langle \Phi_0 | \Phi'_n \rangle|^2 |\langle k' | P d_\varepsilon | b \rangle|^2 \delta(\omega + E_c - \omega_n - \epsilon_k) \\ &= \int_0^{\omega + E_c - E_F} d\omega' \, A(\omega') \mu^{(1)}(\omega + E_c - \omega'). \end{aligned} \tag{5.18}$$

The core-hole spectral function $A(\omega)$ is defined as

$$A(\omega) = \sum_n |\langle \Phi_0 | \Phi'_n \rangle|^2 \delta(\omega - \omega_n), \tag{5.19}$$

and the one electron XAS as

$$\mu^{(1)}(\omega) = \sum_{k' > k_F} |\langle k' | P d_\varepsilon | b \rangle|^2 \delta(\omega - \epsilon_k). \tag{5.20}$$

This form is similar to the previous result from equation 3.9. However, the projection operator P in the dipole matrix element introduces an edge singularity from the singular nature of the $\langle k | k' \rangle$ overlap of the projection operator P in the dipole matrix element [19]. It is interesting to note that $A(\omega)$ contains the core electron edge singularity $A(\omega) \approx \omega^{\alpha - 1}$, where α is the singularity index, and that $\mu^{(1)}(\omega)$ is also singular at the Fermi level, $\mu^{(1)}(\omega) \approx (\omega - E_F)^\beta$. This latter singularity follows from the singular behavior of the overlap integral $\langle k' | k \rangle$ [29]. We also see from Eq. (5.20) that the final state rule is not strictly valid, except well above threshold, where P

can be replaced by a δ-function and the matrix element reduces to $\langle k'|d|b\rangle$. We know from photoemission [25] that there is little extrinsic scattering at threshold, where this limiting case should be a good representation of our basic approximation given by Eqs. (5.10) and (5.16).

5.2.2 No core hole

When the core-hole potential is neglected then $H'_{v0} = H_{v0}$ and $h' = h$. This gives for our Green's function (with γ an infinitesimal)

$$G_{\text{eff}}(\omega) = \left\langle \Phi_0 \left| \frac{1}{\omega - (H_{v0} - E_0) - h - V_{pv} + i\gamma} \right| \Phi_0 \right\rangle . \tag{5.21}$$

This is a Green's function in its standard form $G(\omega)$ For the Green's function between two photoelectron states k_1 and k_2 we have

$$\langle k_1|G(\omega)|k_2\rangle = \langle 0| \left\langle \Phi_0 \left| c_{k_1} \frac{1}{\omega - (H_{v0} - E_0) - h - V_{pv} + i\gamma} c^\dagger_{k_2} \right| \Phi_0 \right\rangle |0\rangle. \tag{5.22}$$

Here, $V_{pv}|0\rangle = 0$, and thus $|\Phi_0\rangle\,|0\rangle$ is an eigenfunction of the full Hamiltonian $H_{v0} + h + V_{pv}$. We can express G in the spectral representation for a spectral function $A(\omega)$,

$$\begin{aligned} \langle k_1|G(\omega)|k_2\rangle &= \int_{E_F}^{\infty} \frac{\langle k_1|A(\omega')|k_2\rangle d\omega'}{\omega - \omega' + i\gamma} \\ &= \langle k_1| \frac{1}{\omega - h - \Sigma(\omega)} |k_2\rangle. \end{aligned} \tag{5.23}$$

This limiting case yields results similar to that of the one electron theory, except for the addition of a additional complex, energy dependent one-electron potential $\Sigma(\omega)$. If $\langle k_1|\Sigma(\omega)|k_2\rangle$ is approximated by a diagonal self energy $\Sigma(\mathbf{k},\omega)$, we obtain the results of chapter 4. If we go further and replace the self energy by a constant $[\Delta E(k_1) - i\Gamma(k_1)]\delta(k_1 - k_2)$, we are operating in the quasiparticle approximation and we recover the single electron result from chapter 2.

5.3 Quasi-boson representation

In the general case all three potentials V_{pv}, V_{pc} and V_{vc} that couple between the the photoelectron, the valence electrons, and the core electron are nonzero. In order to deal with this case we introduce a quasi-boson model Hamiltonian,

$$H_{v0} = \sum_n \omega_n a_n^\dagger a_n, \qquad h' = \sum_{k>k_F} \epsilon_k c_k^\dagger c_k, \tag{5.24}$$

$$V_{vc} = -\sum_n V_{bb}^n (a_n^\dagger + a_n), \tag{5.25}$$

$$V_{pv} = \sum_{nk_1k_2} [V_{k_1k_2}^n a_n^\dagger + (V_{k_1k_2}^n)^* a_n] c_{k_1}^\dagger c_{k_2}. \tag{5.26}$$

This model, with equations 5.9, 5.10 and 5.16, are the basic approximations we use for our theory of interference. Because $h|\Phi_0\rangle = 0$, the potential V_{pc} does not come into our expressions explicitly. Therefore, we do not have to worry about the transform between the h and h' states.

This quasi-boson model has been discussed in references [10] and [24]. The basic idea is that the electron-hole type excitations are approximated as bosons with creation operators a_n and energies ω_n, and the charge density fluctuation coupling is expressed as a term which is linear in the boson operators, as in equation 5.26. Equation 5.25 is a special case of equation 5.26 where the valence and conduction creation and annihilation operators $c_{k_1}^\dagger$ and c_{k_2} are replaced by those for the core hole, b and $b^\dagger$, with a minus sign for the opposite charge on the core hole. The potentials V^n are fluctuation potentials corresponding for the excited states n. The V^n can be obtained from a theory of the dielectric function. Hedin*et al* found the fluctuation potentials using an RPA type dielectric function [25], but here we shall use the plasmon pole coupling from equation 4.21. With the quasiboson model Hamiltonian we can solve explicitly for the relation between the ground states with and without a core hole, from H'_{v0} and $H_{v0}h$ respectively [10]. First, we note that we can represent $|\Phi_0\rangle = e^{-S}|\Phi'_0\rangle$, where the operator S is linear in the creation operators $a_n^\dagger$, $S = \sum_n A_n a_n^\dagger + C_n$. Since the creation operators commute for different modes n, we

need only consider one mode. The Hamiltonian for such a system is given by

$$\begin{aligned} \mathcal{H} &= \omega \hat{a}^\dagger a \\ \mathcal{H}' &= \omega \hat{a}^\dagger \hat{a} - V(\hat{a}^\dagger + \hat{a}). \end{aligned} \tag{5.27}$$

We can write $\mathcal{H}' = \omega \bar{a}^\dagger \bar{a} - V^2/\omega$ where $\bar{a} = \hat{a} - V/\omega$. Now, for a state of occupied by v bosons, we have

$$\begin{aligned} \langle \Phi_v' | \Phi_0 \rangle &= \langle \Phi_0' | \bar{a}^v (v!)^{-1/2} | \Phi_0 \rangle \\ &= \langle \Phi_0' | (a - V/\omega)^v (v!)^{-1/2} | \Phi_0 \rangle \\ &= \langle \Phi_0' | \Phi_0 \rangle (-V/\omega)^v (v!)^{-1/2}. \end{aligned} \tag{5.28}$$

Further, by definition,

$$\begin{aligned} \langle \Phi_v' | \Phi_0 \rangle &= \langle \Phi_v' | e^{-S} | \Phi_0' \rangle \\ &= \langle \Phi_v' | \sum_{j=0}^{\infty} (-1)^{v+j} \frac{S^{v+j}}{(v+j)!} | \Phi_0' \rangle \\ &= \langle \Phi_v' | \sum_{j=0}^{\infty} (-1)^{v+j} \frac{A^v (\bar{a}^\dagger)^v C^j}{j! v!} | \Phi_0' \rangle \\ &= \langle \Phi_v' | \frac{(-A\bar{a}^\dagger)^v}{v!} e^{-C} | \Phi_0' \rangle \\ &= \frac{(-A)^v}{(v!)^{1/2}} e^{-C}. \end{aligned} \tag{5.29}$$

$$\tag{5.30}$$

From this, we immediately see that $\langle \Phi_0' | \Phi_0 \rangle = e^{-C}$. Thus, from equations 5.28 and 5.29 we find $A = V/\omega$. When we note that $\sum_v |\langle \Phi_v' | \Phi_0 \rangle|^2 = 1 = e^{A^2} e^{-2C}$, we see that $C = A^2/2$. Thus,

$$S = (V/\omega)\bar{a}^\dagger + \frac{1}{2}(V/\omega)^2.$$

Generalizing to all boson modes,

$$S = \frac{a}{2} + \sum_n \frac{V_{bb}^n}{\omega_n} \bar{a}_n^\dagger, \; a = \sum_n \left(\frac{V_{bb}^n}{\omega_n} \right)^2, \tag{5.31}$$

Expanding to second order in the coupling potentials V^n, we obtain

$$G_{\text{eff}}(\omega) = \left\langle \Phi_0' \left| e^{-S^\dagger} \frac{1}{\omega - (H_{v0}' - E_0') - h' - V_{pv} + i\gamma} e^{-S} \right| \Phi_0' \right\rangle$$

$$= e^{-a} \left\{ G(\omega) + \sum_n \left(\frac{V_{bb}^n}{\omega_n} \right)^2 G(\omega - \omega_n) - 2 \sum_n \frac{V_{bb}^n}{\omega_n} G(\omega - \omega_n) V^n G(\omega) \right\}, \qquad (5.32)$$

where

$$\begin{aligned} G(\omega) &= \left\langle \Phi_0' \left| \frac{1}{\omega - (H_{v0}' - E_0') - h' - V_{pv} + i\gamma} \right| \Phi_0' \right\rangle \\ &\equiv \frac{1}{\omega - h' - \Sigma(\omega) + i\gamma}, \end{aligned} \qquad (5.33)$$

is the damped Green's function for a system with a core hole. With this form for $G_{\text{eff}}(\omega)$ we can now express $\mu(\omega)$ from equation 5.10 as a sum of one-particle Green's functions, thus achieving our goal of avoiding the calculation of correlated many body final states. Note that all the limiting expressions in section 5.2 are the same when we use the quasi-boson model.

5.4 Qualitative discussion of the 2nd order expression

The expressions in equations 5.10 and 5.16 which comprise our basic approximations give a positive absorption. However, the terms in the expansion of equation 5.32 need not be positive when taken individually. An estimate for the strength of the expansion parameters V^n can be obtained from the dimensionless constant a from equation 5.31. In an electron gas with values for typical solid densities, a ranges from 0.2 to 0.4 when considering only the plasmon excitations. For energies insufficient to excite plasmon modes, the quasiparticle spectral weight Z is roughly e^{-a}, which takes values of 0.8 to 0.7 for typical solid densities. However, in XAS we generally do not see effects of order a. We can take this as empirical evidence that the loss mechanisms largely cancel.

Due to the large values of a, this second order approximation can give rise to non-physical results in the numerical computations. In particular, the spectral func-

tion can become negative over small energy ranges. Taking higher order effects into account would be expected to significantly reduce this problem. However, as will be shown later, there are ways to correct for this effect so that the spectra themselves do not show non-physical behaviors.

To summarize and simplify, we remove a factor of e^{-a} from the definition of G_{eff} in equation 5.16, giving us an absorption of

$$\mu(\omega) = -\frac{e^{-a}}{\pi}\text{Im } \langle b|d_\varepsilon^\dagger P G_{\text{eff}}(\omega + E_c) P d_\varepsilon|b\rangle, \tag{5.34}$$

where

$$\begin{aligned} G_{\text{eff}}(\omega) = G_{qp}(\omega) &+ G_{extr}(\omega) + G_{intr}(\omega) + G_{inter}(\omega), \\ G_{qp}(\omega) &+ G_{extr}(\omega) = G(\omega), \\ G_{intr}(\omega) &= \sum_n \left(\frac{V_{bb}^n}{\omega_n}\right)^2 G(\omega - \omega_n), \\ G_{inter}(\omega) &= -2\sum_n \frac{V_{bb}^n}{\omega_n} G(\omega - \omega_n) V^n G(\omega), \end{aligned} \tag{5.35}$$

are the Green's functions for the quasiparticle term, the extrinsic and intrinsic satellite terms, and the interference between these three terms. In order to deal with the one particle Green's function $G(\omega)$ we make the assumption that $\Sigma(\omega)$ is diagonal in the $|k'\rangle$ basis of eigenvectors for h'. Hedin has shown [24] that this is a fairly good approximation. To avoid unnecessary clutter of notation, we drop the prime on the photoelectron quantum number k' and write

$$\langle k|G(\omega)|k\rangle \equiv G(k,\omega) = \frac{1}{\omega - \varepsilon_k - \Sigma(k,\omega) + i\gamma}. \tag{5.36}$$

As discussed in sections 4.2 and 4.3, $G(k,\omega)$ as a function of ω has a quasiparticle peak and a satellite structure The quasiparticle occurs at E_k which is defined from $E_k = \text{Re}\, E_p = k^2/2 + \text{Re}\, \Sigma(k, E_p)$, with E_p the (complex) energy of the quasiparticle pole ($E_p = k^2/2 + \Sigma(k, E_p)$). The quasiparticle has a width $\Gamma_k = |\text{Im}\, \Sigma(k, E_p)|$ and a weight $Z_k = [1 - \partial\Sigma(k,\omega)/\partial\omega]^{-1}_{\omega = E_p}$. For our purposes, it will be sufficient in most cases

to approximate $E_p = E_k = k^2/2 + \mathrm{Re}\,\Sigma(k, E_k)$; unless explicitly stated otherwise, this is the approximation we will use throughout the rest of this thesis. We thus will write a quasiparticle Green's function as

$$G(k,\omega) \approx \langle k|G_{qp}(\omega)|k\rangle = \frac{Z_k}{\omega - E_k + i\Gamma_k}. \tag{5.37}$$

We now make an on-shell approximation, defining the quasiparticle properties as functions of ω,

$$Z(\omega) = Z_k,\ \Delta E(\omega) = \Delta E_k,\ \Gamma(\omega) = \Gamma_k,$$

where the relation between k and ω is given implicitly through

$$\omega = E_k. \tag{5.38}$$

With the on-shell approximation we obtain

$$\langle k|G_{qp}(\omega)|k\rangle \approx \left\langle k \left| \frac{Z(\omega)}{\omega - h' - \Delta E(\omega) + i\Gamma(\omega) + i\gamma} \right| k \right\rangle, \tag{5.39}$$

and since the $|k\rangle$ are eigenfunctions of h', the operator $G_{qp}(\omega)$ becomes

$$G_{qp}(\omega) = \frac{Z(\omega)}{\omega - h' - \Delta E(\omega) + i\Gamma(\omega) + i\gamma}. \tag{5.40}$$

We can use this form of the quasiparticle in the one electron formalism developed in chapter 2. From equations 5.34, 5.35, and 5.40, the quasiparticle contribution to the x-ray absorption is given by

$$\mu_{qp}(\omega - E_c) = -\frac{e^{-a}}{\pi}\mathrm{Im}\,\langle b|d^\dagger P G_{qp}(\omega) P d|b\rangle. \tag{5.41}$$

This is form of the absorption is similar to the standard one-electron formula for the x-ray absorption $\mu^{(1)}(\omega)$ with the mean free path taken from the quasiparticle width $\Gamma(\omega)$, but there are differences in the form of a complex amplitude factor $Z(\omega) = \exp(i\phi)|Z(\omega)|$ with its many body phase shift ϕ, and a wave-function overlap reduction factor e^{-a}.

The expressions in equation 5.35 are only expanded to second order in the fluctuation potentials V^n. If we replace the full extrinsic electron Green's function $G(\omega)$ by the quasiparticle $G_{qp}(\omega)$ in the interference and intrinsic functions $G_{inter}(\omega)$ and $G_{intr}(\omega)$, we are still correct to the same order of approximation. We can then define the extrinsic satellite function $G_{extr}(\omega)$ as the difference between the full propagator $G(\omega)$ and the quasiparticle propagator $G_{qp}(\omega)$, as is discussed in section 4.3. As we noted earlier, the projection operator P found in equations 5.34 and 5.20 is responsible for edge singularities and deviations from the final state rule, but does not significantly affect the fine structure.

Once we assume that G_{eff} (see equation 5.35) is diagonal in the one-particle index k, from Eq. (5.34) we find

$$\mu(\omega - E_c) = -\frac{e^{-a}}{\pi} \sum_k \left| \langle b|d^\dagger P|k\rangle \right|^2 \operatorname{Im} G_{\text{eff}}(k,\omega), \tag{5.42}$$

GW calculations show that G and G_{qp} are approximately diagonal [24], so this should be a good approximation for all the contributions to G_{eff} except for the interference G_{inter}, which will require special treatment as is described later in this chapter.

Let us define the real spectral weight function $\hat{A}_{\text{eff}}(k,\omega)$ by representing $\operatorname{Im} G_{\text{eff}}(k,\omega)$ as

$$\operatorname{Im} G_{\text{eff}}(k,\omega) = \int d\omega' \hat{A}_{\text{eff}}(k,\omega') \operatorname{Im} G_{qp}(k,\omega-\omega'). \tag{5.43}$$

We use a hat to distinguish the spectral weight function which has been deconvolved with the quasiparticle $\hat{A}(k,\omega)$ from the "physical" spectral weight function $A(k,\omega) = -\frac{1}{\pi}\operatorname{Im} G(k,\omega)$. Now we make the on-shell approximation by replacing k in $\hat{A}_{\text{eff}}(k,\omega')$ by $k = k(\omega-\omega')$, with $k(\omega)$ defined in equation 5.38. Now that $\hat{A}_{\text{eff}}(\omega,\omega') \equiv \hat{A}_{\text{eff}}(k(\omega-\omega'),\omega')$ depends only on ω and ω', we can sum over k to obtain

$$\mu(\omega) = \int d\omega' \hat{A}_{\text{eff}}(\omega,\omega')\, \mu_{qp}(\omega-\omega'). \tag{5.44}$$

Note that the quasiparticle contribution to $\hat{A}_{\text{eff}}(\omega,\omega')$ is simply a delta-function, $\hat{A}_{qp}(\omega,\omega') = \delta(\omega')$.

Numerical analysis of this theory for real condensed systems can be a daunting endeavor. As such, only rough estimates of the effects will be carried out here, which hopefully will illustrate the theory and give rise to non-negligible corrections to XAS theory [44]. One of these simplifications is the use of the electron gas model with a plasmon pole dielectric function when evaluating the effective spectral function. This model should be sufficient for this semi-quantitative pilot study. The theory of interference is more general, however, and could be applied to real systems by those willing to undertake more extensive calculations. In the next couple chapters, we will show how some of the main ingredients in this theory can be calculated, namely, the projection operator in the dipole matrix elements and the intrinsic and interference terms in the effective spectral function.

Chapter 6

EDGE SINGULARITY EFFECTS

In this chapter, we calculate the edge singularities described in Chapter 3, using the projection operator formalism of Chapter 5. The effects of these singularities on two materials, copper and titanium, are shown.

The projection operator introduced in equation 5.12 can be rewritten as

$$P = 1 - \sum_{k<k_F} |k\rangle\langle k|. \tag{6.1}$$

When inserted into equation 5.20, it gives the result

$$\mu^{(1)}(\omega) = \sum_{k'>k_F} \left| \langle k'|d|b\rangle - \sum_{k<k_F} \langle k'|k\rangle\langle k|d|b\rangle \right|^2 \delta(\omega - \epsilon_k). \tag{6.2}$$

It has been shown by Friedel [18] [19] that in a large sphere of radius R the matrix element between an unperturbed state in a metal with radial quantum number m and angular momentum state l and a state with radial quantum number n perturbed by a scattering potential with phase shift η_{nl} and the same angular momentum is

$$u_{mn} = \frac{\sin(\eta_{nl})}{\eta_{nl} + (m-n)\pi}. \tag{6.3}$$

The boundary conditions at the surface of the sphere yield

$$\begin{aligned} kR &= l\pi/2 + m\pi \\ k'R &= l\pi/2 + n\pi - \eta_l \end{aligned} \tag{6.4}$$

for the initial and final wavenumbers, respectively. Thus, extending to infinite R and a continuum of states, we obtain

$$\langle k'|k\rangle = \frac{\sin(\eta_l(k'))}{k - k'}. \tag{6.5}$$

It is this singular overlap between the initial and final states that leads to the edge singularity.

We can now evaluate equation 6.1 numerically. The dipole matrix elements $\langle k|d_\varepsilon|b\rangle$, $\langle k'|d_\varepsilon|b\rangle$, and the phase shifts η_l can be calculated with the code FEFF8, so that we have all the components to estimate the corrections to the final state rule single body absorption.

The singular nature of the wave function overlap is broadened by replacing the sharp cutoff in the states from Eq. 6.2 by a Fermi function at finite temperature

$$\mu^{(1)}(\omega) = \sum_{k'>k_F} \left| \langle k'|d|b\rangle - \sum_k \langle k'|k\rangle\langle k|d|b\rangle F(k,T) \right|^2 \delta(\omega - \epsilon_k) \tag{6.6}$$

$$F(k,T) = \frac{1}{\exp[\omega(k) - \varepsilon_F)/(k_B T)] + 1}, \tag{6.7}$$

and by replacing the real k' in Eq. 6.5 with a complex momentum $p' = k' + i\lambda^{-1}$, where λ is the mean free path of the photoelectron in state k'.

The edge enhancement due to the projection operators cannot be taken independantly of other many body effects. The convolution with the spectral function also contains a singular reduction in the edge intensity as shown by Friedel [20]. In the next chapter, we develop forms for the intrinsic and interference contributions to the spectral function which, along with the extrinsic satellite from Chapter 4, will give us all the elements we need to perform this convolution.

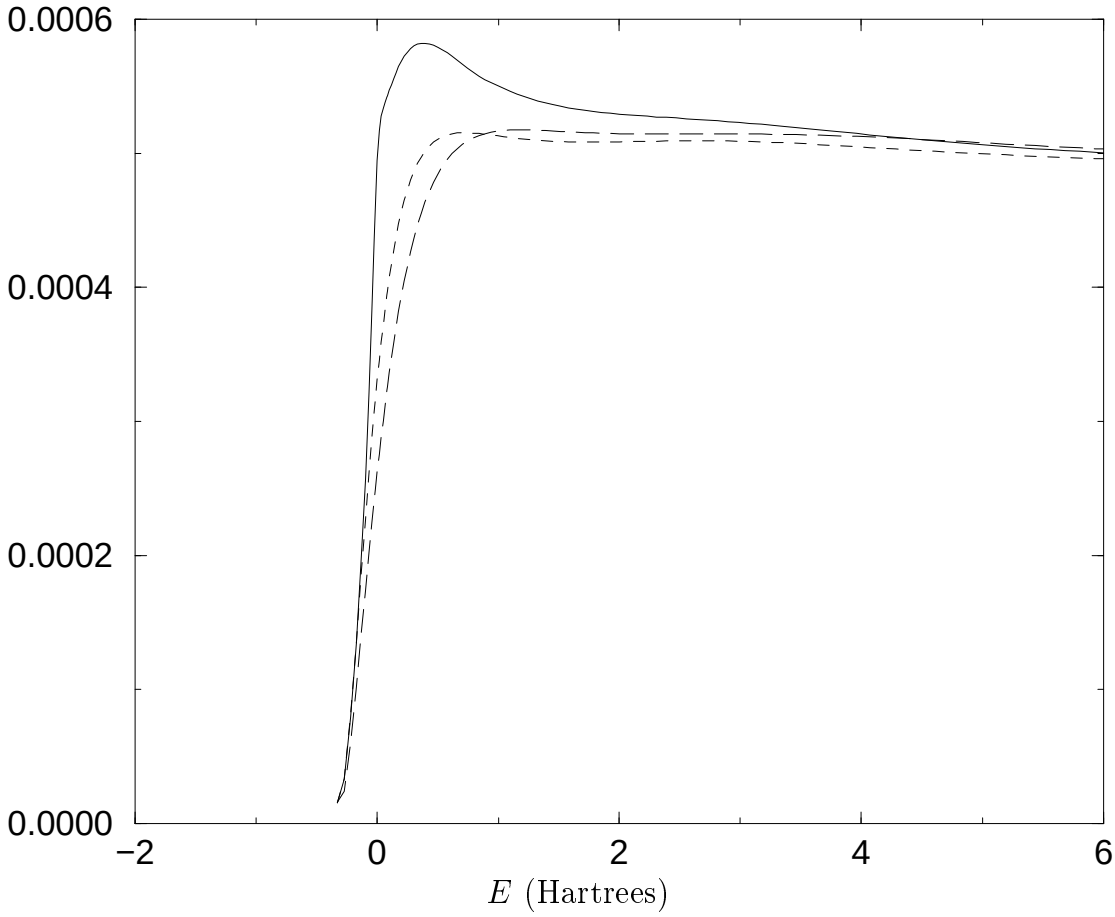

Figure 6.1: The effects of the projection operator on the dipole matrix elements of copper are shown, the solid line shows the projected matrix element $|\langle k'|Pd_\varepsilon|b\rangle|^2$ compared to the matrix element with the core hole potential $|\langle k'|d_\varepsilon|b\rangle|^2$ (short dashes) and that without the core hole potential $|\langle k|d_\varepsilon|b\rangle|^2$ (long dashes). The matrix elements with and without the core holes were computed for crystalline copper by the code FEFF. Energy is measured with respect to the Fermi level.

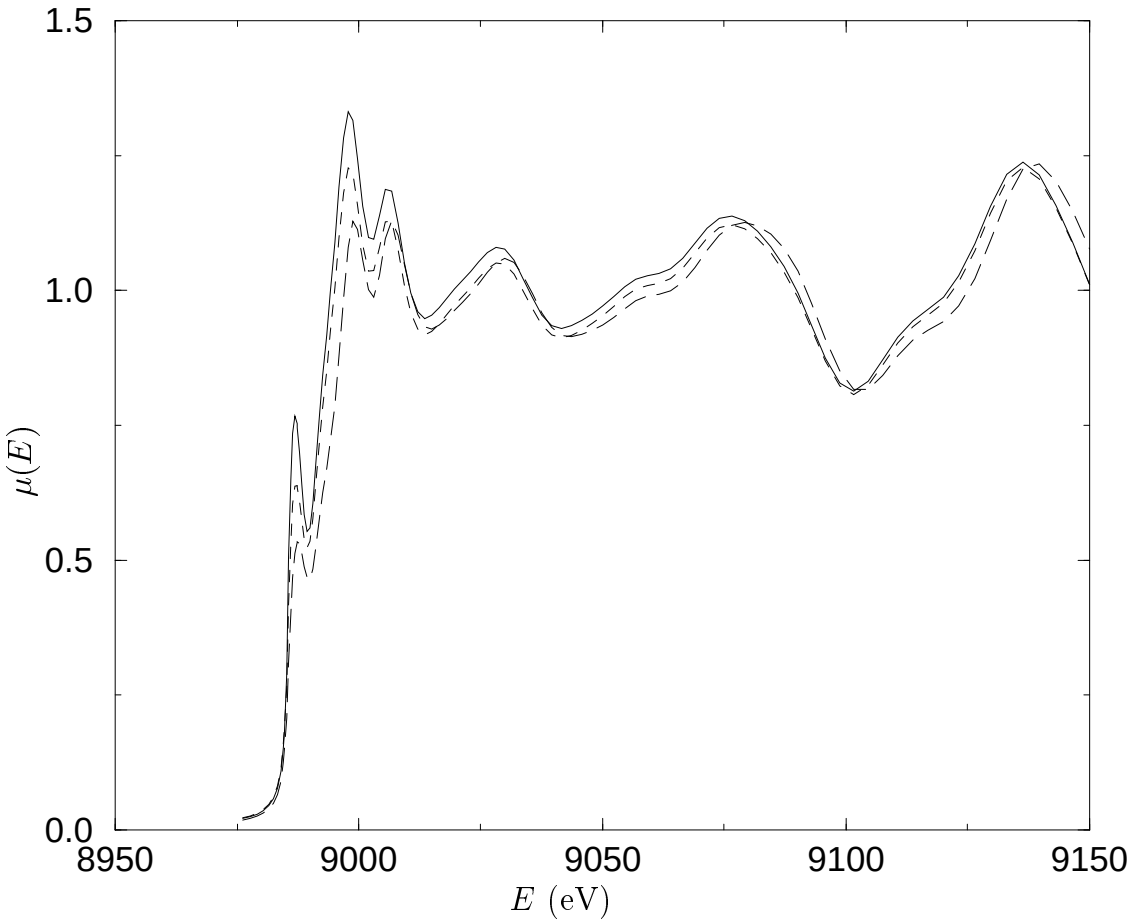

Figure 6.2: The XANES of copper computed with (short dashes) and without (long dashes) the core hole, and with the projection operator in the dipole matrix elements (solid).

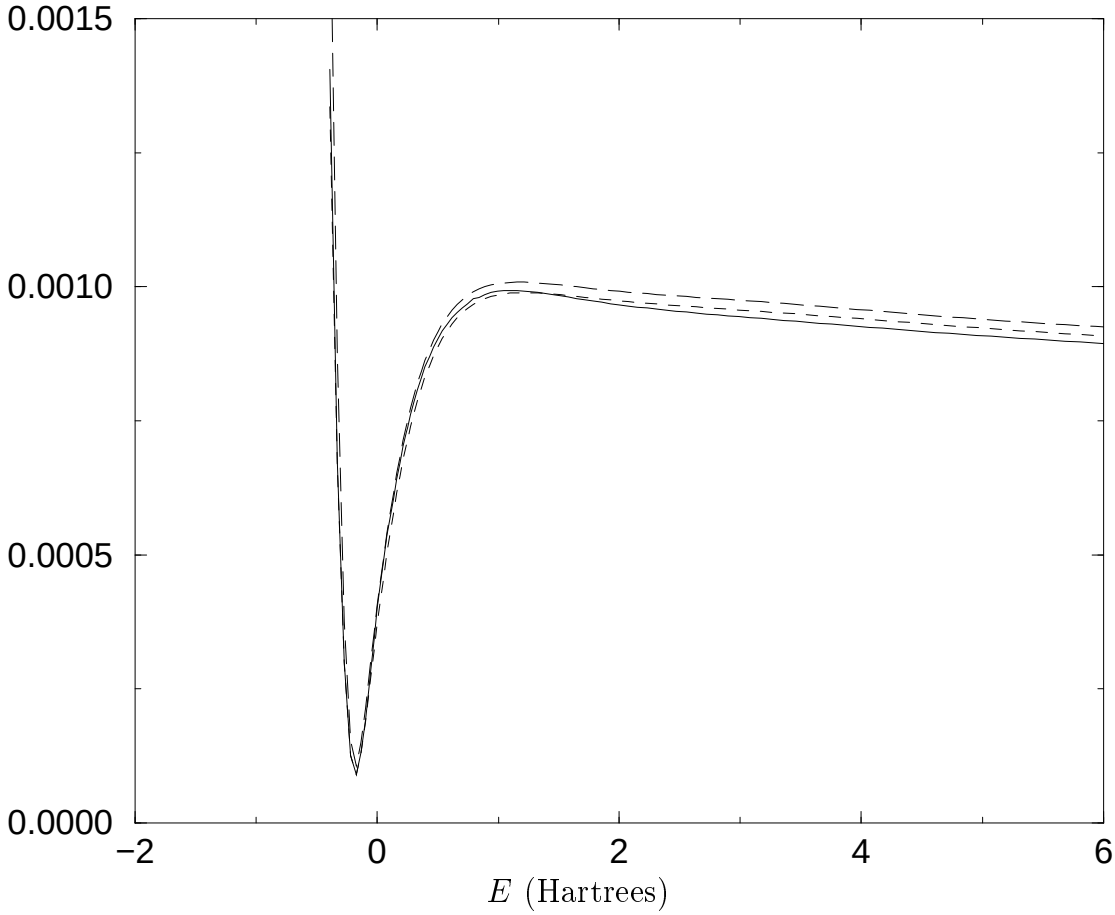

Figure 6.3: The effects of the projection operator on the dipole matrix elements of titanium are shown, the solid line shows the projected matrix element $|\langle k'|Pd_\varepsilon|b\rangle|^2$ compared to the matrix element with the core hole potential $|\langle k'|d_\varepsilon|b\rangle|^2$ (short dashes) and that without the core hole potential $|\langle k|d_\varepsilon|b\rangle|^2$ (long dashes). The matrix elements with and without the core holes were computed for crystalline copper by the code FEFF. Energy is measured with respect to the Fermi level. In this system, the strong reduction of the magnitude of the dipole matrix elements just below the edge means that the projection integral has very little effect, and there is not any significant difference between the single particle and the many body matrix elements.

Chapter 7

EXPRESSIONS FOR THE INTRINSIC AND INTERFERENCE LOSSES IN THE PLASMON POLE ELECTRON GAS

In this chapter, we derive explicit forms for the interference satellite terms and intrinsic contributions to the many body spectral function in the plasmon pole free electron gas. Together with the extrinsic satelite calculated in Chapter 4, we have all the ingredients for the complete many body spectral function. In addition, we cover difficulties that arise with this second order formulation and describe how they may be corrected in practice.

For the computation of the satellite terms, we take $G(\omega, \omega') = (\omega - E_k(\omega) - i\delta)$. If, in the calculation of the satellite terms we ignore the small many body phase, we find that Eq. 5.43 gives us

$$\hat{A}_{intr}(\omega, \omega') = \frac{1}{|Z(\omega)|} \mathrm{Im}\, G_{intr}(\omega, \omega') \tag{7.1}$$

$$\hat{A}_{inter}(\omega, \omega') = \frac{1}{|Z(\omega)|} \mathrm{Im}\, G_{inter}(\omega, \omega') \tag{7.2}$$

From equations 5.35 and 4.21, we can write the intrinsic contributions as

$$\hat{A}_{intr}(\omega, \omega') = \int \frac{d^3q}{(2\pi)^3} \frac{2\pi\omega_p^2}{q^2\omega_q^3|Z(\omega)|} \delta(\omega' - \omega_q). \tag{7.3}$$

Inserting our dispersion relation (equation 4.11), we can do the integral analytically to find

$$\hat{A}_{intr}(\omega, \omega') = \frac{\omega_p^2 \theta(\omega' - \omega_p)}{\pi(\omega')^2 (A + q^2(\omega')/2) q(\omega')}. \tag{7.4}$$

where $q(\omega)$ is the solution to $\omega_q = \omega$. This gives a pronounced satellite structure which only contributes spectral weight above the plasma frequency ω_p. It peaks at

the plasma frequency, and rapidly declines at higher frequencies ω'. The intrinsic satellite does not depend on the quasiparticle energy ω, unlike all the other satellite contributions which decline at high quasiparticle energies. Thus, at high energies, only the intrinsic contribution and the quasiparticle remain and we reduce to the sudden approximation.

The interference contributions from equation 5.35 are not diagonal in k; V^n can transfer momentum between the Green's functions in the term $G(\omega-\omega_n)V^nG(\omega)$. However, we wish to force the interference terms into a form that can be used in equation 5.44. This requires several further approximations. First, we take the fluctuation potentials as plane waves, such that $\langle k+q'|V^q|k\rangle = V_0^q\delta_{qq'}$. Second, we take the Green's functions as diagonal in a plane wave basis. Then, from equations 5.35 and 5.34 we obtain

$$\mu_{inter}(\omega) = \frac{2e^{-a}}{\pi}\mathrm{Im}\sum_{kq}\frac{|V_0^q|^2}{\omega_q}\langle b|d^\dagger P|k+q\rangle\langle k+q|G(\omega-\omega_q)|k+q\rangle\,\langle k|G(\omega)|k\rangle\langle k|Pd|b\rangle. \tag{7.5}$$

Now we approximate $G(\omega)$ by the one electron Green's function, and further we neglect the q dependence in the dipole matrix element above, to obtain

$$\begin{aligned}\mu_{inter}(\omega) &= \frac{2e^{-a}}{\pi}\mathrm{Im}\sum_{kq}\frac{|V_0^q|^2}{\omega_q}\,|\langle k|Pd|b\rangle|^2\,\frac{1}{\omega_q+E_{k+q}-E_k}\times \\ &\quad\times\left[\frac{1}{\omega-\omega_q-E_{k+q}+i\Gamma_{k+q}}-\frac{1}{\omega-E_k+i\Gamma_k}\right],\end{aligned} \tag{7.6}$$

where we have made the approximation that $\Gamma_{k+q}\simeq\Gamma_k$ in the denominator of the prefactor before the term in brackets. We now have a difference between two Green's functions, and we can again write $\mu_{inter}(\omega)$ as a convolution with μ_{qp}, i.e.,

$$\mu_{inter}(\omega)\approx 2\left[a(\omega)\mu_{qp}(\omega)-\int d\omega'\hat{A}^{sat}_{inter}(\omega,\omega')\mu_{qp}(\omega-\omega')\right], \tag{7.7}$$

with

$$a(\omega)=\sum_q\frac{|V_0^q|^2}{\omega_q}\frac{1}{\omega_q+E_{k+q}-E_k}\bigg|_{k=k(\omega)}, \tag{7.8}$$

$$\hat{A}^{sat}_{inter}(\omega,\omega') = \sum_q \frac{|V_0^q|^2}{\omega_q} \frac{1}{\omega_q + E_k - E_{k-q}}\bigg|_{k=k(\omega-\omega')} . \tag{7.9}$$

We now have a term $a(\omega)$ that contributes to the quasiparticle, and a term $\hat{A}^{sat}_{inter}$ that subtracts from the satellite. Now,

$$a(\omega) = \frac{\omega_p^2}{4\pi k}\int_0^\infty d\omega' \frac{1}{\omega'\omega_q^2} \ln\left[\frac{\omega_q + \omega' - kq}{\omega_q + \omega' - kq}\right] \tag{7.10}$$

where $q = \sqrt{2\omega'}$ and $k = \sqrt{2\omega}$. Similarly

$$\begin{aligned} \hat{A}^{sat}_{inter}(\omega,\omega') &= \frac{\omega_p^2}{2\pi k'} \frac{1}{(A + q(\omega')^2/2)q(\omega')^2} \\ &\quad \times \ln\left|\frac{\omega' - q(\omega')^2/2 + k'q(\omega')}{\omega' - q(\omega')^2/2 - k'q(\omega')}\right| \theta(\omega' - \omega_p) \end{aligned} \tag{7.11}$$

where $k' = \sqrt{2(\omega - \omega')}$ and $q(\omega')$ is as defined in equation 7.4.

This interference results in a net shift of spectral weight away from the satellite and into the quasiparticle peak. At low energies, twice the spectral weight of $\hat{A}^{sat}_{inter}$ is roughly equal to the sum of the spectral weights of $\hat{A}_{intr}$ and $\hat{A}_{\text{extr}}$ and has a similar lineshape, as is shown in figure 7.1. This provides an approximate cancelation in this region. At higher energies, the interference term decreases. An intuitive understanding of this behavior can be gained by thinking of the interference arising from the mutual screening of the photoelectron and core hole. At close distances, the fields of these two oppositely charged particles roughly cancel each other, so the system response in terms of creating many body electronic excitations is greatly reduced. It is only at large distances that the full interaction of the excited particles with the medium is restored. At low energies, the photoelectron leaves slowly, so it remains close to the core hole for long periods of time, while at high photoelectron energies these two particles separate quickly. Thus, at low energies, we expect the interference to be maximal while in the limit of high energies the interference should vanish.

This behavior is reflected in our model. Near threshold, all of the satellite parts of the spectral density function have similar shapes and a weight equal to a, so that the

sum of the satellite contributions tend to cancel. Further, the quasiparticle weight $Z(\omega) \approx 1 - a$, while the interference contribution to the main peak $a(\omega) \approx a$. Thus, the weight of the quasiparticle becomes $\exp(-a)(1-a)(1+2a) \rightarrow 1 + \mathcal{O}(a^2)$. At high energies, the interference as given in equations 7.10 and 7.11 declines toward zero.

7.1 Practical difficulties

The effective spectral function has been separated into many terms. In the satellite region, two of the three terms are calculated from a direct second order expansion, while the other is calculated via a self energy representation. Problems arise because the interference term is subtracted from the other two. Since the approximations are not all the same, there is no guarantee that the interference will not over-cancel the intrinsic and extrinsic terms, leading to a region of net negative spectral density. A net spectral density is clearly unphysical; however, since the only physical effect of the spectral function occurs once it is integrated over, one might be led to think that small regions of negative spectral density are not a problem so long as the net satellite weight is not negative. This is true, so long as the regions of negative spectral density are small enough. However, even when the satellite has a net positive spectral weight, significant pathologies can occur when some regions in the satellite have significant negative spectral weight. This is because equation 8.2 is a convolution of the spectral function with a sinusoid. When the period between the main quasiparticle peak and the negative part of the satellite hits resonance with the sinusoid, it will lead to a net amplitude *increase*. This is even more serious when the negative part of the satellite occurs before the main satellite structure, because at certain energies $\omega \approx E_F + \omega_p$, the main positive parts of the satellite are cut off by the upper limit to the integration. This amplitude increase is quite unphysical. If care is not taken in constructing the spectral function, it is quite likely to find large amplitude increases just before the onset of plasmon losses.

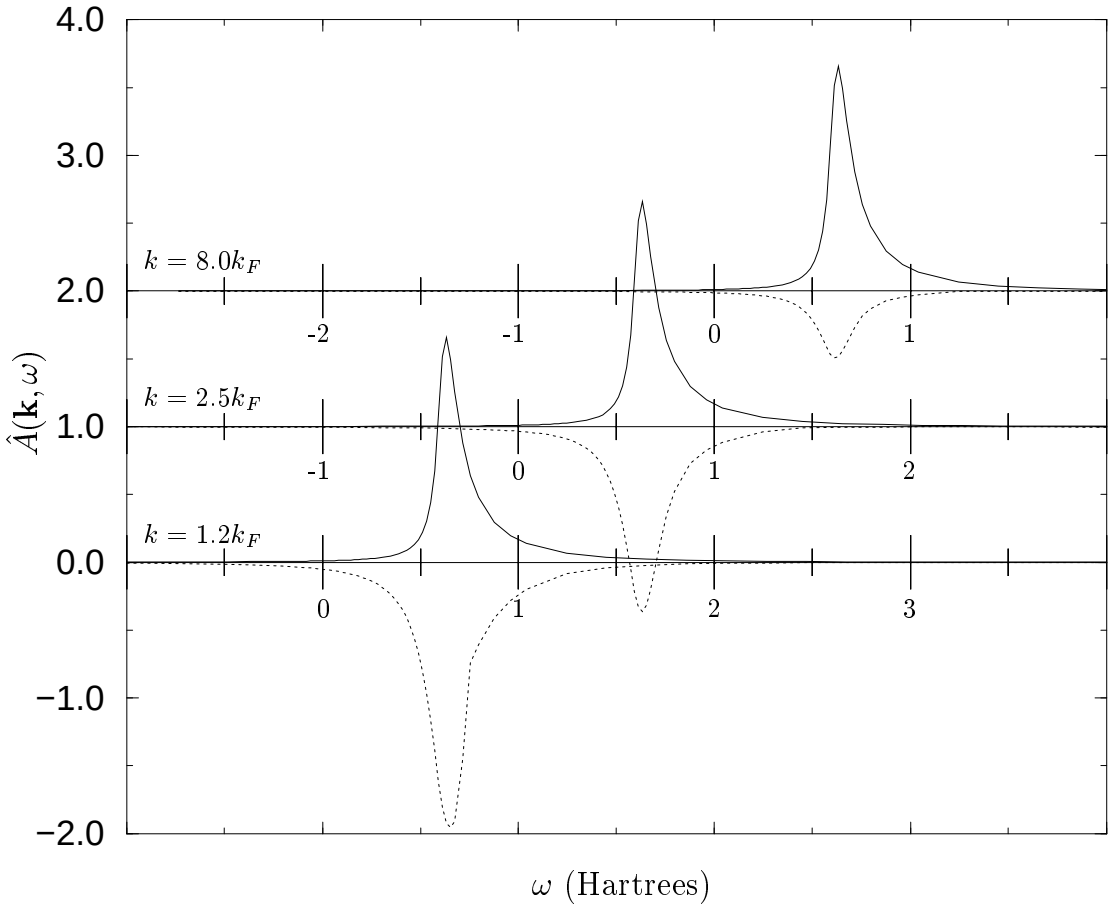

Figure 7.1: The intrinsic (solid) and interference (dots) satellite spectral functions for $r_s = 2$ at several values of momentum. The interference satellite shown is $-2\hat{A}_{inter}$. In order to avoid regions of significant negative spectral density and to avoid numerical instability, these spectral functions need to be broadened, and the interference contribution needs considerably more broadening than the intrinsic term. The intrinsic satellite has been broadened by $1/15\,\omega_p$, while the interference satellite has been broadened by $1/6\,\omega_p$.

There are a few tricks that can be used to reduce the possibility of this unphysical increase. The first is simply to apply more broadening to the satellite terms. The intrinsic and interference terms, in particular, have quite sharp features when equations 7.4 and 7.11 are used directly, and broadening helps to smooth out the features that can lead to over-cancelation. However, even large amounts of broadening are insufficient to completely suppress the problematic negative regions of the satellite. The reason is because the extrinsic satellite from the GW approximation peaks at energies significantly greater than ω_p beyond the quasiparticle, unlike the intrinsic and interference satellites. Since we know from photoemission that the extrinsic satellite should peak at ω_p beyond the quasiparticle, we find it is necessary to shift the extrinsic satellite spectral function to the left so that it coincides with the other two satellite spectral functions. With these two methods, the satellite region is left with only small regions of negative spectral density. While this small negative spectral density is not a problem over most of the absorption spectrum, there are small regions where it still leads to pathologies. Our final step to correct this is to simply set the satellite spectral function to zero wherever our equations tell us we have a negative spectral weight. We then renormalize the satellite spectral function so that the net satellite spectral weight is unchanged. With this last step, the convolution is quite well behaved.

At energies near the absorption edge, the extrinsic satellite exhibits significant satellite features at excitation energies lower than the quasiparticle. Because of our approximations that neglect many effects near the Fermi level, there are no corresponding features in the intrinsic or interference terms. As such, these low energy satellite features remain in the spectral function. Because cancelation should be large near threshold, and because the low energy satellites lead to significant effects on the spectrum that are not reproduced in the experimental data, that part of the self energy arising from contributions below the Fermi level, Σ_d^-, is set to zero. This removes the low energy satellites while leaving the high energy satellites unaffected.

A second unphysical feature that occurs in this model is a sharp structure located

at the onset of plasmon losses. This is due to the singularity at the plasmon pole in our model dielectric function, and can be traced to a singular point in the renormalization constant. Two ways around this are to use a more realistic dielectric function such as the Lindhard or RPA function; and to use a broadened plasmon pole. Even large amounts of plasmon broadening still leave a fairly sharp cusp in the renormalization constant, however, as is shown in figures 4.7 and 4.8.

In the next two chapters, we present the results obtained using these procedures for calculating the satellites, plus the extrinsic satellite found in Chapter 4, on the EXAFS and XANES spectroscopies, respectively.

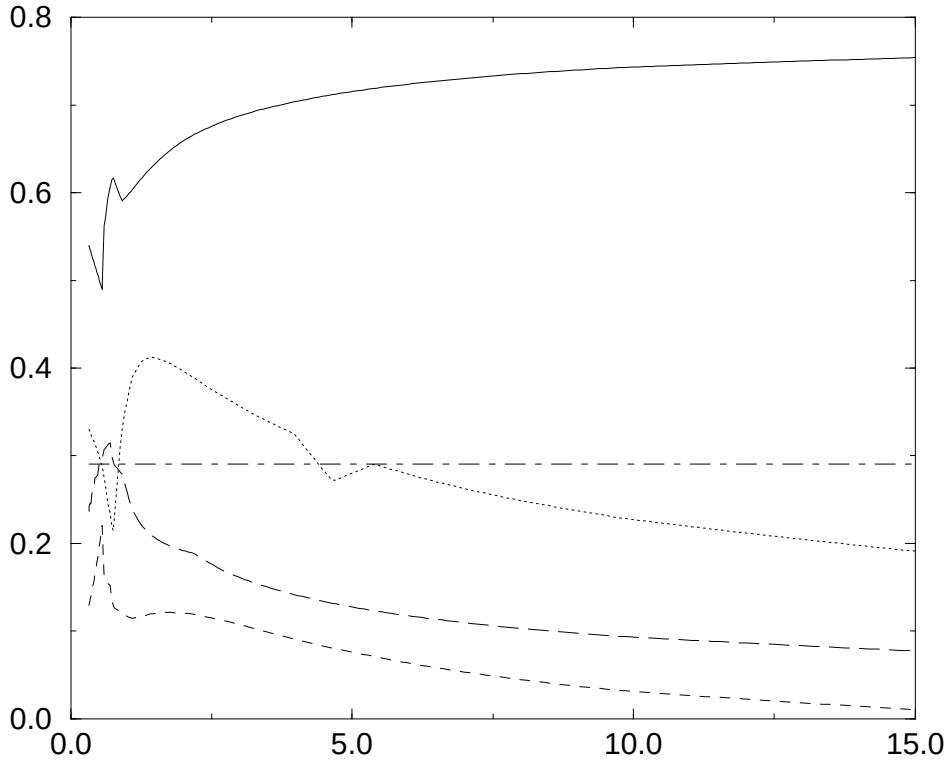

Figure 7.2: The spectral weights of the various contributions to the effective Green's function for the electron gas density of interstitial copper ($r_s = 1.8$) and a plasmon broadening of $0.1\omega_p$. In these curves, the anomalous region of the extrinsic satellite has been removed and added to the quasiparticle. The extrinsic quasiparticle contribution (solid) is dominant, but the interference quasiparticle weight $2a(\omega)$ (dots) has a significant contribution at low energies. The extrinsic satellite $\hat{A}_{extr}$ (short dashes) and the interference satellite $\hat{A}^{sat}_{inter}$ (long dashes) have a significant contribution at low energies, but quickly drop in importance with increasing intensities. Twice the weight shown for the interference satellite is subtracted from the total satellite. Because of the ambiguity about the anomalous region of the extrinsic satellite, the extrinsic satellite and quasiparticle weights are only approximate, although their sum is exact. The intrinsic satellite $\hat{A}_{inter}$ (dash-dots), however, is has a constant weight of $a\exp(-a)$, and the theory reduces to the sudden approximation. These weights have been multiplied by the quasiparticle weight $\mathrm{Re}\, Z_k$ for approximate normalization, but because this terms are from a second order expansion in the potentials, normalization is not guarenteed and they only sum to one with an error on the order of $a^2 \approx 0.07$.

Chapter 8

MANY BODY EFFECTS ON THE EXAFS SPECTRUM

In this chapter, we expand on the main result of chapter 5, Eq. 5.44, to consider the effect this has on the EXAFS spectrum. We show how the many body amplitude reduction can be given by a phasor sum over the spectral function. Finally, we test our theory on two materials, copper and titanium.

It seems prudent to re-iterate here the point of Eq. 5.41; the quantity μ_{qp} that appears in equation 5.44 differs by a complex constant $Z(\omega)\exp(-a)$ from the absorption calculated in the single particle approximation with the mean free path and on-shell energy shift included. The complex nature of $Z(\omega)$ can be included as a phase shift added to the central cell phase shift, the magnitude of $Z(\omega)$ simply reduces the overall magnitude of μ. As discussed, all many body effects can be included (under certain approximations) by representing the absorption via equation 5.44. This means that all of our well tested techniques for calculating the single particle XAS can be used for the starting point for our calculations.

In fact, we start with the familiar trick of separating the quasiparticle absorption into an embedded central atom component and a term from scattering off neighboring atoms $\mu_{qp}(\omega) = \mu^0_{qp}(\omega)[1 + \chi_{qp}(\omega)]$. We then have

$$\begin{aligned} \mu_0(\omega) &= \int d\omega' \hat{A}_{\text{eff}}(\omega, \omega')\mu^0_{qp}(\omega - \omega') \\ &\approx \mu^0_{qp}(\omega) \int_{-\infty}^{\omega - E_F} d\omega' \hat{A}_{\text{eff}}(\omega, \omega'). \end{aligned} \tag{8.1}$$

In the second step, we neglect the variation of μ^0_{qp}. Since μ^0 is usual a smooth function past the edge with little variation over the energy scale of a few ω_p, this is usually a good approximation. However, the presence of sharp atomic resonances may lead to

many body features present in the background. With this approximation, the EXAFS spectrum becomes

$$\chi(\omega) \approx \int_{-\infty}^{\omega - E_F} d\omega' \tilde{A}_{\text{eff}}(\omega, \omega') \chi_{qp}(\omega - \omega'). \tag{8.2}$$

where $\tilde{A}_{\text{eff}}$ is the effective spectral function normalized over the range of integration

$$\tilde{A}_{\text{eff}}(\omega) = \hat{A}_{\text{eff}}(\omega)/N(\omega) \tag{8.3}$$

$$N(\omega) = \int_{-\infty}^{w - E_F} d\omega' \hat{A}_{\text{eff}}(\omega, \omega'). \tag{8.4}$$

From equation 2.18, we see that the EXAFS signal for a given scattering path of length R is a sinusoidal function. If we treat the fine structure as an analytic function of ω, we have $\chi(\omega) \propto \exp 2ik(\omega)R$ for an EXAFS wave number $k = \sqrt{2(\omega - E_F)}$. The convolution of this $\chi(\omega)$ with any normalized, positive definite density function $\tilde{A}_{\text{eff}}(\omega, \omega')$ gives a phasor sum where the satellite part shifts the energy argument in χ by the excitation energy ω'. This introduces both an amplitude reduction and a phase shift to the original χ. In our notation, the constant amplitude reduction factor S_0^2 from the single electron theory is replaced by an energy dependent complex amplitude factor $S_0^2(\omega)$, given by

$$S_0^2(\omega) = \int_{-\infty}^{\omega - E_F} \tilde{A}_{\text{eff}}(\omega, \omega') e^{2i[k(\omega - \omega') - k(\omega)]R} \tag{8.5}$$

The qualitative behavior of S_0^2 is now apparent. At low energies, the satellite terms largely cancel and $\tilde{A}(\omega, \omega') \rightarrow \delta(\omega')$. Thus, $S_0^2 \rightarrow 1$. At high energies, $\tilde{A}_{\text{eff}} \rightarrow \tilde{A}_{qp} + \tilde{A}_{\text{intr}}$. However, $\tilde{A}_{\text{intr}}$ contains all of its weight within a few multiples of ω_p of the quasiparticle, so that the phase difference $2[k(\omega - \omega') - k(\omega)]R$ becomes small, and once again $S_0^2 \rightarrow 1$. It is at intermediate energies where the magnitude of S_0^2 goes through a minimum. The many body phase shift will give a small phase ϕ_{mb} to the sinusoidal EXAFS signal $\exp[2ikR + \phi_{mb}(k)$. As a consequence, if $\phi_{mb}(k)$ has a non-zero overall slope it will give a correction to the experimentally determined distances of the scattering paths.

We choose to compare our theory with experiments on two metals, copper and titanium. Reliable experimental data exists for both. Copper is chosen because the errors in the MS path expansion are quite small, and thus it has formed a useful test case for nearly every new advance in XAS theory. Here, that tradition is continued with an analysis of the S_0^2 and other many body effects. Titanium has a relatively large S_0^2, so it can act as a fairly extreme case on which to test our model. The results are shown in figures 8.2 and 8.3. The amplitude of the Fourier transformed theory with and without the many body convolution is shown. The phase shift turns out to be small enough that its correction to the scattering lengths is within the experimental error, and thus this correction is not shown.

The effect of the many body convolution on the EXAFS spectra is to bring the theoretical amplitude down to within a few percent of the experimentally measured values on both of the cases that we examined. Interestingly, in both of these cases, the amplitudes were consistently overestimated by a small amount. This may be due to an incorrect estimate of the quasiparticle losses employed in the single particle EXAFS calculations. If this agreement with experiment is typical of the results that can be expected, this method should eliminate the adjustable amplitude parameter in EXAFS theory. In the next chapter, we shift our attention from the extended fine structure to the near edge x-ray spectra.

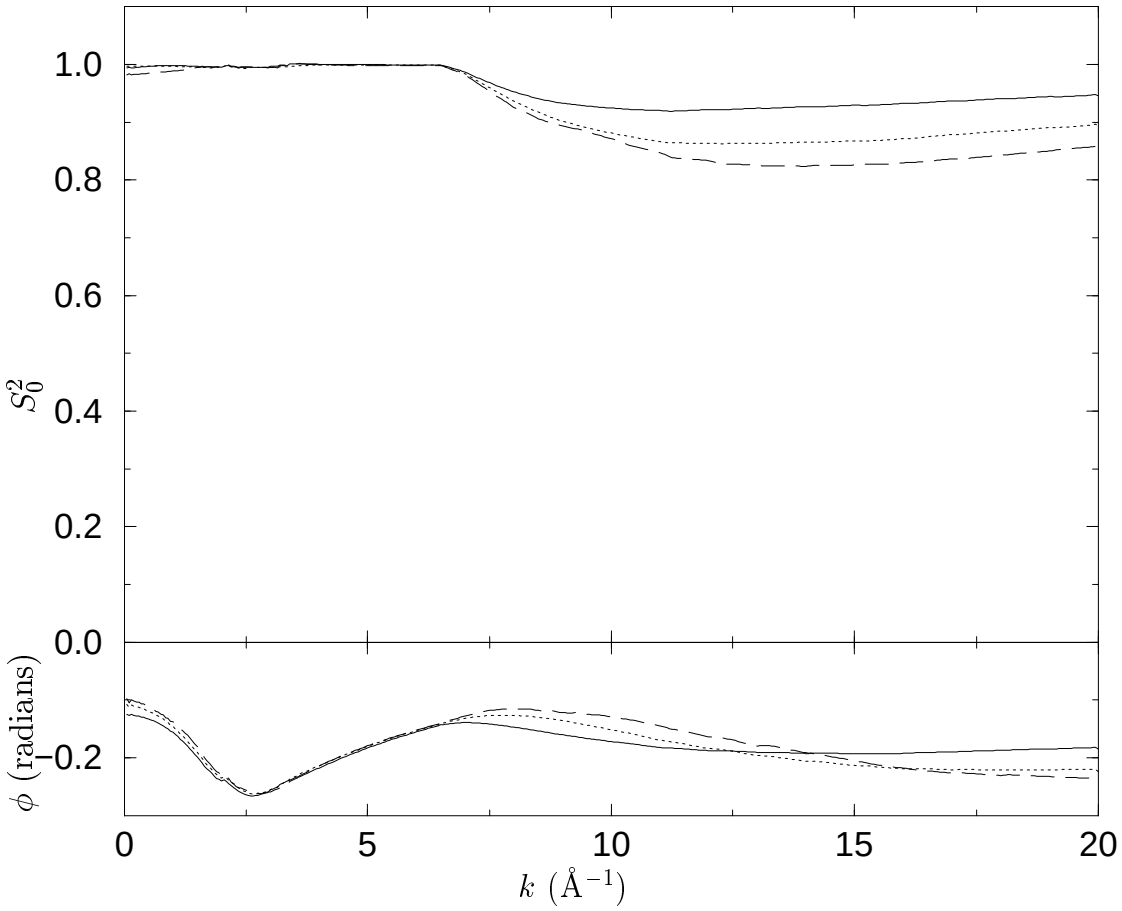

Figure 8.1: The many body amplitide reduction (S_0^2) and many body phase correction ϕ to the EXAFS shown for the nearest neighbor single scattering path (solid), the second nearest neighbor single scattering path (dots), and a triangular scattering path (dashes) in the EXAFS expansion in copper.

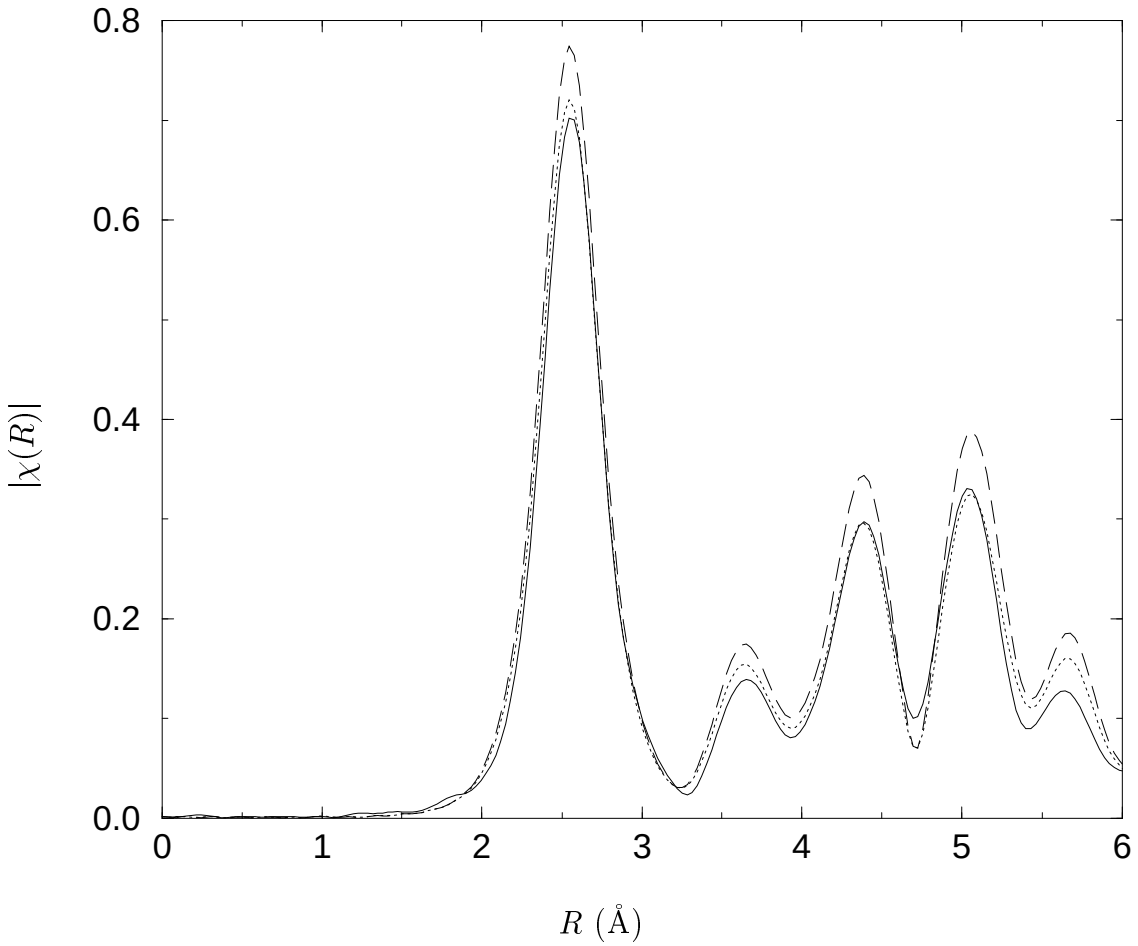

Figure 8.2: The Fourier transformed EXAFS spectrum $\chi(R)$ for copper at 10 Kelvin. The single electron theory (dashes) overestimates the experimental results (solid) everywhere. The many body theory (dots) reduces the amplitude to within a few percent of the experimental values.

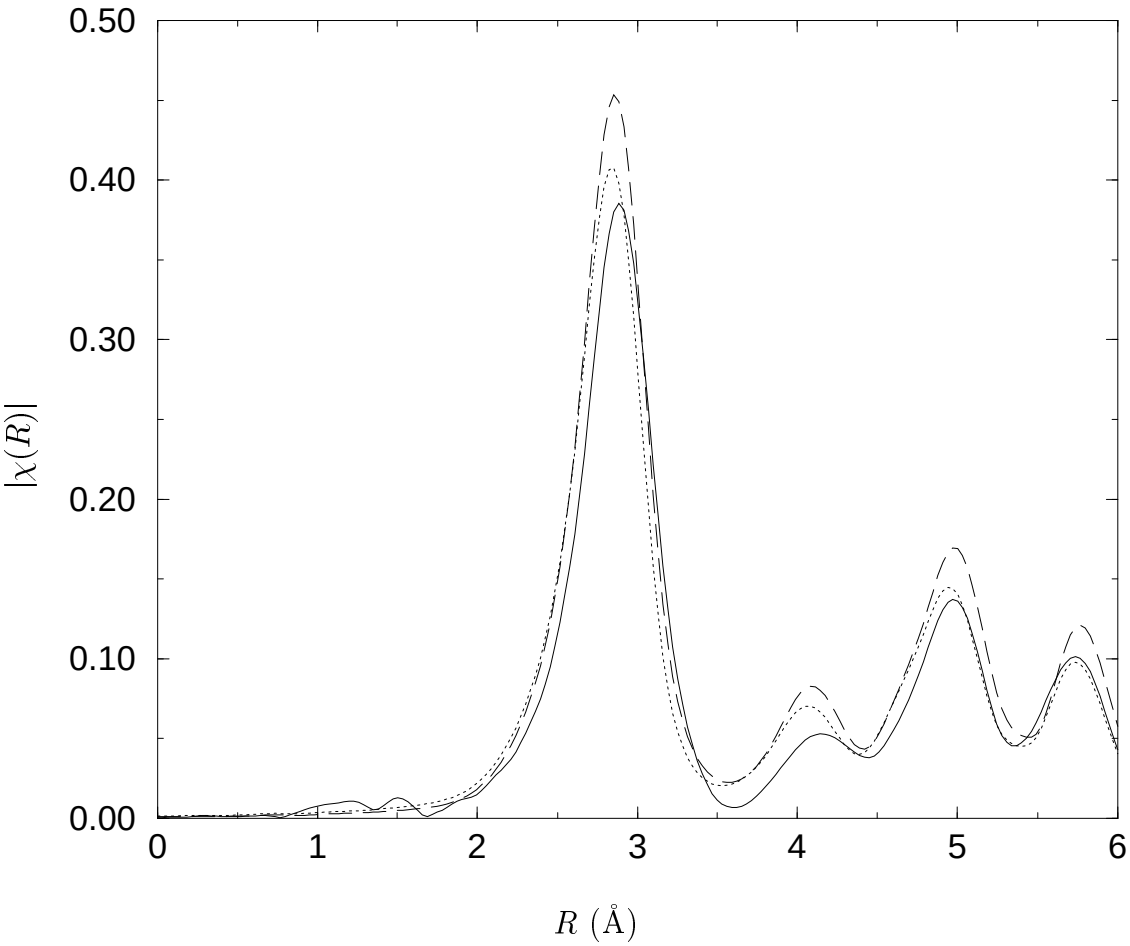

Figure 8.3: The Fourier transformed EXAFS spectrum $\chi(R)$ for titanium at 20 Kelvin. The single electron theory (dashes) overestimates the experimental results (solid) everywhere. The many body theory (dots) reduces the amplitude to within a few percent of the experimental values.

Chapter 9

MANY BODY EFFECTS ON THE XANES SPECTRUM

In this chapter, we consider the consequences of the main result of chapter 5, Eq. 5.44, on the near edge region of x-ray absorption spectra. We predict several features which may be observed, and show evidence of one of these features in the XANES spectrum of copper. We also apply our theory to titanium and compare with experiment.

In the XANES region, the approximation we employ in equation 8.1 is no longer suitable. Instead, we take $\mu(\omega)$ directly from equation 5.44,

$$\mu(\omega) = \int d\omega' \hat{A}_{\text{eff}}(\omega, \omega - \omega')\mu_{qp}(\omega'). \tag{9.1}$$

What we have available to us, however, is not the quasiparticle spectrum μ_{qp} but the one electron spectrum from our XAS codes $\mu^{(1)}$, which differs from μ_{qp} by an amplitude $\exp(a)/|Z(\omega)|$ and a many body phase ϕ. The amplitude can be dealt with simply by multiplying by the appropriate factor. However, the single particle spectrum is given as a real valued function, and to reproduce the many body phase we need to treat our absorption spectrum as a complex quantity. From equation 2.7, we can represent the complex absorption cross section as

$$\sigma(E) = \frac{4\pi i\omega}{c} \sum_i |\langle i|\Delta_\varepsilon^\dagger G(\omega + E_i)\Delta_\varepsilon|i\rangle|\theta(\omega + E_i - \mu_F). \tag{9.2}$$

We represent the matrix elements $|\langle i|\Delta_\varepsilon^\dagger G(\omega + E_i)\Delta_\varepsilon|i\rangle|$ as analytic quantities. If we then assume that the background absorption μ_0 varies slowly, then the quantity $\mu - \mu_0$ corrects for the edge jump due to the step function in equation 9.2 and we can approximate the imaginary part of a complex μ as the Hilbert transform of the

known real part of μ with the background subtracted

$$\mathrm{Im}\,\mu(\omega) = -\frac{1}{\pi} P \int d\omega' \frac{\mathrm{Re}\,\mu(\omega') - \mathrm{Re}\,\mu_0(\omega')}{\omega' - \omega} \tag{9.3}$$

with the understanding that this will not be accurate immediately near the edge, but will give the correct phase shift within an EXAFS oscillation or two of the edge. With this complex μ, we can now perform the convolution in equation 9.1.

This convolution should not be performed on its own, as the many body corrections to the dipole matrix elements are also of importance near the edge. As a consequence, one should first calculate the edge singularity effects from Chapter 6 and find the "single particle" spectrum with these modified matrix elements before carrying out the convolution. The convolution tends to lead to an edge reduction, partially canceling the edge increase due to the projection operator acting in the dipole matrix elements.

A qualitative understanding of some many body effects may be gained by examining what occurs when we convolute different edge structures with our many body spectral function. For the purpose of this rough explanation, the quasiparticle contribution to $\hat{A}_{\mathrm{eff}}$ will be considered a delta function with weight $Z(\omega)$ located at $\omega' = 0$. The satellite contribution will be approximated as a sharp localized feature occurring at energies close to $\omega' = \omega_p$ with weight $1 - Z(\omega)$. When a strong white line occurs, the convolution will then reproduce the white line structure starting at an energy ω_p above the edge when the satellite part of the spectral function picks up the white line in the absorption spectrum. This white line "shadow" will be reduced in weight from the white line itself by a factor $1 - Z(\omega)$. Unfortunately, it will be difficult to verify this prediction, since the strongest white lines occur in the L_2 edges of the transition metals, and the white line shadow peak will be hopelessly obscured by the L_3 absorption edge.

A dark line can also lead to a similar shadow feature, in this case a region of lowered absorption which follows the dark line. Starting at an energy ω_p beyond the edge, the quasiparticle will give a reduced contribution to the convolution, while

the satellite is picking up very little weight since it is in the dark line region. Once the photon energy is high enough to bring the satellite beyond the dark line, the absorption climbs back up to approximately the level of the background. Since these dark lines occur for K-edge transitions, there is hope of finding experimental evidence for many body effects in the XANES region in the form of dips in the absorption edge not reflected in the single electron spectrum.

Pre-edge features also occur at K-edges. Just as described for the white lines, the pre-edge feature should have a shadow structure located about one plasma frequency above the edge. Because pre-edge features are often very sharp, we stand a reasonable hope of getting a small but recognizable peak in the absorption spectrum. Unfortunately, pre-edge features are also often quite small. Whether this will overcome the sharpness of the feature and obscure any many body effects will be investigated later.

After all this, however, it is necessary to point out that our spectral function has been derived from a model that made several approximations that are not justified near the Fermi level. At this point, our theory can only suggest many body effects near the edge, it cannot be expected to accurately reproduce them. It may be that our approximations work well as close as ω_p to the edge, but this can only be confirmed by comparison with experiments. In the two cases explored in this dissertation, copper and titanium, the edge structure of copper is markedly improved by our procedures, while that of titanium is virutally unaffected. A description of the computer codes used to find the many body effects in both the EXAFS and XANES regions will be described in the next chapter.

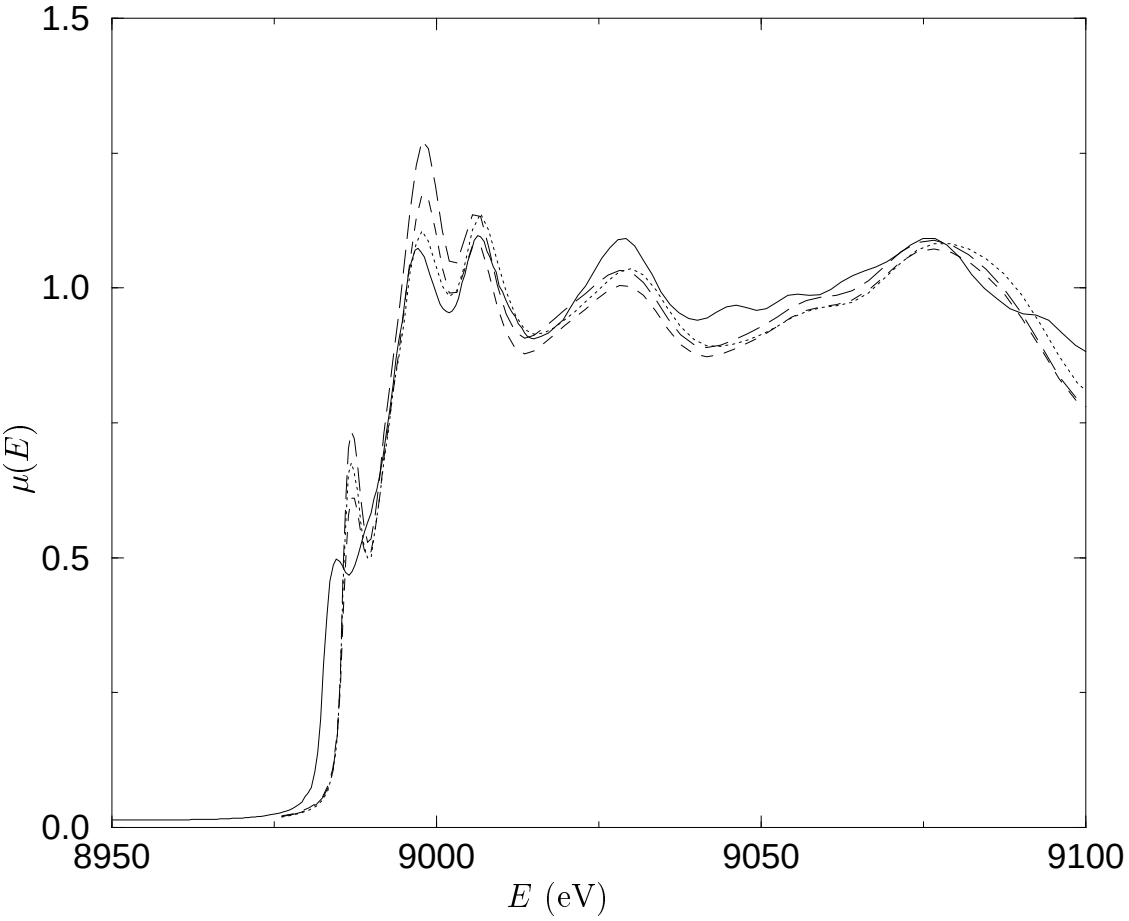

Figure 9.1: The XANES spectrum of copper at 10 Kelvin. In the experiment (solid) the first two peaks are of nearly equal height. The single particle theory (short dashes) overestimates the height of the first peak. The edge enhancement from the projected dipole matrix elements (long dashes) increases this overestimation. The convolution with the many body spectral function (dots) reduces the amplitude of the first peak, and this full many body spectrum more closely coincides with the experimental result. Copper is a material with a dark line, this reduction of intensity near the edge can be seen as evidence for many body effects in the XANES region.

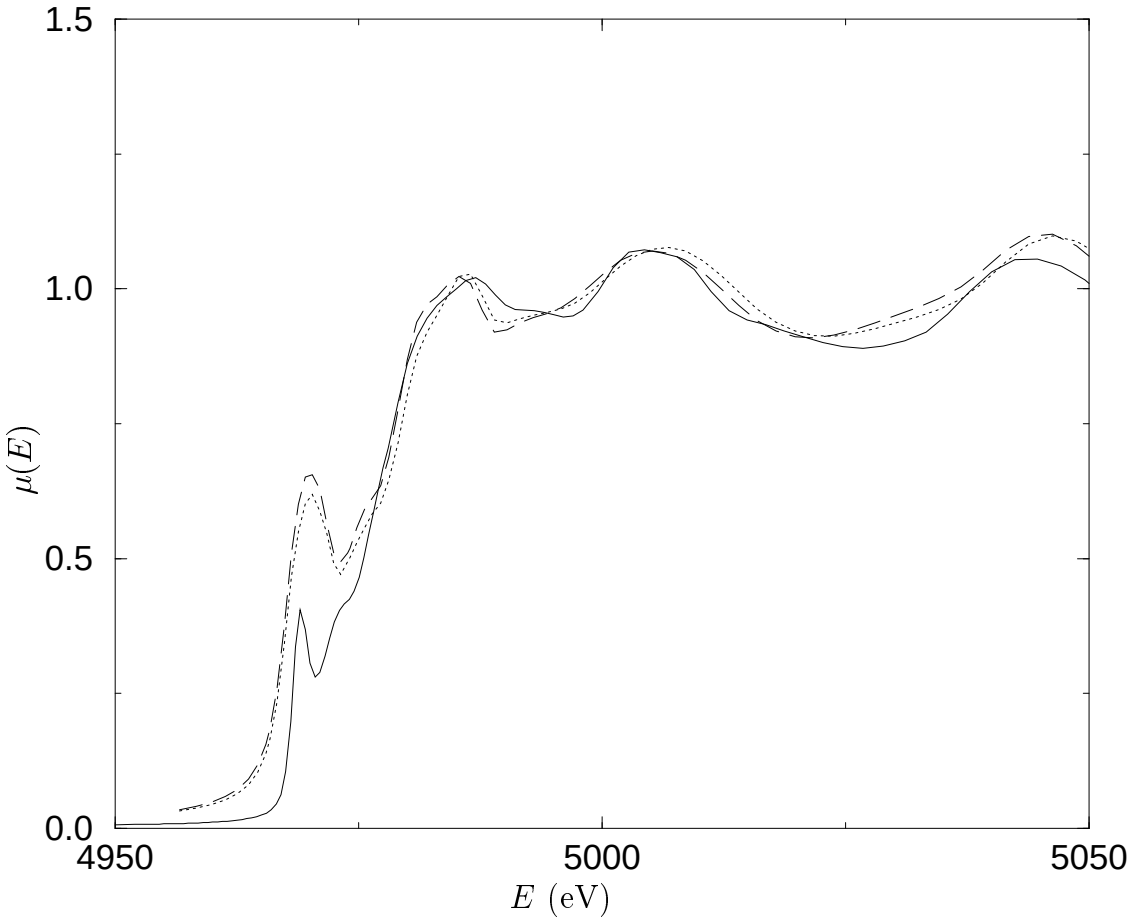

Figure 9.2: The XANES spectrum of titanium at 20 Kelvin. As expected from figure 6.3, these is essentially no effect from the projection operator and the single particle spectrum essentially lies on top of the spectrum computed with projected matrix elements (dashes) and thus is not shown for the sake of clarity. Despite the strong pre-edge feature, the convolution with the many body spectral function (dots) has little effect. In particular, there is no appreciable change to the spectrum at an energy $\omega_p = 17$eV from the pre-edge feature. The experiment is shown as a solid line.

Chapter 10

CODE FOR THE CALCULATION OF MANY BODY EFFECTS

Two computer programs were written for this project. In order to calculate the many body spectral function and perform convolutions with the single electron XAS spectra, the code SO2CONV was written. To calculate edge singularity effects based on the projection operator in the dipole matrix elements, the code EDGEC was developed.

10.1 so2conv

The computer code SO2CONV was written to calculate the full many body spectral function and convolute the output of the single electron *ab initio* XAS program FEFF with this spectral function to get the many body x-ray absorption spectrum. SO2CONV is programmed in FORTRAN77 for easy portability to other platforms.

10.1.1 Input and Output

SO2CONV requires as its input at least one of the XAS output files from FEFF, either xmu.dat, chi.dat, or one or more of the chipNNNN.dat or feffNNNN.dat files. From these files, SO2CONV.F determines important physical parameters about the system and, when applicable, about the scattering path under consideration. These files also provide the XAS spectrum that will be convoluted. The FEFF XAS files should not be renamed, since SO2CONV determines what type of data the file contains and the procedure for convoluting it based on the name of the file. If the XAS file is renamed, those listing the EXAFS signal χ should contain the text string "chi" in their name,

those listing the absorption μ should contain the text string "mu", and those listing the effective backscattering amplitude should contain the text string "feff".

One further file is required as input. This is a file titled so2conv.inp. The only required information in so2conv.inp is a line that says only FILES, followed by a list of the FEFF output files to be read and processed. The word FILES must be in capital letters. Each output file must be on its own separate line. After the FILES card, every line must be either blank, a comment line (designated by a hash symbol (#) in the first column), or contain the name of a file. SO2CONV will read and process each file listed in the input file independently.

There are other, optional cards that can be placed before the FILES card. Most of these are for diagnostic and testing purposes, and can probably be ignored by the average user. Nevertheless, in the event that someone may find them useful, I will describe the extra cards here. All card must be typed in capital letters.

SAT isat This card tells SO2CONV what approximation to use for the extrinsic satellite. The argument isat is an integer, whose meanings are as follows:

0 The deconvoluted GW extrinsic satellite, from equation 4.70

1 The cumulant expansion of the satellite: $A_{extr}(\omega,\omega') = (1/\pi)|\mathrm{Im}\,\Sigma(\omega,\omega') - \mathrm{Im}\,\Sigma(\omega,0) - \omega'(\partial/\partial\omega')\Sigma(\omega,0)|$

2 The fully broadened GW extrinsic spectral function with the quasiparticle hole subtracted off.

The default is SAT 0, and is recommended. The cumulant expansion gives similar results, but has not been rigorously tested. The satellite based on the fully broadened GW spectral function has, in the cases it was tested on, given S_0^2 significantly smaller than experiment.

WGRID igrid The name of this card stands for write grid point. Its argument igrid is an integer between 1 and 66. On the igrid'th call to the subroutine MKSPECTF,

the spectral function will be written to the files satsf.dat, which contains the satellite contributions, and the file qpsf.dat, which contains the quasiparticle lineshape and an attempt to separate the anomalous region of the extrinsic satellite from the rest of the satellite. If forces the main program to call MKSPECTF on the first file, and will only write the spectral function for the first file.

WPOINT ipoint The name of this card stands for write data point. Its argument ipoint is a positive integer argument equal to or less than the number of lines of data in the first FEFF XAS data file read. The argument specifies the data point from the FEFF XAS file for which a spectral function will be written. The spectral function is written as a function of excitation energy for the momentum of the specified data point. It will write the spectral function for the first FEFF XAS file only. The spectral function files are the same as those written when the WGRID card is called. If both WPOINT and WGRID are specified, WGRID takes precedence and the spectral function is written for a grid point rather than a data point.

WCONV iconv ifile This card will tell the program to write a running log of the convolution for the data point number iconv from the file number ifile from the list of XAS files. As the integration of the convolution proceeds through each grid point, the functions being convoluted and the integrated value up to that point are written. Examining this output can help in understanding where a particular feature comes from, and what is responsible. The file realint.dat is written for the convolution of the real part of the XAS spectrum, and the file imagint.dat is written for the convolution of the imaginary part of the spectrum.

WEIGHTS If this card is present, a file named weights.dat of the spectral weights of the quasiparticle and satellite terms from the extrinsic, intrinsic and interference parts of the spectral function will be written. The weights file will be written for the first FEFF XAS file read, if the spectral function is recomputed during the execution

of the program, the weights file will not be re-written.

WEIGHTSCL This card's name stands for clipped weights, and it does the same thing as WEIGHTS, except that the weights it writes are for a method of removing the anomalous structure from the extrinsic satellite weight and putting it in the quasiparticle weight. It writes to a file named weightscl.dat

SE This card's name is an abbreviation for self energies. If present, SO2CONV will write a file named selfenergy.dat containing the real and imaginary parts of the on shell self energy and their derivatives as a function of energy. The self energy file will be written for the first FEFF XAS file read, if the spectral function is recomputed during the execution of the program, the file will not be re-written. The self energies written are E_k^1 (equation 4.48), Γ_k^1, and Z_k^1, note that these are not the corrected quasiparticle energies and widths. If desired, the quasiparticle energies can easily be calculated from these quantities from the definitions given after equation 4.52.

There are no other cards at this time.

For every FEFF XAS file read, a file of the same name but appended with the letter "c" before the .dat extension ("c" for convoluted) will be written containing the many body XAS spectrum. For example, the output of SO2CONV running on xmu.dat would be xmuc.dat, while if SO2CONV runs on the file feff0003.dat, it would output a file feff0003c.dat. These output files have the same header and format as their respective FEFF XAS files they were convoluted from.

In addition, if a chi.dat or chipNNNN.dat file is convoluted, a file is written containing the amplitude reduction and many body phase shift. The name of this file is the same as the name of the FEFF chi file, but with the text string "so2" appended to the file name before the .dat extension. The *so2.dat files contain three columns:

1. EXAFS wavenumber k.

2. Many body amplitude reduction S_0^2.

3. Many body phase shift.

These files also contain the same header as the XAS input file they correspond to.

The entire spectral function for every momentum and energy grid point is stored in a binary file named specfunct.dat. In addition, the spectral weights, self energies, renormalization constant, bare electron and quasiparticle energies, material parameters, and the energy and momentum values at each grid point are also stored in this file. If this file exists, and SO2CONV is running on a XAS file that requires the same spectral function, the program can skip the time consuming evaluation of the spectral function.

The diagnostic file qpsf.dat is used to write the spectral functions of the quasiparticle terms when the cards WGRID or WPOINT are specified. It contains five columns:

1. Excitation energy ω'.

2. Line shape of the extrinsic quasiparticle.

3. Line shape of the interference quasiparticle.

4. Anomalous part the extrinsic satellite spectral function.

5. Remainder of the extrinsic satellite after the anomalous region has been removed.

The diagnostic file satsf.dat lists the spectral functions of the satellite terms when the cards WGRID or WPOINT are specified. It contains five columns:

1. Excitation energy ω'.

2. Extrinsic spectral function.

3. Interference spectral function.

4. Intrinsic spectral function.

5. Total satellite spectral function, the sum of the extrinsic and intrinsic terms minus twice the interference.

The diagnostic files weights.dat and weightscl.dat contain the spectral weights of the components of the spectral functions. They both have six columns:

1. Energy ω.

2. Weight of the extrinsic quasiparticle. In the file weightscl.dat, the spectral weight of the anomalous part of the extrinsic satellite is added to the quasiparticle weight.

3. Weight of the interference quasiparticle.

4. Spectral weight of the extrinsic satellite. In the file weightscl.dat, the spectral weight of the anomalous part of the extrinsic satellite is removed from the satellite weight.

5. Spectral weight of the interference satellite.

6. Spectral weight of the intrinsic satellite.

The diagnostic file selfenergy.dat is used to output information on the on-shell self energy. contains five columns:

1. Energy ω.

2. Real part of the on shell self energy.

3. Imaginary part of the on shell self energy.

4. Real part of the renormalization constant.

5. Imaginary part of the renormalization constant.

A modified form of SO2CONV has been developed to act as a subroutine in FEFF. In this form, SO2CONV does not need the so2conv.inp file, but it requires the feff.inp input file for FEFF and the list.dat FEFF output file. No diagnostic files will be written. The files xmu.dat, chi.dat, chipNNNN.dat and feffNNNN.dat are overwritten by the files containing the many body convolution, so no *c.dat or *so2.dat files are output.

10.1.2 Program structure and subroutines

The main program so2conv reads the input files, does some preprocessing, and then calls the subroutines that generate the spectral function and convolute the spectral function with the data. Figure 10.1 shows the structure of the program, with arrows indicating which subprograms each component of the program calls.

Subroutines

MKRMU The absorption spectrum μ from the file xmu.dat is real valued. In order to get a phase shift, we need to convolute with a complex function. Thus, μ treated as the imaginary part of a complex valued analytic function, and is put through a Kramers-Kronig transform to find the real part. MKRMU performs this transform.

MKSPECTF This subroutine is really the heart of the program. It is what generates the spectral function. It also broadens the self energies for a broadened plasmon model.

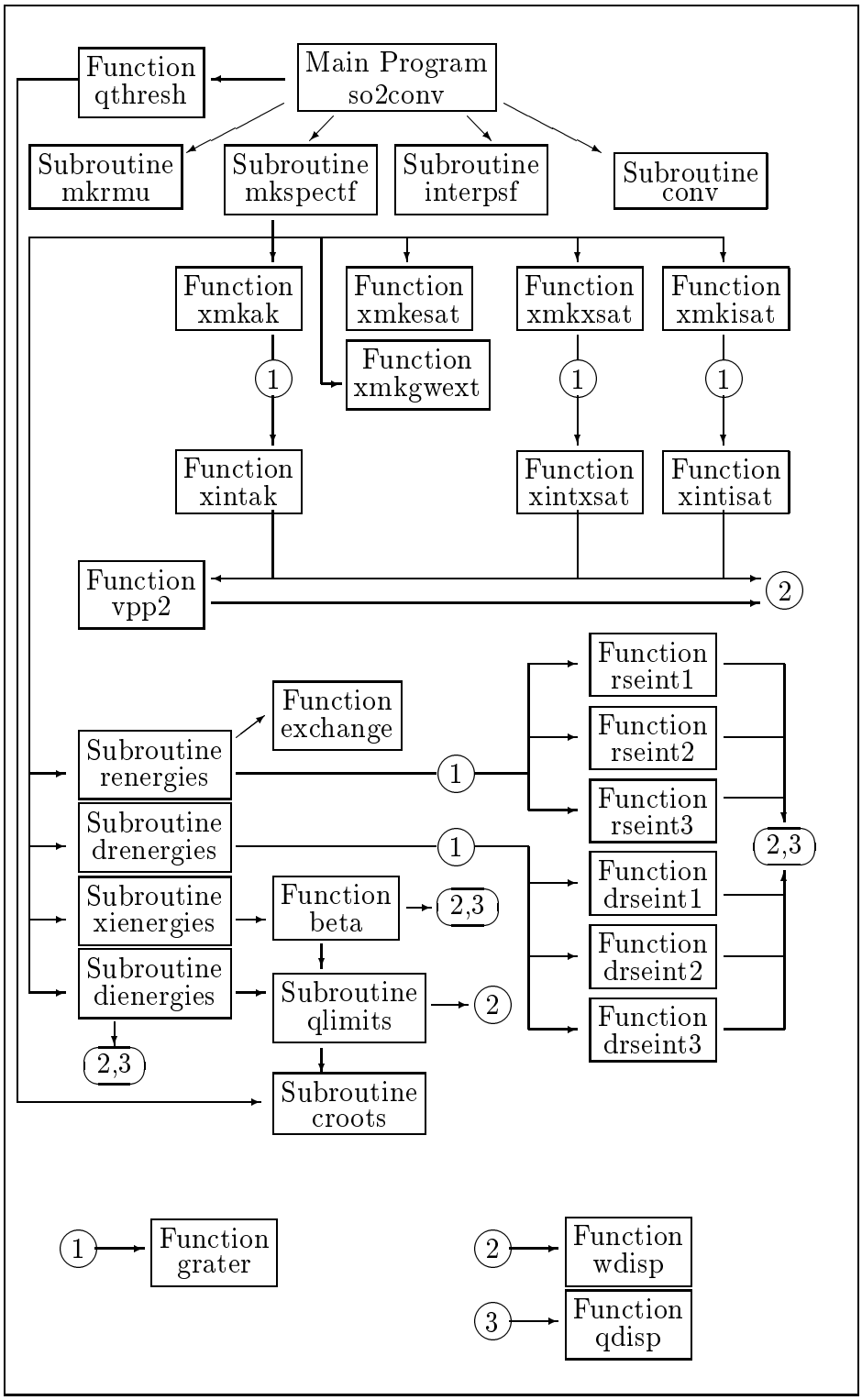

Figure 10.1: The structure of the program SO2CONV. An arrow passing through the number one indicates that the function referenced is integrated by the function grater.

INTERPSF The subroutine MKSPECTF outputs the spectral function on an energy grid whose points are chosen to represent all the necessary detail with the minimum number of grid points. INTERPSF interpolates the spectral function onto a uniform grid for the convolution subroutine.

CONV This convolutes the XAS signal with the spectral function. In the process, it creates the truncated, normalized spectral function $\tilde{A}_{\text{eff}}$ from equation 8.3 from the spectral function it takes as input.

RENERGIES Calculates the real part of the plasmon pole self energy.

XIENERGIES Calculates the imaginary part of the plasmon pole self energy.

DRENERGIES Calculates the real part of the derivative of the plasmon pole self energy with respect to the excitation energy.

DIENERGIES Calculates the imaginary part of the derivative of the plasmon pole self energy with respect to the excitation energy.

D2RENERGIES Calculates the real part of the second derivative of the plasmon pole self energy with respect to the excitation energy. Although this subroutine is not currently used in the program, if anyone ever needs an analytical calculation of this quantity, here is the code for it.

D2IENERGIES Calculates the imaginary part of the second derivative of the plasmon pole self energy with respect to the excitation energy. Like D2RENERGIES, this subroutine is not currently called in the execution of the program.

QLIMITS Finds the momentum limits $\tilde{q}_1$, $\tilde{q}_2$, q_3 as the solutions to equation 4.32.

CROOTS Returns the roots of a cubic polynomial.

Functions

XMKAK Integrates the function XINTAK to find the weight of the interference quasiparticle contribution $a(\omega)$ (equation 7.8).

XINTAK The integrand of the weight of the interference quasiparticle contribution $a(\omega)$.

XMKESAT Finds the deconvoluted extrinsic satellite $\hat{A}_{\text{extr}}$ from equation 4.70 at a given energy and momentum.

XMKGWEXT Finds the full GW extrinsic spectral function at a given energy and momentum.

XMKXSAT Finds the interference satellite function $\hat{A}^{sat}_{inter}$ from equation 7.9 at a given energy and momentum. In order to add broadening, it actually performs the integration rather than calculating equation 7.11 analytically.

XINTXSAT The integrand of XMKXSAT.

XMKISAT Finds the intrinsic satellite function $\hat{A}_{intr}$ from equation 7.3 at a given energy and momentum. In order to add broadening, it actually performs the integration rather than calculating equation 7.4 analytically.

XINTISAT The integrand of XMKISAT.

VPP2 The square of the plasmon pole coupling potential $|V_0^{\mathbf{q}}|^2$ from equation 4.21.

EXCHANGE The Hartree-Fock exchange potential Σ_{ex} from equation 4.6.

RSEINT*,DRSEINT* Here, * represents either 1, 2, or 3. These are the integrands of the self energy (RSEINT*) or the derivative of the self energy (DRSEINT*) from equations 4.41 and 4.42 or 4.55.

BETA The beta function $\beta = -|\mathrm{Im}\,\Sigma|/\pi$, used to find the imaginary part of the self energy.

GRATER Mike Teter's integration function, rewritten by Steve White and modified by John J. Rehr. This is the workhorse for integration in SO2CONV.

WDISP The plasmon dispersion relationship $\omega(\mathbf{q})$.

QDISP The inverse plasmon dispersion relation $q(\omega)$.

10.2 edgec

The computer code EDGEC takes the dipole matrix elements from the FEFF output files phase.bin and xsect.bin and computes the effects of the projection operator on these matrix elements. EDGEC is programmed in FORTRAN77 for portability to many different computing platforms. In order to avoid true singularities, broadening is added through a complex part of the momentum and through the use of a Fermi occupation factor in the momentum cutoff. Although the latter is temperature dependent, the final output is largely insensitive to either method of broadening.

10.2.1 input and output

The only input files for EDGEC are the files phasef.bin and xsectf.bin from a FEFF run for the material with a core hole, and the files phasei.bin and xsecti.bin for the same material calculated with the NOHOLE card in the feff.inp control file to force calculations for the material lacking a core hole potential.

The main output files from EDGEC are named phase.bin and xsect.bin. These are designed to replace the FEFF files of the same name in all calculations using FEFF modules 3 through 6.

10.2.2 program structure and subroutines

The program EDGEC is written as a subroutine which can be put into the FEFF code. At this time, however, FEFF only calculates the dipole matrix elements for either the state with the core hole present or the core hole absent, but not both. Since it would not be trivial to change the architecture of the FEFF code to do this, at this time the EDGEC subroutine is called by an outer main program TESTEDGEC which reads the input files and passes the relevant data to EDGEC.

subroutines

In addition to EDGEC, the following subroutines are called during the normal execution of this program:

RDNORM This subroutine reads the file xsecti.bin or xsectf.bin in order to extract the normalization for the dipole matrix elements in phase.bin. If EDGEC is incorporated into FEFF, this subroutine can be omitted as the FEFF program already has this information.

WRNORM This subroutine writes the file xsect.bin to be used in FEFF calculations. If EDGEC is incorporated into FEFF, this subroutine can be omitted as the FEFF program already has the code to do this.

RDXSPF and RDXSPI These are slightly modified forms of the FEFF subroutine RDXSPH to read the files phasei.bin and phasef.bin. They call on other subroutines and functions already present in FEFF.

WRXSPH This subroutine is taken directly from FEFF, and writes the file phase.bin.

functions

XINTPMR This is the real part of the integrand of the projection integral over states below the Fermi level.

XINTPMI This is the imaginary part of the integrand of the projection integral over states below the Fermi level.

FERMI This is a Fermi occupation function for a given temperature.

SENERGY This function interpolates between points from the self energy grid read from phase.bin to find the self energy at any given momentum.

XMATEL This function interpolates between points from the matrix elements read from phase.bin to find the matrix element at any given momentum and polarization.

GRATER Mike Teter's integration function, rewritten by Steve White and modified by John J. Rehr. This is the workhorse for integration in EDGEC.

Chapter 11

CONCLUSIONS

X-ray absorption spectroscopy has come a long way since its debut, and has been greatly aided by advances in theory. While a one particle quasiparticle approximation is useful for predicting a great many of the features observed in the x-ray absorption spectra, there are several many body parameters which, until now, were either neglected or were required to be fitted to the experimental data. Foremost among these is the EXAFS amplitude reduction, S_0^2 and an associated complex many body phase in the EXAFS. Without knowing S_0^2, the coordination number of the absorbing species cannot be experimentally determined with XAS. The amplitude reduction is fundamentally a many body effect. To model and predict it requires a knowledge of the inelastic losses and collective behavior of the condensed matter system. In particular, the interference between the extrinsic and intrinsic losses is significant in other systems (photoemission), suggesting its relevance to XAS.

In addition, there are potentially other many body effects which can be observed. Many authors have suggested that certain bumps in fine structure may be due to shake-up effects due to their proximity to the calculated shake-up lines. While such lines of argument are somewhat inconclusive, they cannot be discounted. There are also suggested edge enhancements or reductions which may be present. Finally, there is the question of how to treat the final state, with some materials better represented by a fully relaxed core hole in the final state and others without a core hole.

In this dissertation, we attempted to resolve some of these issues by developing a general theory of many body losses in the presence of both a core hole and a photoelectron, including interference between the two, based on a quasi-boson model.

The theory we develop is, in principle, capable of determining the EXAFS amplitude reduction while dealing with shake-up, edge singularities, and deviations from the final state rule. The main results of this theory are that the many body XAS can be represented as a convolution of the single electron XAS with a many body spectral function, where the single particle XAS is computed with dipole matrix elements which are modified by the presence of a projection operator. For this preliminary study, we have chosen to use an electron gas approximation. With this approximation, we leave the analysis of atomic-type shake-up effects for future investigators. However, we also come up with forms for the edge singularities and deviations from the final state rule, as well as methods of calculating the EXAFS amplitude reduction which was the primary motivation for this work and an associated many body phase shift to the EXAFS signal.

By considering the effect of plasmon excitations when applied to our general theory of losses, we suggest that there may be additional many body effects observable in XAS. In the presence of a dark line, we expect a reduction of intensity about one plasma frequency from the edge with a width comparable to that of the dark line. In the presence of a white line, an enhancement located one plasma frequency away may be seen instead. Other sharp features may also be observed "shadowed" by a peak about one plasma frequency from the location of the sharp feature.

In finding an expression for the extrinsic losses, we introduce a broadened plasmon pole model of the self energy. We use this to calculate the quasiparticle properties, including corrections to the width and energy due to the complex nature of the quasiparticle pole. The broadened plasmon reduces the unphysical effects of the plasmon singularity and introduces a small amount of losses into the region below the plasmon turn-on energy. However, this model can give unphysical values for the quasiparticle weight at high energies when plasmon broadenings are large, and it should thus be used with care when quasiparticle properties will influence the final result of a calculation.

To carry out these computations, several pieces of new code have been developed. The code SO2CONV will calculate the many body excitation spectrum and use this in a convolution with the single electron XAS to produce the many body XAS. Subroutines from SO2CONV can also be used to calculate the self energy and quasiparticle properties if needed for other applications. The code EDGEC will modify the single electron dipole matrix elements from FEFF to find multi-electron effects to these matrix elements due to the inclusion of an operator which projects onto unoccupied states.

In order to test our models, we applied them to the XAS of copper and titanium metals. The electron gas calculations were able to reproduce the amplitude of the Fourier transformed EXAFS of copper to within less than 2% on the main scattering peaks, compared to a 10% error from the one electron calculations. In titanium, the calculated many body amplitude is within about 5% of that of the experiment, compared to a 18% overestimation of the amplitude from the one electron calculations. If these results are typical, we can expect to pin the amplitude of the EXAFS signal to within a few percent, and thus eliminate the last remaining adjustable parameter in EXAFS theory.

In the XANES region, our model found an edge reduction in the copper spectrum, suggesting that these methods could be used to predict or explain some many body effects. No appreciable many body effects were noticed in the XANES of titanium despite the presence of small but sharp features which might be expected to show the satellite at about one plasma frequency from the edge, indicating that not every material will evidence many body effects from coupling to plasmons in the near edge absorption spectroscopies. More work needs to be done do determine the effect of dominant near edge structures such as white lines, although these are expected to show noticeable many body effects on the spectrum if not obscured by other features.

We have found that the edge singularity effects can lead to a significant edge enhancement in many cases. However, depending on the behavior of the dipole matrix

elements near the edge, there may not be a large effect. In copper, they lead to an edge enhancement, while in titanium they are practically unobservable. However, the edge effects cannot be taken alone, for the many body convolution can significantly alter the XANES signal, such that in copper there is actually a net edge reduction.

The research presented in this work represents a beginning in the calculations of inelastic losses. There is a lot of room for improvement. In particular, the following areas can immediately be identified as possible directions to take to extend the ideas presented here and improve upon these results:

- The expression for the effective Green's function is expanded to second order in the coupling potentials. This second order expansion leads to unphysical effects in some regions of the spectrum. Although these can be corrected by some rather *ad hoc* methods, a formulation which avoided these problems in the first place would be desirable. In particular, it will be promising to investigate grouping all loss effects together into the self energy. Such a formulation would give a positive normalized spectral function everywhere, thus avoiding many of the computational problems we encountered.

- A more realistic dielectric function could be employed. Within the electron gas approximation, the Lindhard or RPA dielectric function for the electron gas could be used in order to smooth out the unphysical singularity introduced in our plasmon pole model.

- To extend this method beyond the electron gas model, the inverse dielectric function of real materials can be calculated, and then approximated as a sum of multiple broadened poles. The self energy would then be the sum of self energies computed for each pole using the method of chapter /refextrinsiclosses.

- The effective Green's function could be calculated for real materials. For example, the one electron Green's function between atomic centers is already

calculated in FEFF and could be employed in the expressions for the effective Green's function.

BIBLIOGRAPHY

[1] A. A. Abrikosov, L. P. Gorkov, and I. E. Dzyaloshinski. *Methods of Quantum Mechanics in Statistical Physics*. Dover Publications, Inc., New York, 1994.

[2] Carl-Olaf Almbladh and Lars Hedin. *Handbook of Synchrotron Radiation*, chapter Beyond the One Electron Model; Many Body Effects in Atoms, Molecules, and Solids. North Holland Publishing Company, Amsterdam, 1989.

[3] P. W. Anderson. Infrared catastrophe in fermi gases with local scattering potentials. *Physical Review Letters*, 18(24):1049–1051, 1967.

[4] A. L. Ankudinov, C. E. Bouldin, J. J. Rehr, J. Sims, and H. Hung. Parallel calculations of electron multiple scattering using lanczos algorithms. *Physical Review B*, 65(10):104107/1–11, 2002.

[5] Alex L. Ankudinov et al. Real-space multiple-scattering calculation and interpretation of x-ray absorption near-edge structure. *Physical Review B*, 58(12):7565–76, 1998.

[6] Alex L. Ankudinov and John J. Rehr. Relativistic calculations of spin-dependent x-ray absorption spectra. *Physical Review B*, 56(4):R1712–15, 1997.

[7] Alexei L. Ankudinov et al. Real space multiple-scattering calculation and interpretation of x-ray-absorption near-edge structure. *Phys. Rev. B*, 59:7865, 1998.

[8] F. Aryasetiawan, L. Hedin, and K. Karlsson. Multiple plasmon satellites in Na and Al spectral fuctions from ab-initio cumulant expansion. *Physical Review Letters*, 77(11):2268–2271, 1996.

[9] Neil W. Ashcroft and N. David Mermin. *Solid State Physics*. Harcourt Brace College Publishers, 1976.

[10] W. Bardyszewski and L. Hedin. A new approach to the theory of photoemission from solids. *Physical Scripta*, 32:439–450, 1985.

[11] L. X. Benedict. Dielectric function for a model of laser excited GaAs. *Physical Review B*, 63(7):075202/1–11, 2001.

[12] M. Benfatto et al. Polarized curved-wave extended x-ray absorption fine structure: Theory and application. *Physical Review B*, 39(3):1936–1039, 1989.

[13] N. Binsted, S. L. Cook, J. Evans, G. N. Greaves, and R. J. Price. Exafs and near-edge structure in the cobalt k-edge absorption spectra of metal carbonyl complexes. *Journal of the Americal Chemical Society*, 109(12):3669–3676, 1987.

[14] C. Bouldin, J. Sims, H. Hung, J. J. Rehr, and A. L. Ankudinov. Rapid calculation of x-ray absorption near edge structure using parallel computation. *X Ray Spectrometry*, 30(6):431–4, 2001.

[15] L. Campbell, L. Hedin, J. J. Rehr, and W. Bardyszewski. Interference between extrinsic and intrinsic losses in x-ray absorption fine structure. *Physical Review B*, 65:064107/1–13, 2002.

[16] Luke Campbell et al. XAFS Debye-Waller factors in aqueous Cr+3 from molecular dynamics. *J. Synchrotron Rad.*, 6:310–312, 1999.

[17] Jhy-Jiun Chang and David C. Langreth. Deep-hole excitations in solids ii. plasmons and surface effects in x-ray photoemission. *Physical Review B*, 8:4638–4634, 1973.

[18] J. Friedel. The distribution of electrons round impurities in monovalent metals. *Philosophical Magazine*, 43(337):153–189, 1952.

[19] J. Friedel. X-ray transition probabilities with special reference to k absorption in lithium. *Philosophical Magazine*, 43(346):1115–1139, 1952.

[20] J. Friedel. X-ray absorption and emission edges in metals. *Comments in Solid State Physics*, 2:21–29, 1969.

[21] Takashi Fujikawa. Basic features of the short-range-order multiple scattering xanes theory. *Physical Scripta*, 32:439–450, 1985.

[22] Lars Hedin. New method for calculating the one-particle green's function with applications to the electron gas problem. *Physical Review*, 139(3A):A739–823, 1965.

[23] Lars Hedin. Extrinsic and intrinsic processes in exafs. *Physica B*, 158:344–346, 1989.

[24] Lars Hedin. On correlation effects in electron spectroscopies and the gw approximation. *Journal of Physics: Condensed Matter*, 11(42):R489, 1999.

[25] Lars Hedin, John Michiels, and John Inglesfield. Transition from the adiabatic to the sudden limit in core-electron photemission. *Physical Review B*, 58(23):15565–15582, 1998.

[26] M. S. Hybertsen and S. G. Louie. Theory and calculation of quasiparticle energies and band gaps. *Comments on Condensed Matter Physics*, 13(5):223–247, 1987.

[27] J. E. Inglesfield. Plasmon excitation in core level photoemission. *Journal of Physics C*, 16:403–416, 1983.

[28] David C. Langreth. Singularities in x-ray spectra of metals. *Physical Review B*, 1(2):471–477, 1970.

[29] P. Lloyd. The x-ray spectra and response of conduction electrons to a potential change: The phase shift operator approach. *Journal of Physics F: Metal Physics*, 1:728–738, 1970.

[30] B. I. Lunqvist. Single-particle spectrum of the degenerate electron gas: I. the structure of the spectral weight function. *Phys. Kondens. Materie*, 6:193–205, 1967.

[31] B. I. Lunqvist. Single-particle spectrum of the degenerate electron gas: II. numerical results for electrons coupled to plasmons. *Phys. Kondens. Materie*, 6:206–217, 1967.

[32] G. D. Mahan. Gw approximations. *Comments on Condensed Matter Physics*, 16(6):333–354, 1994.

[33] Gerald D. Mahan. Excitons in metals: Infinite hole mass. *Physical Review*, 163:612–7, 1967.

[34] A. G. McKale, G. S. Knapp, and S. K. Chan. Practical methods for full curved-wave theory analysis of experimental x-ray-adsorption fine structure. *Physical Review B*, 33(2):841–846, 1986.

[35] Matt Newville et al. Analysis of multiple-scattering XAFS data using theoretical standards. *Physica B*, 208 & 209:154–155, 1995.

[36] P. Nozières and C. T. de Dominicis. Singularities in the x-ray absorption and emission of metals. iii. one-body theory exact solution. *Physical Review*, 178:1097–107, 1969.

[37] Simone De Panfilis et al. Liquid Rb micrometric droplets confined in parafin wax: an x-ray absorption spectroscopy study. *Journal of Synchrotron Radiation*, 8:764–766, 2001.

[38] J. B. Pendry. *Low Energy Electron Diffraction*. Academic Press, London, 1974.

[39] Anna V. Poiarkova and John J. Rehr. *Ab initio* Debye-Waller factors. *J. Phys. IV France*, 7:C2–155, 1997.

[40] Anna V. Poiarkova and John J. Rehr. Multiple scattering x-ray absorption fine-structure Debye-Waller factor calculations. *Phys. Rev. B*, 59:9–18, 1999.

[41] J. J. Rehr, R. C. Albers, and S. I. Zabinsky. High-order multiple scattering calculations of x-ray-absorption fine structure. *Physical Review Letters*, 69(23):3397–3400, 1992.

[42] J. J. Rehr, E. A. Stern, R. L. Martin, and E. R. Davidson. Extended x-ray absorption fine structure amplitudes – wave function relaxation and chemical effects. *Physical Review B*, 17:560, 1978.

[43] John J. Rehr and Robert C. Albers. Scattering-matrix formulation of curved-wave multiple-scattering theory: Application to x-ray absorption fine structure. *Phys. Rev. B*, 41:8139, 1990.

[44] John J. Rehr and Robert C. Albers. Theoretical approaches to x-ray absorption fine structure. *Reveiws of Modern Physics*, 72:621, 2000.

[45] J. J. Sakuri. *Modern Quantum Mechanics, Revised Edition*. Addison-Wesley Publishing Company, 1994.

[46] D. E. Sayers et al. *Advances in X-ray Analysis*, chapter Point Scattering Theory of X-ray K-Absorption Fine Structure. Plenum Press, New York, 1997.

[47] D. E. Sayers, E. A. Stern, and F. W. Lytle. New technique for investigating noncrystalline structures: Fourier analysis of the extended x-ray absorption fine structure. *Physical Review Letters*, 27(18):1204–1207, 1971.

[48] E. Sevillano et al. Extended x-ray absorption fine structure Debye-Waller factors. I. monoatomic crystals. *Phys. Rev. B*, 52:4908, 1979.

[49] M. Šunjič and D. Šokçevič. On the problem of "intrinsic" vs "extrinsic" scattering in x-ray photoemission. *Solid State Communications*, 18:373–375, 1976.

[50] B. K. Teo and P. A. Lee. *Journal of the American Chemical Society*, 101:2815, 1979.

[51] S. I. Zabinsky et al. Multiple-scattering calculations of x-ray-absorption spectra. *Physical Review B*, 52(4):2995, 1995.

VITA

Luke Campbell was born in Sacramento, California. He grew up in the Palouse region of Eastern Washington in a little town called Pullman. Luke earned his Bachelor of Science in Physics at the University of California, Davis in 1995. In 1996, he was awarded a Masters of Science in Physics by the University of Washington. He earned his Doctor of Philosophy degree in Physics at the University of Washington in 2002.